

AD-A245 327



WL-TR-91-2086

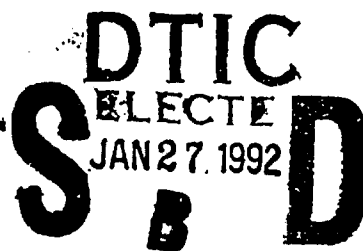


ANALYSIS OF FROZEN STARTUP OF HIGH-TEMPERATURE HEAT PIPES  
AND THREE-DIMENSIONAL MODELING OF BLOCK-HEATED HEAT PIPES

Amir Faghri, Ph.D.  
Brage Golding Distinguished Professor

DEPARTMENT OF MECHANICAL AND MATERIALS ENGINEERING  
WRIGHT STATE UNIVERSITY  
DAYTON, OH 45435

NOVEMBER 1991



INTERIM REPORT FOR PERIOD JANUARY 1990 - MAY 1991

Approved for public release; distribution is unlimited.

92-01685



AERO PROPULSION AND POWER DIRECTORATE  
WRIGHT LABORATORY  
AIR FORCE SYSTEMS COMMAND  
WRIGHT-PATTERSON AIR FORCE BASE, OHIO 45433-6563

02 1 21 018

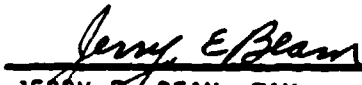
# NOTICE

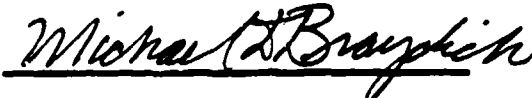
When Government drawings, specifications, or other data are used for any purpose other than in connection with a definitely Government-related procurement, the United States Government incurs no responsibility or any obligation whatsoever. The fact that the government may have formulated or in any way supplied the said drawings, specifications, or other data, is not to be regarded by implication, or otherwise in any manner construed, as licensing the holder, or any other person or corporation; or as conveying any rights or permission to manufacture, use, or sell any patented invention that may in any way be related thereto.

This report is releasable to the National Technical Information Service (NTIS). At NTIS, it will be available to the general public, including foreign nations.

This technical report has been reviewed and is approved for publication.

  
WON S. CHANG  
Project Engineer

  
JERRY E. BEAM, TAM  
Power Technology Branch  
Aerospace Power Division  
Aero Propulsion and Power Directorate

  
MICHAEL D. BRAYDICH, Lt Col, USAF  
Deputy Director  
Aerospace Power Division  
Aero Propulsion & Power Directorate

If your address has changed, if you wish to be removed from our mailing list, or if the addressee is no longer employed by your organization please notify WL/POOS, WPAFB, OH 45433-6563 to help us maintain a current mailing list.

Copies of this report should not be returned unless return is required by security considerations, contractual obligations, or notice on a specific document.

UNCLASSIFIED

SECURITY CLASSIFICATION OF THIS PAGE

REPORT DOCUMENTATION PAGE				Form Approved OMB No. 0704-0188		
1a. REPORT SECURITY CLASSIFICATION Unclassified			1b. RESTRICTIVE MARKINGS N/A			
2a. SECURITY CLASSIFICATION AUTHORITY N/A			3. DISTRIBUTION/AVAILABILITY OF REPORT Approved for public release; distribution is unlimited.			
2b. DECLASSIFICATION/DOWNGRADING SCHEDULE N/A						
4. PERFORMING ORGANIZATION REPORT NUMBER(S)  WSU-TR-88-001			5. MONITORING ORGANIZATION REPORT NUMBER(S)  WL-TR-91-2086			
6a. NAME OF PERFORMING ORGANIZATION  Wright State University		6b. OFFICE SYMBOL (If applicable)	7a. NAME OF MONITORING ORGANIZATION Aero Propulsion & Power Dir. (WL/POOS) Wright Laboratory			
6c. ADDRESS (City, State, and ZIP Code) Dept. of Mechanical & Materials Engineering Wright State University Dayton, OH 45435			7b. ADDRESS (City, State, and ZIP Code)  Wright-Patterson AFB, OH 45433-6563			
8a. NAME OF FUNDING/SPONSORING ORGANIZATION Wright Research and Development Center		8b. OFFICE SYMBOL (If applicable) WL/POOS	9. PROCUREMENT INSTRUMENT IDENTIFICATION NUMBER  F-33615-86-C-2720			
8c. ADDRESS (City, State, and ZIP Code) Aero Propulsion and Power Directorate Wright-Patterson AFB, OH 45433-6563			10. SOURCE OF FUNDING NUMBERS			
			PROGRAM ELEMENT NO 62203F	PROJECT NO 3145	TASK NO 20	WORK UNIT ACCESSION NO. 06
11. TITLE (Include Security Classification) Analysis of Frozen Startup of High-Temperature Heat Pipes and Three-Dimensional Modeling of Block-Heated Heat Pipes						
12. PERSONAL AUTHOR(S) Amir Faghri, Ph.D., Brage Golding Distinguished Professor						
13a. TYPE OF REPORT Final		13b. TIME COVERED FROM JAN 90 TO MAY 91		14. DATE OF REPORT (Year, Month, Day) November 1991		
15. PAGE COUNT 165						
16. SUPPLEMENTARY NOTATION						
17. COSATI CODES			18. SUBJECT TERMS (Continue on reverse if necessary and identify by block number)  Heat Pipes; Startup; Multiple Heat Sources; Block Heating			
FIELD	GROUP	SUB-GROUP				
19. ABSTRACT (Continue on reverse if necessary and identify by block number)  The startup behavior of high-temperature heat pipes from the frozen state was investigated both numerically and experimentally for various heat loads and input locations. A high-temperature sodium/stainless steel heat pipe with multiple heat sources and sinks was fabricated, processed, and tested. A numerical simulation of the transient heat pipe performance including the vapor region, wick structure and the heat pipe wall is given. Furthermore, experimental and numerical analyses of several operating parameters of a low-temperature copper-water heat pipe under uniform circumferential heating and block heating has been performed. Finally, a numerical analysis of transient heat pipe performance including nonconventional heat pipes with nonuniform heat distributions is presented. Numerical calculations were then made for a leading edge heat pipe with localized high heat fluxes.						
20. DISTRIBUTION/AVAILABILITY OF ABSTRACT <input checked="" type="checkbox"/> UNCLASSIFIED/UNLIMITED <input type="checkbox"/> SAME AS RPT. <input type="checkbox"/> DTIC USERS			21. ABSTRACT SECURITY CLASSIFICATION Unclassified			
22a. NAME OF RESPONSIBLE INDIVIDUAL Won S. Chang			22b. TELEPHONE (Include Area Code) (513) 255-2922		22c. OFFICE SYMBOL WL/POOS	

DD Form 1473, JUN 86

Previous editions are obsolete

SECURITY CLASSIFICATION OF THIS PAGE  
Unclassified

## FOREWORD

The information in this report was assembled for contract #F33615-88-C-2820 with the Aero Propulsion and Power Directorate, Wright Laboratory and NASA Lewis Research Center as the sponsoring agencies. This is the third annual report on this contract. The other two reports were WRDC-TR-90-2031 and WRDC-TR-89-2077. The work was carried out at the Department of Mechanical and Materials Engineering at Wright State University.

During 1990, five tasks were performed as outlined in the Table of Contents. The various tasks dealt with the frozen startup of a high-temperature heat pipe, the effects of block heating on a low-temperature heat pipe, and a transient analysis of nonconventional heat pipes with uniform and nonuniform heat distributions. Five journal publications were produced from the present work. Five graduate research assistants, Mr. Matt Buchko, Mr. Yiding Cao, Mr. Joe Schmalhofer, Mr. Scott Thomas, and Mr. Mike McDonough, were involved in the preparation of this work. Dr. Won Chang from Wright Laboratory was the technical supervisor for this contract and the author is grateful to him for his discussions and comments. Support from Dr. Jerry Beam and Dr. Tom Mahefkey from Wright Laboratory and Mr. Jim Calogeras, Mr. Al Juhasz, and Mr. Ron Sovie from NASA Lewis Research Center is greatly appreciated.



<b>Accession For</b>	
NTIS GRA&I	<input checked="checked" type="checkbox"/>
DTIC TAB	<input type="checkbox"/>
Unannounced	<input type="checkbox"/>
Justification	
By _____	
Distribution/	
Availability Codes	
Disc	Avail and/or Special
A-1	

## TABLE OF CONTENTS

Section	Page
I. EXPERIMENTAL METHODOLOGY AND FROZEN STARTUP PROFILES OF HIGH-TEMPERATURE HEAT PIPES WITH MULTIPLE HEAT SOURCES AND SINKS .....	
1.1 Summary.....	1
1.2 Introduction.....	2
1.3 Experimental Apparatus and Procedure.....	4
1.4 Results and Discussion.....	11
1.5 Conclusions.....	24
II. AN ANALYSIS OF CONTINUUM TRANSIENT AND STEADY-STATE EXPERIMENTAL DATA WITH NUMERICAL PREDICTIONS OF HIGH-TEMPERATURE HEAT PIPES.....	
2.1 Summary.....	26
2.2 Introduction.....	27
2.3 Characteristics of Continuum Transient and Steady-State Operations.....	28
2.4 Numerical Modeling and Predictions.....	40
2.4.1 Governing Equations.....	40
2.4.2 Boundary Conditions.....	42
2.4.3 Numerical Procedure.....	44
2.4.4 Numerical Predictions.....	46
2.5 Conclusions.....	53
III. EXPERIMENTAL ANALYSIS AND GENERALIZED ANALYTICAL PREDICTION OF CAPILLARY LIMITS OF CIRCUMFERENTIALLY-HEATED AND BLOCK-HEATED HEAT PIPES.....	
3.1 Summary.....	55
3.2 Introduction.....	56
3.3 Experimental Setup and Test Procedures.....	57
3.4 Generalized Analytical Prediction of Capillary Limit for Block Heating.....	63
3.5 Results and Discussion.....	70
3.5.1 Elapsed Time to 60°C Vapor Temperature.....	71
3.5.2 Transient and Steady-State Temperature Comparisons.....	71
3.5.3 Capillary Limit.....	80
3.6 Conclusions.....	82

## Table of Contents (continued)

Section	Page
IV. THREE-DIMENSIONAL NUMERICAL MODELING OF CIRCUMFERENTIALLY-HEATED AND BLOCK-HEATED HEAT PIPES:.....	
4.1 Summary.....	84
4.2 Introduction.....	85
4.3 Mathematical Modeling.....	87
4.4 Numerical Solution Procedure.....	93
4.5 Results and Discussion.....	96
4.6 Circumferentially-Heated Heat Pipe Model.....	97
4.7 Block-Heated Heat Pipe Model.....	102
4.8 Conclusions.....	112
V. TRANSIENT MULTIDIMENSIONAL ANALYSIS OF NONCONVENTIONAL HEAT PIPES WITH UNIFORM AND NONUNIFORM HEAT DISTRIBUTIONS.....	
5.1 Summary.....	114
5.2 Introduction.....	115
5.3 Mathematical Modeling.....	118
5.3.1 Heat Pipe Wall and Wick.....	119
5.3.2 Transient Compressible Quasi - One-Dimensional Vapor Flow.....	121
5.3.3 Boundary Conditions and Friction Coefficients.....	123
5.3.4 Limits to Heat Transport.....	126
5.3.5 Capillary Limits.....	126
5.3.6 Boiling Limit.....	127
5.4 Numerical Procedure.....	128
5.5 Numerical Results and Discussion.....	130
5.6 Conclusions.....	142
VI. REFERENCES.....	145

## **LIST OF FIGURES**

<b>Figure</b>		<b>Page</b>
1.1	High-Temperature Heat Pipe Thermocouple Locations.....	7
1.2	High-Temperature Heat Pipe Assembly.....	9
1.3	Vacuum Chamber Operating System.....	12
1.4	Transient Axial Vapor Temperature Profiles With Evaporator 1 Active.....	15
1.5	Transient Axial Vapor Temperature Profiles With Evaporator 2 Active.....	16
1.6	Effects of Test Environment on Transient Vapor Temperatures During Startup.....	18
1.7	Transient Axial Vapor Temperature Profiles for One Evaporator Operation in Vacuum.....	21
1.8	Transient Axial Vapor Temperature Profiles for Operation in Vacuum With Evaporators 1 and 4 Active.....	22
1.9	Transient Axial Vapor Temperature Profiles for Two Evaporator Operation in Vacuum.....	23
2.1	Effect of Emissivity on Steady-State Axial Vapor Temperature Profiles.....	30
2.2	Effect of Evaporator Elevation on Steady-State Axial Vapor Temperature Profiles.....	30
2.3	Effect of Startup Power Levels on Steady-State Axial Vapor Temperature Profiles.....	32
2.4a	Axial Heat-Transfer Limits Versus Transport Vapor Temperature for Operation in Air and Vacuum With Evaporator 1 Active.....	34
2.4b	Steady-State Axial Vapor Temperature Profiles for Operation in Air and Vacuum With Evaporator 1 Active.....	34
2.5a	Axial Heat-Transfer Limits Versus Transport Vapor Temperature for Operation in Air and Vacuum With Evaporator 2 Active.....	35
2.5b	Steady-State Axial Vapor Temperature Profiles for Operation In Air and Vacuum With Evaporator 2 Active.....	35
2.6a	Axial Heat-Transfer Limits Versus Transport Vapor Temperature for Operation in Air and Vacuum With Evaporator 3 Active.....	36

# List of Figures (continued)

Figure	Page
2.6b	Steady-State Axial Vapor Temperature Profiles for Operation in Air and Vacuum With Evaporator 3 Active.....36
2.7a	Axial Heat-Transfer Limits Versus Transport Vapor Temperature for Operation in Air and Vacuum With Evaporator 4 Active.....37
2.7b	Steady-State Axial Vapor Temperature Profiles for Operation in Air and Vacuum With Evaporator 4 Active.....37
2.8	Evaporator 1 Dryout for Case 28h Total Power in 2409 Watts, Operation in Air With 5.7' Evaporator Elevation.....38
2.9	The Multiple - Evaporator Heat Pipe and Coordinate System.....40a
2.10	The Vapor Temperature for Different Time Periods Compared With the Experimental Data for Cases 6b-6c.....48
2.11	The Vapor Temperature for Different Time Periods Compared With the Experimental Data for Cases 19c-19d.....49
2.12	The Vapor Temperature for Different Time Periods Compared With the Experimental Data for Cases 21d-21e.....50
2.13	The Axial Velocity Profile Along the Centerline for Different Time Periods With Cases 21d-21e.....51
2.14	The Axial Pressure Profile Along the Centerline of the Heat Pipe for Different Time Periods With Cases 21d-21e.....52
3.1	Schematic of Experimental Setup.....58
3.2	Experimental Heat Pipe Configuration.....60
3.3	Heat Pipe Thermocouple Locations.....62
3.4	Time for Heat Pipe Vapor Temperature to Reach 60°C Versus Step Heat Input.....72
3.5	Transient Starting Temperature Profiles of the Circumferentially- Heated Heat Pipe for 50 W.....73
3.6	Transient Starting Temperature Profiles of the Circumferentially- Heated Heat Pipe for 150 W.....74
3.7	Transient Starting Temperature Profiles of the Block-Heated Heat Pipe for 50 W.....75
3.8	Transient Starting Temperature Profiles of the Block-Heated Heat Pipe for 150 W.....76

# List of Figures (continued)

Figure		Page
3.9	Vapor and Wall Temperature Versus Axial Distance From Evaporator End Cap for 50 Watt Step Heat Input.....	78
3.10	Vapor and Wall Temperature Versus Axial Distance From Evaporator End Cap for 150 Watt Step Heat Input.....	79
3.11	Analytical and Experimental Capillary Limit Versus Vapor Temperature for Circumferential and Block Heating Modes.....	81
4.1	Block-Heated Heat Pipe Model.....	88
4.2	Circumferentially-Heated Heat Pipe Model.....	89
4.3	Circumferentially-Heated Heat Pipe, $Q = 100$ W.....	98
4.4	Axial Variation of Velocity for the Circumferentially-Heated Heat Pipe, $Q = 100$ W.....	100
4.5	Outer Wall Temperature for the Circumferentially-Heated Heat Pipe ( $^{\circ}\text{C}$ ), $Q = 100$ W.....	101
4.6	Block-Heated Heat Pipe, $Q = 100$ W.....	103
4.7	Axial Variation of Velocity for the Block-Heated Heat Pipe Model, $Q = 100$ W.....	104
4.8	Outer Wall Temperatures for the Block-Heated Heat Pipe Model ( $^{\circ}\text{C}$ ), $Q = 100$ W.....	107
4.9	Velocity Variation in the Radial and Circumferential Directions in the Evaporator Section of the Block-Heated Heat Pipe Model, $Q = 100$ W.....	108
4.10	Velocity Variation in the Radial and Circumferential Directions in the Adiabatic Section of the Block-Heated Heat Pipe Model, $Q = 100$ W.....	109
4.11	Velocity Variation in the Radial and Circumferential Directions in the Condenser Section of the Block-Heated Heat Pipe Model, $Q = 100$ W.....	110
5.1	Schematic of the Leading Edge Heat Pipe.....	116
5.2	Body-Fitted Grids for the Wall and Wick Region (not to scale)....	120
5.3	Vapor Control Volume for the Conservation of Mass and Momentum...	122
5.4	The Axial Temperature Profiles Along the Sodium Heat Pipe Compared With the Experimental data by Kemme (1969).....	131

# List of Figures (continued)

Figure	Page
5.5	The Vapor Temperature for Different Time Periods Compared with the Experimental Data by Faghri and Buchko (1990).....134
5.6	The Startup Axial Mach Number Along the Leading Edge Heat Pipe With Uniform Heating and High Heat-Transfer Coefficient.....135
5.7	The Leading Edge Heat Pipe With Uniform Heating at Evaporator a) Outer Wall Temperature b) Vapor Temperature c) Axial Mach Number.....137
5.8	The Heat Pipe With Line Source at the Leading Edge a) Outer Wall Temperature b) Vapor Temperature c) Axial Mach Number.....139
5.9	The Liquid and Vapor Pressure Distributions Along the Heat Pipe for Different Time Periods.....141
5.10	The Outer Wall Temperature Along the Stagnation Line for the Case of Nonuniform Heating.....143

## LIST OF TABLES

Table	Page
3.1 Physical Dimensions and Material Properties of the Circumferentially-Heated and Block-Heated Heat Pipe.....	59
4.1 Boundary Conditions for Circumferentially-Heated and Block-Heated Heat Pipe Models.....	94

## NOMENCLATURE

- a coefficient in eqn. (5.17)
- a coefficient in the discretization equation (2.17)
- A cross-sectional area,  $m^2$
- $A_c$  outer surface area of condenser section,  $m^2$
- $A_e$  outer surface area of evaporator section,  $m^2$
- b source term in eqn. (2.17)
- B source term in eqn. (5.17)
- $c_p$  specific heat at constant pressure,  $J/(kg \cdot K)$  (5)
- C ratio of the screen mesh diameter to the opening width of the screen,  
 $d/w_s$
- $C_p$  specific heat,  $J/kg \cdot K$  (4)
- d screen mesh wire diameter, m
- $d_i$  container inner diameter, m
- $d_w$  wick inner diameter
- D diameter of the heat pipe, m (5)
- D ratio of the screen mesh wire diameter to the wick thickness,  $d/t_w$  (4,3)
- $D_v$  dynamic pressure coefficient,  $(N/m^2)/W^2$
- $D_h$  hydraulic diameter, m
- f friction coefficient,  $2\tau_w/\rho U^2$
- F frictional pressure coefficient,  $(N/m^2)/W^2$
- $(f_v Re_v)$  drag constant
- g gravity constant,  $m/s^2$
- G liquid mass flow rate in the wick, kg/s
- h convective heat transfer coefficient,  $W/(m^2 \cdot K)$
- $h_{fg}$  latent heat, J/kg
- $h_o$  half thickness of the leading edge heat pipe, m

$k$  thermal conductivity,  $W/(m \cdot K)$   
 $K$  wick permeability,  $m^2$   
 $L$  Total length of the heat pipe,  $m$   
 $L_a$  total adiabatic section length,  $m$   
 $L_c$  condenser length,  $m$   
 $L_e$  evaporator length,  $m$   
 $L_{eff}$  effective total transport length,  $m$   
 $\dot{m}$  mass flow,  $kg/s$   
 $m_i$  mass flux at the liquid-vapor interface,  $kg/(m^2 \cdot s)$   
 $Ma$  Mach number,  $U/\sqrt{\gamma p/\rho_v}$   
 $p'$  pressure correction,  $N/m^2$   
 $p_o$  reference pressure,  $N/m^2$  (2)  
 $P$  pressure,  $N/m^2$   
 $P_c$  capillary pressure,  $N/m^2$   
 $P_{cm}$  maximum capillary pressure,  $N/m^2$   
 $P_n$  normal hydrostatic pressure,  $N/m^2$   
 $q$  heat flux,  $W/m^2$  (2), (5)  
 $q$  radial heat flux,  $W/m^2$  (4)  
 $q_i$  heat flux,  $W/m^2$   
 $q_s$  heat source term,  $W/m^2$   
 $Q$  axial heat transport,  $W$  (3)  
 $Q$  heat input at the outer wall of the evaporator,  $W$  (5)  
 $Q_{c,max}$  analytical capillary limit,  $W$   
 $Q_{in}$  heat input rate at the evaporator section,  $W$   
 $Q_{out}$  heat output rate at the condenser,  $W$   
 $Q^*$  local axial heat rate,  $W$   
 $Q'$  axial heat rate per unit circumferential length,  $W/m$

$r$  radial coordinate, m  
 $r$  radial coordinate or capillary radius, m (5)  
 $r_c$  effective capillary radius of the wick pores at the liquid-vapor interface, m  
 $r_{h,v}$  hydraulic radius of vapor flow, m  
 $r_n$  initial radius of the vapor bubble at formation, m  
 $r_p$  wick pore radius, m  
 $R$  gas constant, J/kg-K  
 $R_{ave}$  average liquid-wick radius, m (3)  
 $Re$  axial Reynolds number (2)  
 $Re$  Reynolds number,  $UD/\nu$  (5)  
 $R_i$  leading edge radius, m (5)  
 $R_m$  radius of curvature of the meniscus in eqn. (5.16), m (5)  
 $R_o$  outer pipe wall radius, m (2)  
 $R_v$  vapor core radius, m  
 $R_w$  wick-wall interface radius, m  
 $S$  channel wall surface area between the leading edge and position  $x$ ,  $m^2$   
 $t$  time, s  
 $t_w$  wick thickness, m  
 $T$  temperature, K  
 $T_a$  environment temperature, K  
 $T_o$  reference temperature, K  
 $T_w$  outer wall surface temperature, K  
 $T_w$  outer wall surface temperature, K  
 $u$  azimuthal velocity component, m/s  
 $U$  axial velocity, m/s  
 $U^*$  axial velocity based on the guessed pressure  $p^*$ , m/s

$v$	radial velocity, m/s
$v^*$	radial velocity based on the guessed pressure, $p^*$ , m/s
$v_i$	radial vapor velocity at the liquid-vapor interface, m/s
$w$	axial velocity, m/s
$w^*$	axial vapor velocity based on the guessed pressure $p^*$ , m/s
$w_s$	screen mesh opening width, m
$W$	width of the heat pipe for numerical calculation, m
$W_e$	heating width in z-direction, m
$x$	axial coordinate, m
$x'$	vapor quality
$z$	axial coordinate
$z$	width direction in Fig. 5.1

### Greek Symbols

$\alpha$	slope of the heat pipe wall, rad
$\gamma$	ratio of specific heats, $c_p/c_v$
$\delta$	wall or liquid-wick thickness, m
$\epsilon$	emmissivity (2)
$\epsilon$	wick porosity (3)
$\theta$	circumferential angle, rad (3)
$\theta$	tangential coordinate at the leading edge (5)
$\mu$	dynamic viscosity, kg/m-s
$\nu$	kinematic viscosity, $m^2/s$
$\nu_\ell$	liquid kinematic viscosity, $m^2/s$
$\xi$	dummy variable in eqn.
$\rho$	density, $kg/m^3$
$\sigma$	Stefan-Boltzmann constant, $W/(m^2 \cdot K^4)$ (2)

- $\sigma$  surface tension, N/m (3, 5)
- $\sigma_l$  liquid surface tension, N/m
- $\phi$  general variable in the discretization eqn. (2.17)
- $\dot{\phi}$  viscous dissipation term in eqn. (2.4)
- $w$  wick porosity
- $\theta$  heat pipe inclination angle, rad (3)

### Subscripts

- a adiabatic
- b vapor bubble
- c condenser
- c condenser or capillary
- e evaporator
- eff effective
- E "east" neighbor of grid P
- f fluid (5)
- i vapor-liquid interface or initial condition
- $l$  liquid or liquid-wick (2), (5)
- $l$  liquid (3), (4)
- $lw$  liquid-wick region (5)
- L latent heat
- max maximum
- min minimum
- N "north" neighbor of grid P

o properties of the injected or extracted fluid at the liquid-vapor interface  
 o,c outer wall condenser  
 o,e outer wall evaporator  
 P grid point  
 ref reference (3)  
 s wick structure material (2)  
 s solid (4)  
 s saturation or wick structure material (5)  
 S "south" neighbor of grid P (2)  
 v vapor  
 w wall (2), (5)  
 w wick (3), (4)  
 W "west" neighbor of grid P  
 0 datum

## Section I

### EXPERIMENTAL METHODOLOGY AND FROZEN STARTUP PROFILES OF HIGH TEMPERATURE HEAT PIPES WITH MULTIPLE HEAT SOURCES AND SINKS

#### 1.1 SUMMARY

A high-temperature sodium/stainless steel heat pipe with multiple heat sources and sinks was fabricated, processed, and tested. Experimental results from tests performed both under vacuum and in air are presented. The startup behavior of the heat pipe from the frozen state was investigated for various heat loads and input locations, with both low and high heat rejection rates at the condenser. No startup evaporator dryout failures were found, although the heat pipe was sonic-limited during startup in air.

## 1.2 INTRODUCTION

The use of high-temperature heat pipes has been proposed for cooling the leading edges and nose cones of re-entry vehicles, rail guns, and laser mirrors, as well as for the thermal management of future hypersonic vehicle structures. These applications will require an understanding of the behavior and performance of liquid metal heat pipes with multiple nonuniform heat inputs. In general, the analytical and experimental analyses developed for single evaporator heat pipes cannot be applied to multiple evaporator heat pipes with nonuniform heat loads.

A high-temperature heat pipe is a closed-system heat transfer device which operates between  $300^{\circ}\text{C}$  and  $1500^{\circ}\text{C}$  and contains a wick structure with a liquid metal working fluid such as potassium or sodium. When a numerical model of high-temperature heat pipe behavior is proposed, the model must be compared to existing experimental data for verification. Specific parameters of the heat pipe that may be needed are the geometry, dimensions, wall material, working fluid, wick type, and the operating temperature range. For comparison with experimental data, detailed information on the heat pipe operating system is also needed. These data should include the type and shape of evaporator heat source, condenser cooling method, heat pipe instrumentation, and measurements of the evaporator and condenser heat fluxes. The type of test performed, such as startup, transient, or steady-state is also important. Unfortunately, most of the previous high-temperature investigations with a single evaporator were presented in conference proceedings and many of the above experimental details were not reported.

Since the startup behavior of a high-temperature heat pipe in air is markedly different from a startup performed under vacuum, the test environment should be reported. There are some disadvantages to operation in air, such as controlling and quantifying convection losses, and possible safety hazards if the container corrodes or fails. Startup in air may also be difficult because of a high heat rejection rate at the condenser. Testing a high-temperature heat pipe in a vacuum chamber eliminates convection losses, prevents oxidation of the container wall, and provides a physical barrier between the heat pipe and the laboratory in case of containment failure. Startup failures generally do not occur in vacuum because the radiation boundary condition at the condenser induces a self-adjusting active condenser length and frontal startup behavior.

The experimental investigation of the operating characteristics of a multiple heat source high-temperature heat pipe was necessary for several reasons:

1. A literature search did not reveal any experimental data for multiple heat source high-temperature heat pipes, and the startup behavior for such a heat pipe was expected to differ from that with a single evaporator.
2. Vapor temperatures, and therefore the vapor pressures, were usually deduced from wall thermocouples, which can be influenced by the type of thermocouple used and the thermocouple mounting method. The wall thermocouple wires may absorb reflected radiation, or act as a small fin at high temperatures, which can cause a steep temperature gradient

along the thermocouple wire and inaccurate temperature readings. Direct measurement of the vapor temperatures is the only accurate approach for determining the startup behavior from the frozen state.

3. Many researchers report only the heat input to the evaporator or the heat output from the condenser, and an accurate energy balance for the heat pipe system cannot be attained. Heat losses from the evaporator and transport sections are significant, even with
4. The convection losses that are due to operation need to be determined for accurate system energy balances.
5. The conventional analytical predictions of Dunn and Reay (1982) and Chi (1976) for the capillary limits of heat pipes are often inaccurate and cannot be extended to multiple heat source heat pipes. Therefore, the capillary limits for multiple heat source heat pipes must be determined experimentally or by using a detailed numerical simulation model. In terrestrial applications the experimental data can be used in designing commercial heat pipes.
6. Accurate and detailed experimental results for the operating behavior of a high-temperature heat pipe with multiple evaporators will be required for verification of future numerical simulation models.

### 1.3 EXPERIMENTAL APPARATUS AND PROCEDURE

The high-temperature heat pipe was a sodium/stainless steel heat pipe designed to operate at a vapor temperature range of 500°C - 800°C. The

compatibility of 304L stainless steel with sodium is well-documented in heat pipe literature. No attempt was made to design a high capacity heat pipe since the main objective was to obtain detailed and accurate experimental data related to the frozen startup operating characteristics with multiple heat sources.

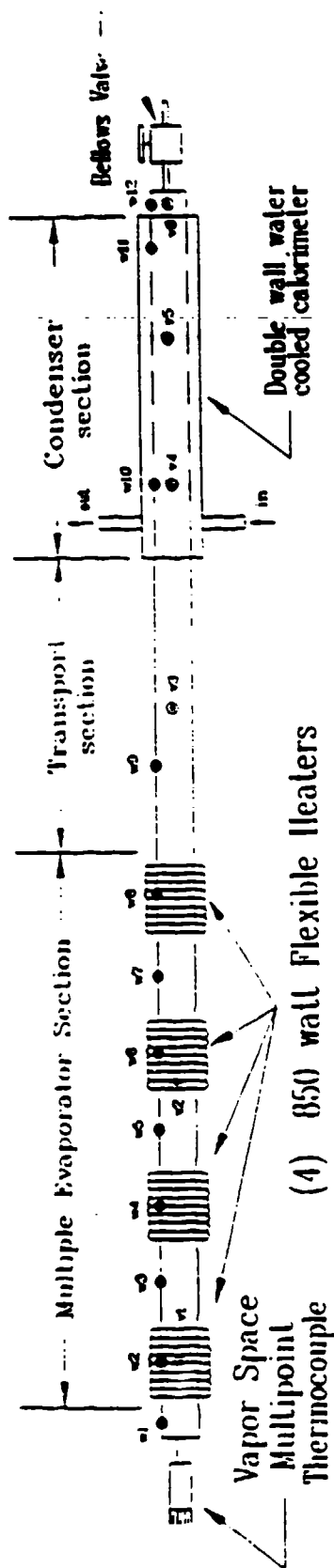
The heat pipe shell and end caps were fabricated from Type 304L stainless steel. The heat pipe shell is 1000 mm in length, with an outside diameter of 26.7 mm, and a wall thickness of 2.15 mm. The ends of the heat pipe shell were machined so that the end caps fit snugly. All of the heat pipe parts were carefully fitted and cleaned using standard procedures. The heat pipe shell, end caps, and wick material were degreased with 1,1,1-trichloroethane, rinsed in deionized water, then rinsed in methanol and allowed to air dry.

A simple circumferential screen wick consisting of two wraps of 100 mesh Type 304 stainless steel was installed to provide a liquid return path to the evaporators. The wick was rolled on a 19-mm mandrel which provided a positive tension in the wick against the heat pipe wall. The vapor core diameter is 21.5 mm. The screen wire diameter and screen wick thickness are 0.114 and 0.456 mm, respectively.

The end caps were TIG welded to the heat pipe shell, and the interior of the heat pipe was protected from oxidation during the welding process by a cover layer of nitrogen. A high-temperature bellows-type valve was attached to the heat pipe fill tube to facilitate sealing, purging, and charging of the fluid inventory.

The heat pipe had four independently-controlled heaters in the evaporator section. After consideration of several heat sources, Inconel 600 Aerorod BXX flexible electric heaters manufactured by ARi Industries were chosen since they were judged most reliable for the heat pipe performance tests. An important advantage of these flexible heaters was their ability to withstand high watt densities at temperatures up to 1000°C. Each evaporator consisted of one 850 watt heater coiled around the heat pipe circumference, giving an individual evaporator length of 53 mm, with 90 mm adiabatic sections separating each evaporator (Figure 1.1). One problem with coil-on heaters is a large temperature drop between the heater elements and the heat pipe wall because of poor thermal contact. In order to minimize the thermal contact resistance, a stainless steel clamp was mounted around each heater. Power input to each heater was supplied by a 120-volt variable ac transformer. The electrical currents and voltages to each heater were measured with a Fluke 77 multimeter, which has an uncertainty of  $\pm 2\%$  of the reading.

Heat pipe vapor and wall temperatures were measured with Type K thermocouples, which were calibrated with an accuracy of  $\pm 0.3^\circ\text{C}$ . There were 12 wall thermocouples, 6 vapor space thermocouples, and 1 thermocouple on the top of each heater (Figure 1.1). Wall thermocouples in the adiabatic, transport, and condenser sections were spot-welded to the heat pipe wall. One sheathed thermocouple was located in a shallow groove underneath each heater coil. A 4.7-mm diameter, Type 316 stainless steel sheathed multipoint thermocouple mounted axially within the heat pipe vapor space provided vapor temperatures at six locations. The multipoint thermocouple exited the heat pipe through a tube in the evaporator end cap



Evaporator section length  $\uparrow$  --- (4) 53-mm evaporators with 90-mm separation = 502-mm total

Transport length  $\uparrow$  --- 188 mm

Condenser length  $\uparrow$  --- 292 mm

• Wall thermocouple  
 ◉ Vapor-space thermocouple

Thermocouple distance from evaporator end cap, mm

v1	45	w1	10	w7	405
v2	322	w2	55	w8	487
v3	615	w3	120	w9	601
v4	738	w4	199	w10	740
v5	861	w5	265	w11	935
v6	986	w6	342	w12	990

{ 20-mm adiabatic section between the evaporator end cap and evaporator 1  
 } 20-mm adiabatic section between the condenser and the condenser end cap

Figure 1.1 High-Temperature Heat Pipe Thermocouple Locations

and was locked in place with a compression fitting to provide a leak-tight seal. Temperature data were monitored with a Fluke 2285B Datalogger interfaced with an IBM personal computer for data storage and were typically recorded every 2 to 5 minutes.

The evaporator section of the heat pipe was insulated with a specially fabricated clam-shell radiation heat shield unit in order to minimize the radiation losses. The evaporator radiation shield consisted of six individual shields arranged concentrically around the heat pipe. The shields were fabricated from 0.127-mm Type 304 stainless steel shim-stock, and were mounted to a stainless steel jacket 127 mm in diameter and 1.6 mm thick (Figure 1.2). The radiation shield also included internal ceramic baffles to separate the evaporators from the adjacent adiabatic sections. The adiabatic transport section of the heat pipe was insulated with six concentric radiation shields in the same manner as the evaporator section. Both the evaporator and transport sections were fitted with water-cooled calorimeters to measure the actual heat losses occurring in each section. The evaporator calorimeter was fabricated by soldering a continuous line of copper tubing to the outer wall of the radiation shield jacket. For the transport section calorimeter a jacket was fabricated from 127-mm diameter 1.6-mm wall copper pipe, and a continuous line of copper tubing was then soldered to the outer wall of the jacket. The evaporator and transport section calorimeter coolant supply lines were connected in series.

Heat was removed from the condenser section by radiation to a water-cooled double-wall calorimeter fabricated from copper. The calorimeter was 292-mm long, with an inner radius of 32 mm, leaving a gap

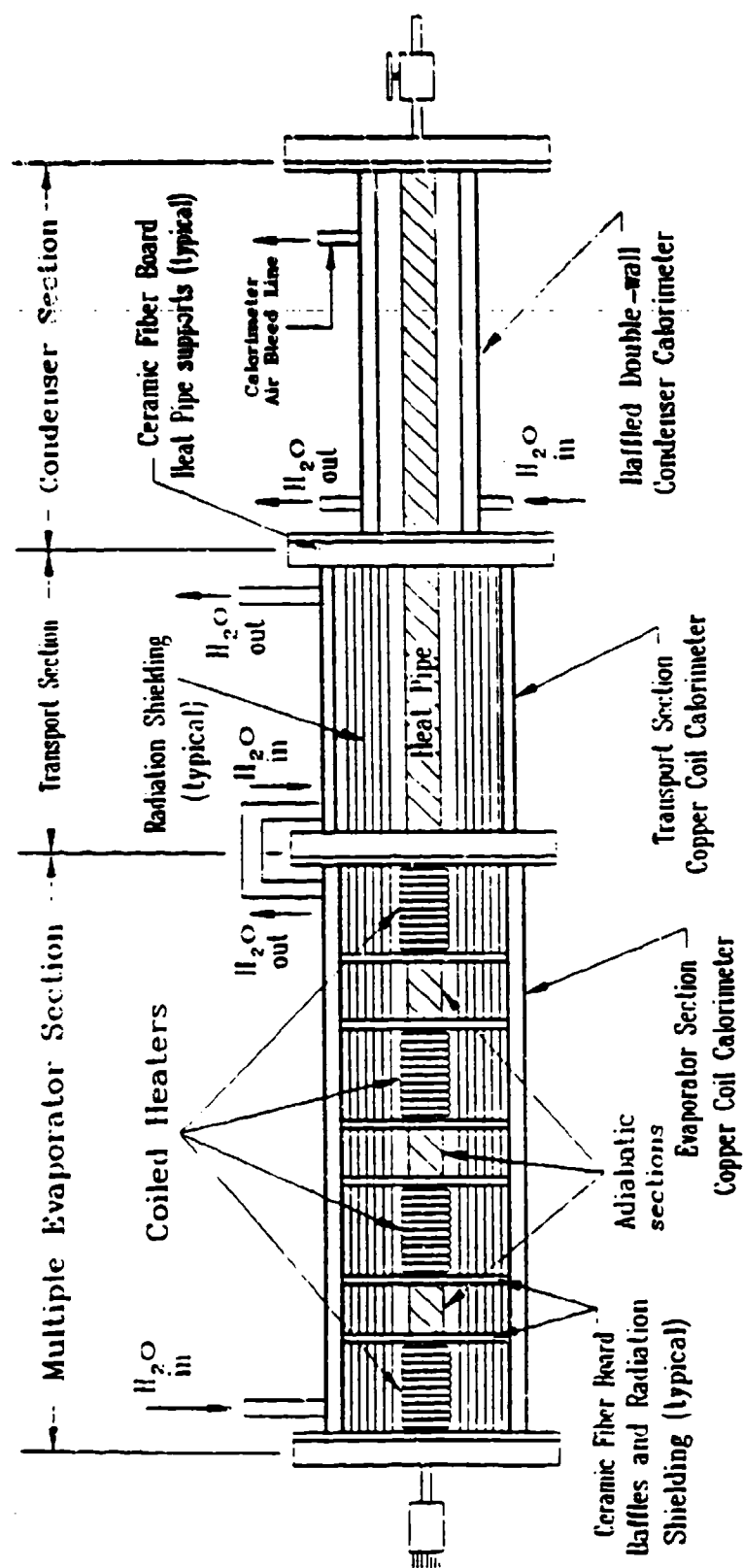


Figure 1.2 High-Temperature Heat Pipe Assembly

of 19 mm between the heat pipe wall and the calorimeter surface. The calorimeter was equipped with internal baffles to improve the heat transfer between the inner wall and the coolant flow, and was fitted with an air bleed valve located at the top of the outer wall to ensure complete filling of the calorimeter.

Type K thermocouples located in the calorimeter inlets and outlets and measurements of the coolant mass flow rate through the calorimeters allowed the heat losses from the each section of the heat pipe to be calculated. An accurate energy balance for the heat pipe could be computed by adding the heat losses from the evaporator, transport, and condenser sections and comparing the total heat loss to the electrical power input. The heat load transported by the heat pipe was defined as the power output from the condenser calorimeter.

After the installation of all thermocouples and heaters the heat pipe was mounted to an adjustable height support frame with ceramic fiberboard brackets. The heat pipe was then processed on a specially-built heat pipe filling station. The heat pipe was evacuated to a pressure of  $10^{-7}$  torr and was initially filled with 43 grams of Grade T3N5 sodium. It was necessary to push the sodium into the heat pipe with argon gas, so the heat pipe was hot-processed to remove the noncondensable gas. The hot-processing procedure was performed by reattaching the sodium fill chamber to the heat pipe fill valve, connecting the fill chamber to a high vacuum source, and operating the heat pipe with the fill valve open until isothermal vapor temperatures were observed. The fill valve was then closed, and the heat pipe was ready for testing.

The high-temperature heat pipe with multiple heat sources was tested at Wright State University in a stainless steel vacuum chamber. Stainless steel is a standard material used in vacuum chamber construction because it exhibits very low outgassing characteristics under high vacuum, and vacuum tight welds are easily attainable when TIG welding is used. Chamber dimensions were chosen to provide sufficient room inside the chamber for the heat pipe instrumentation and the heater power leads, and to allow testing at various evaporator elevations. The chamber was built with hinged bulkheads at each end to allow easy access to the chamber interior, which were sealed with neoprene O-rings. The vacuum chamber evacuation system consisted of a 152-mm diffusion pump with a water-cooled baffle, an aluminum slide valve, and a 480 LPM mechanical pump. Vacuum pressure was monitored by a Bayard-Alpert type ionization gauge and a thermocouple gauge mounted to the chamber wall. Vacuum ports welded to the chamber wall were fitted with feed-throughs for the heater power leads, calorimeter water supply lines, and the heat pipe thermocouples. The chamber was also fitted with viewports to allow visual observation of the heat pipe during testing. Figure 1.3 shows the vacuum chamber operating system and auxiliary equipment used in the testing of the high-temperature heat pipe.

#### 1.4 RESULTS AND DISCUSSION

The high-temperature heat pipe with multiple heat sources was tested under many different operating conditions. The startup behavior for single and multiple evaporator operation both under vacuum and in air was investigated. The heat pipe was operated with two different fluid charges (30g and 43g), and was tested with evaporator elevations of 0, 1.4, 3.0, and 5.7 degrees against gravity. A complete summary of tests completed is

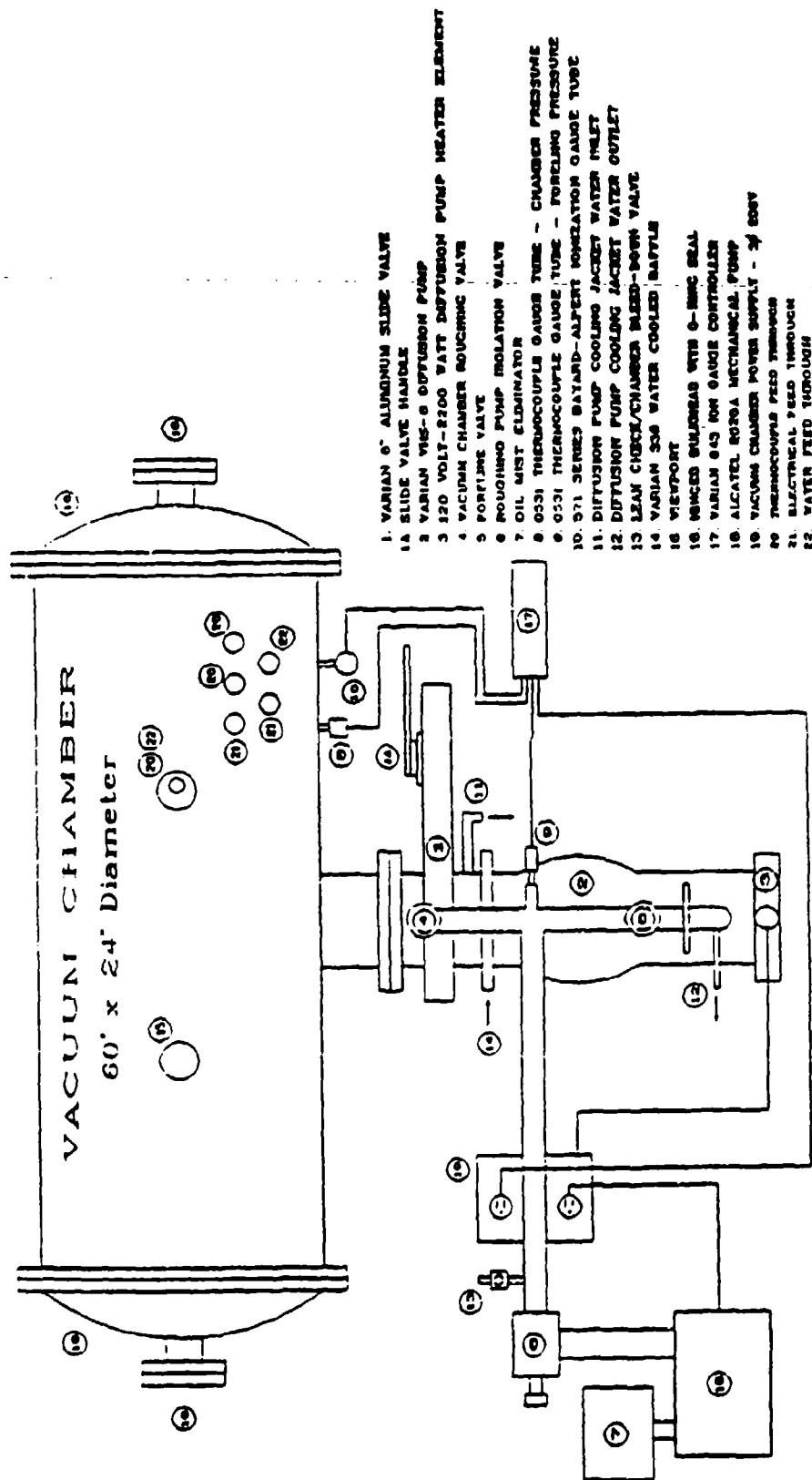


Figure 1.3 Vacuum Chamber Operating System

given in Table 1.1. The conditions contained in Table 1.1 are given for steady-state conditions, although the results presented here are for frozen startup (part I) and continuum transient and steady-state operation (part II), and include the following:

- A. The electrical input power to each active heater
- B. The individually measured power outputs from the evaporator, transport, and condenser section calorimeters
- C. The transport section vapor temperature
- D. The heat pipe fluid charge and evaporator elevation against gravity

The legend at the beginning of Table 1.1 contains explanations for the superscript notations used to identify specific operating conditions reached during each case. Superscripts 1 and 2 modify the case number, and indicate when continuum flow ( $T^* = 395^{\circ}\text{C}$ ) was reached in the entire vapor space, and when isothermal operation was attained, respectively. Superscripts 3, 4, and 5 are located adjacent to individual evaporator heater power listings, and indicate that the notated evaporator overheated from wick dryout, the heater reached the maximum allowable temperature ( $900^{\circ}\text{C}$ ), and the maximum power output from the power supply was reached, respectively.

The startup behavior of the high-temperature heat pipe in vacuum was always frontal in nature, with a sharp dropoff in temperature across the vapor front, and no pressure recovery in the condenser. This startup mode is well-established for a radiation-cooled condenser, being observed by

Merrigan et al. (1986), and Ponnappan (1990), among others. Deverall (1970) concluded that heat rejection by radiation is a self-compensating system and automatically controls the heat-rejection rate. In other words, the active length of the condenser is determined by the surface area necessary to reject the applied heat load. Even though sonic velocities may occur in the condenser, the heat pipe startup is not sonic limited for a radiation-cooled condenser. No startup failures were found during testing in vacuum, even with initial power input levels of 1263 watts to the heaters (case 1.9a). The time necessary to reach a steady-state from a frozen startup was found to be strictly dependent upon the initial heat load on the heat pipe. The startup time from the frozen state was dependent on the applied heat load because the input heat flux determined the evaporation rate at the liquid-vapor interface and the subsequent axial heat transport. The thermal mass of the heat pipe mounting assembly, radiation shields, calorimeters, and the thermal lag in the evaporator heaters also affected the startup time.

Since no startup failures were found during testing in vacuum, several tests were conducted with the heat pipe operating in air, which increased the heat rejection rate at the condenser by the addition of convective heat losses. Figures 1.4a and 1.4b present three-dimensional transient vapor temperature profiles during operation under vacuum (case 11) and in air (case 22) with only evaporator 1 active. Figures 1.5a and 1.5b are similar graphs during operation under vacuum (case 15) and in air (case 23) with only evaporator 2 active. Both sets of figures clearly show how the startup behavior of the heat pipe changed with the increased heat rejection at the condenser. The startup power inputs for the cases in air (529 and

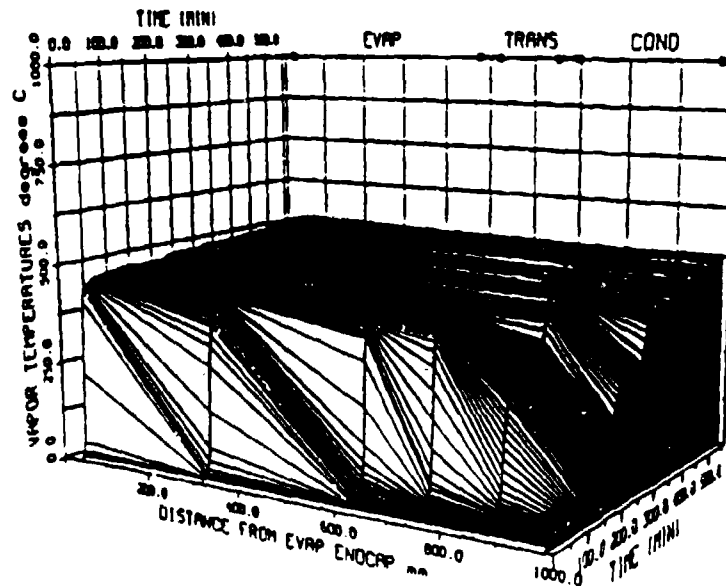


Figure 4a. Case 11, in vacuum

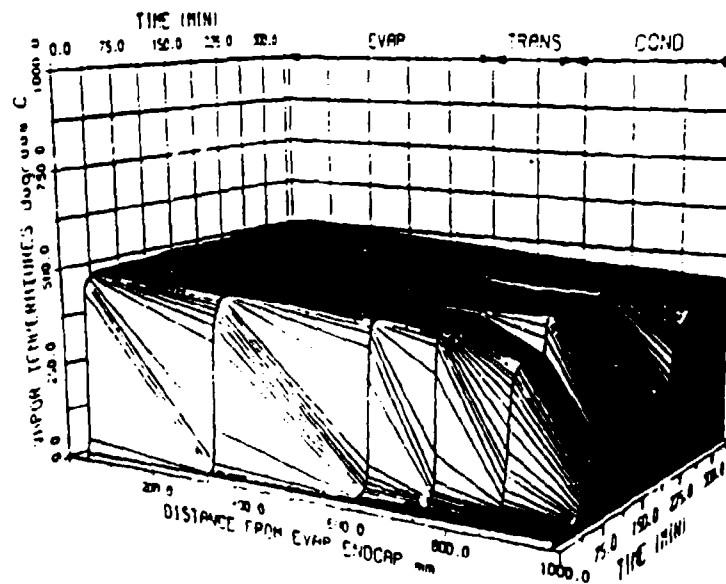


Figure 4b. Case 22, in air

Figure 1.4 Transient Axial Vapor Temperature Profiles With Evaporator 1 Active

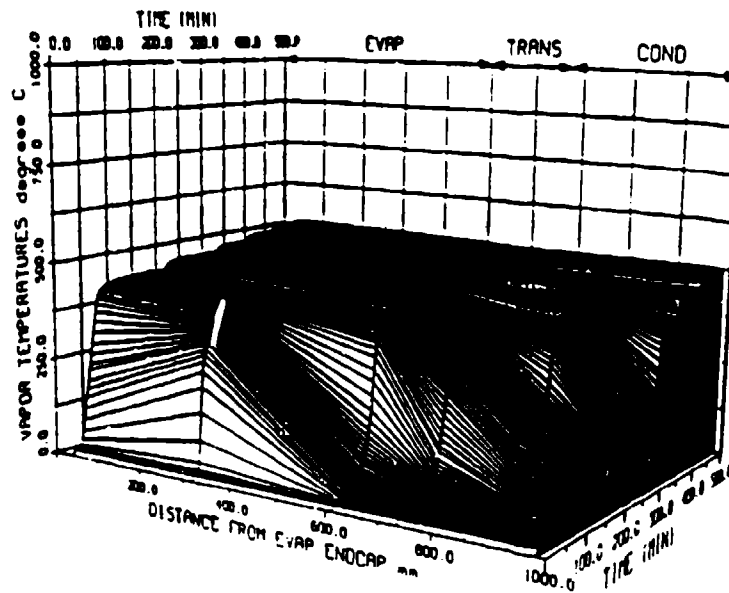


Figure 5a. Case 15, in vacuum

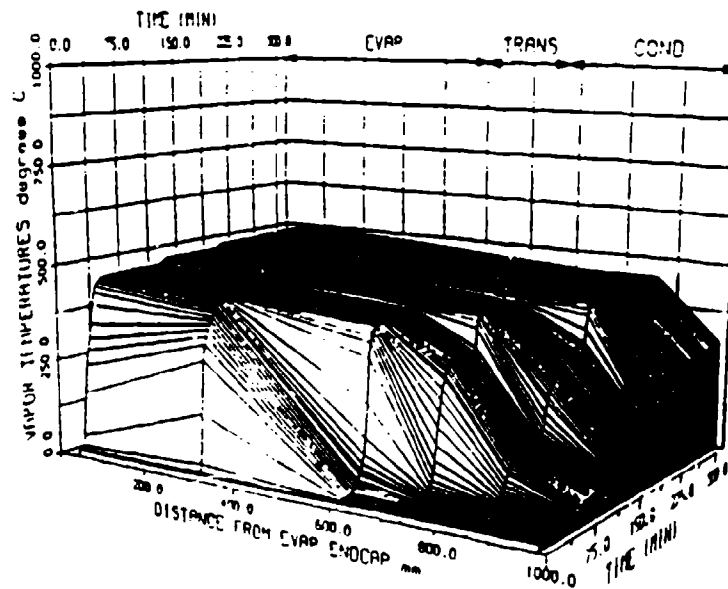


Figure 5b. Case 23, in air

Figure 1.5 Transient Axial Vapor Temperature Profiles With Evaporator 2 Active

394 watts) were much higher than those for startup under vacuum (311 and 205 watts), the axial temperature gradient in the condenser was much more pronounced, and supersonic vapor flow occurred within the condenser region. No startup failures were found during operation in air, although much higher power levels were required to attain continuum flow in the entire vapor space. The total energy balance for the heat pipe was maintained during operation in air. This was due to the radiation shield insulation in the evaporator and transport sections which effectively eliminated air exchange between the room and the heat pipe assembly, so there were minimal convection losses from the heat pipe assembly to the environment. Also, the heat pipe itself was mounted on ceramic board supports, so very little heat was lost by conduction.

Figure 1.6a presents the transient vapor temperatures versus time for a high-power startup with only evaporator 1 active under vacuum (case 14a), and in air (case 22a). The six vapor space thermocouples are given curve labels V1, V2, V3... etc., and each specific case is identified by the number to the right of the hyphen, i.e., V2-14 specifies vapor thermocouple #2 for case 14. Exact vapor space thermocouple locations are given in Figure 1.1. The transient vapor temperature profiles for the thermocouples located within the evaporator section, the transport section, and at the beginning of the condenser (V1, V2, V3, V4) show identical trends up to approximately 35 minutes from the initial power input, both under vacuum and in air. The heat pipe is well insulated in the evaporator and transport sections, and the presence of air within the insulation apparently has a negligible effect on the heat losses in these sections. The increased heat rejection rate at the condenser during operation in air

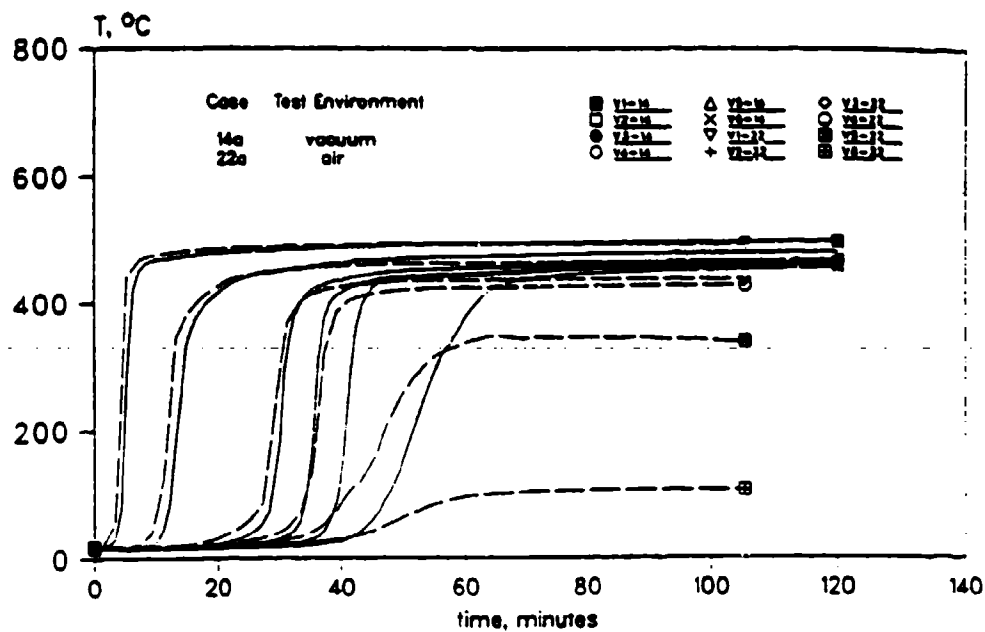


Figure 6a. Evaporator 1 active

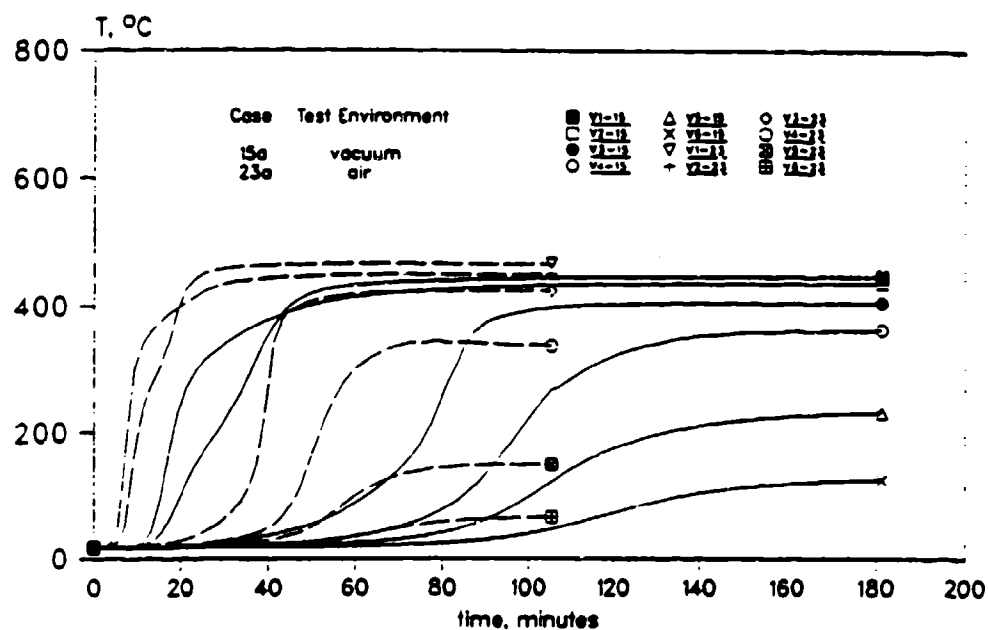


Figure 6b. Evaporator 2 active

Figure 1.6 Effects of Test Environment on Transient Vapor Temperatures During Startup

has a noticeable effect on the vapor temperatures within the condenser, shown by curves V5 and V6. Continuum flow was established in the entire heat pipe for startup under vacuum (case 14a), but during operation in air (case 22a) the end of the condenser is barely above the melting temperature of sodium. The startup of the heat pipe for single evaporator operation in air was definitely sonic limited, and the pressure drop in the condenser, as indicated from the steep dropoff in the vapor temperatures, shows that supersonic vapor flow existed within the condenser.

Figure 1.6b is a plot of transient vapor temperatures for startup with evaporator 2 active under vacuum (case 15a) and in air (case 23a). The vapor profiles show no similarities between the two cases, except for the first thermocouple located in the evaporator section (V1). Although an input power level of 205 watts was insufficient to reach continuum flow in the entire heat pipe for startup in vacuum, the final steady-state evaporator vapor temperatures were nearly the same as for case 23 (in air), which had a startup power level of 394 watts. The time necessary to reach steady-state under vacuum was almost twice as long as that in air because of the smaller heat rejection rate at the condenser. The slope of the transient condenser vapor temperatures for startup under vacuum shows the slower temperature rise to the final steady state. The case in air reached steady state within 105 minutes, but the vapor front became essentially stationary at a time of about 70 minutes, when the front entered the condenser and supersonic vapor flow occurred. The low condenser heat rejection rate during operation in vacuum apparently prevented supersonic vapor velocities and allowed the condenser to slowly rise in temperature to the final steady-state condition.

The startup behavior of the heat pipe with evaporators 3 or 4 active was quite different from a standard configuration heat pipe, where the evaporator is located at one end of the heat pipe. Figures 1.7a and 1.7b, three-dimensional plots of the transient axial vapor temperature profiles for cases 16 and 17, demonstrate that during startup with an evaporator located near the middle of the heat pipe the vapor flowed towards both the condenser and the evaporator end caps. When continuum flow was established in the entire evaporator section, the vapor flow assumed a 'normal' profile, where the evaporator section was nearly isothermal and a temperature gradient existed in the condenser section.

The transient axial vapor temperature profiles for several two-evaporator startups are given in Figures 1.8, 1.9a, and 1.9b. Figure 1.8 (case 19, evaporators 1 and 4 active) indicates that a large temperature drop existed between the two active evaporators during startup due to the sudden heat flux applied to the evaporator sections, and the heat losses in the inactive evaporator sections. The axial vapor temperature gradients in Figure 1.9a (case 20, evaporators 3 and 4 active) and Figure 1.9b (case 21, evaporators 2 and 3 active) show that during startup in vacuum<sup>1</sup> the vapor flow reached supersonic velocities in both directions, i.e., towards the evaporator end and towards the condenser end. The experimental setup had a certain effect on the degree of two-way vapor flow. The evaporator section of the heat pipe was insulated, but not truly

---

<sup>1</sup>The heater configurations of cases 20 and 21 were not repeated during testing in air, so an air-vacuum startup behavior comparison of these cases was not possible.

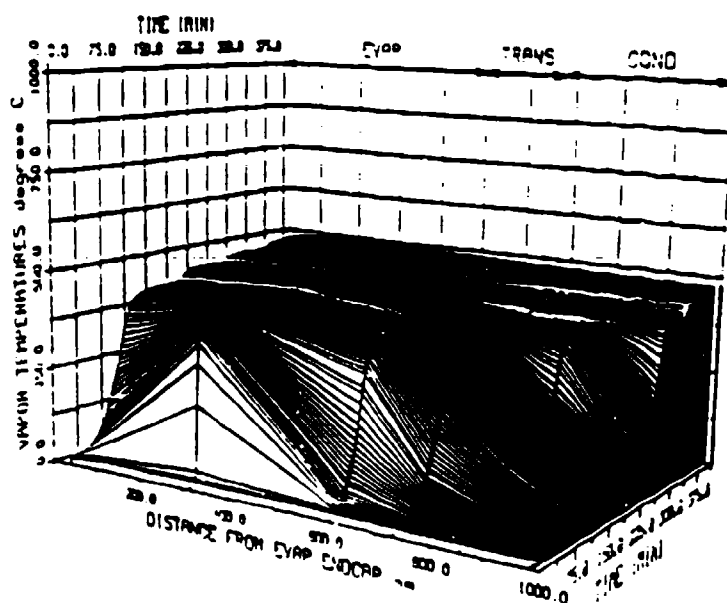


Figure 7a. Case 16, evaporator 3 active

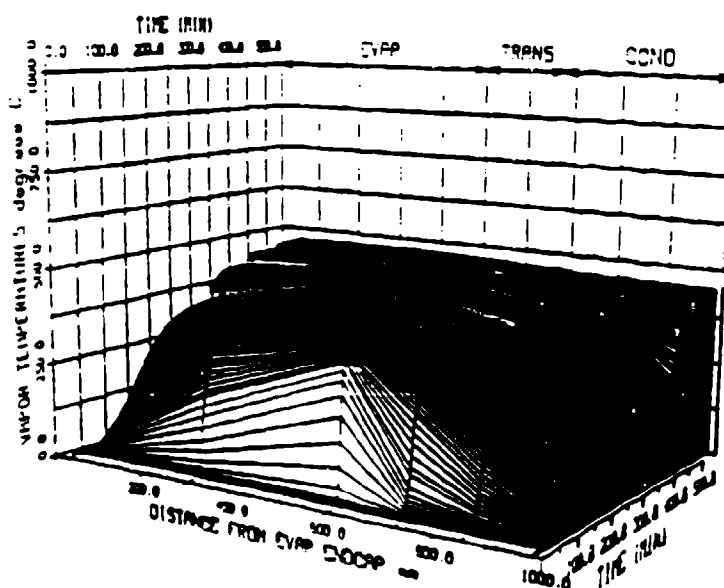


Figure 7b. Case 17, evaporator 4 active

Figure 1.7 Transient Axial Vapor Temperatures Profiles for One Evaporator Operation in Vacuum

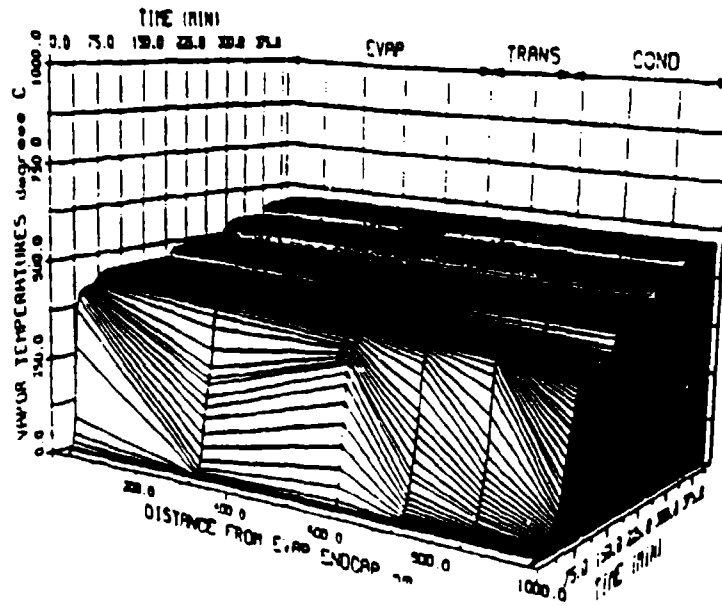


Figure 1.8 Transient Axial Vapor Temperature Profiles for Operation in Vacuum With Evaporators 1 and 4 Active

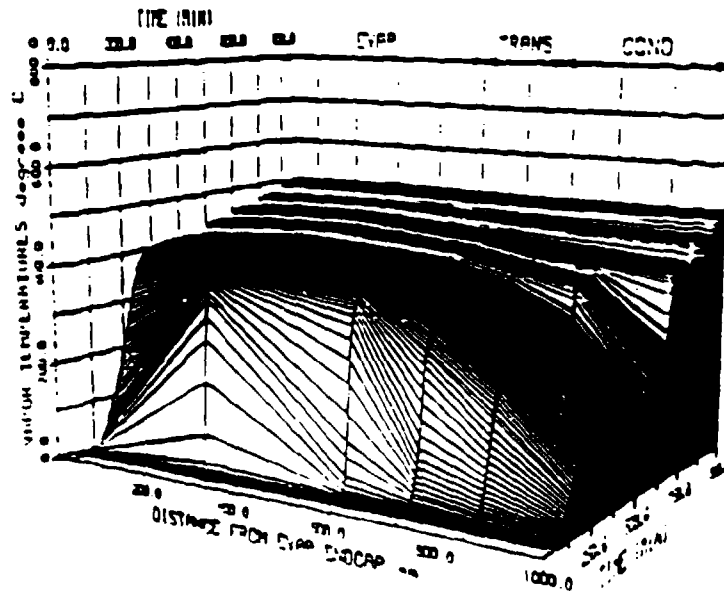


Figure 9a. Case 20. evaporators 3 and 4 active

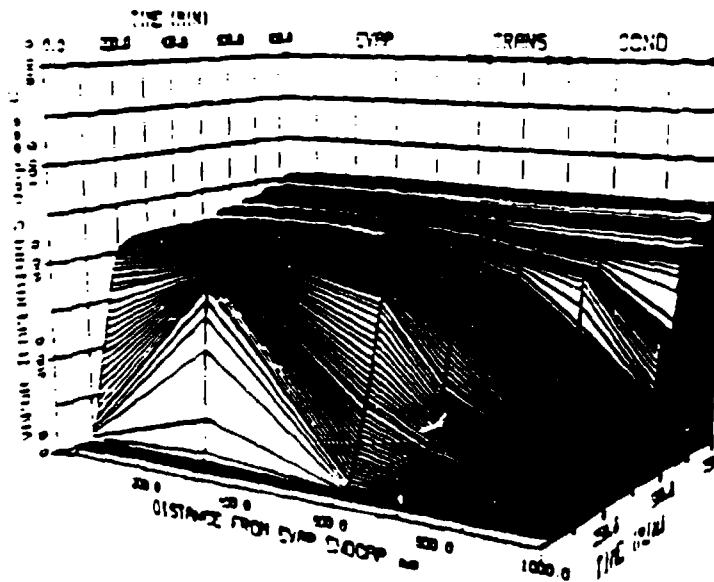


Figure 9b. Case 21. evaporators 2 and 3 active

Figure 1.9 Transient Axial Vapor Temperature Profiles for Two Evaporator Operation in Vacuum

adiabatic, so condensation occurred in the inactive areas of the evaporator section. The heat losses in the evaporator section contributed to the extreme temperature gradients between the active evaporators during startup. The three-dimensional two-evaporator startup graphs clearly show that after continuum flow was reached in the evaporator section, the evaporator vapor temperature remained relatively constant as the vapor front moved down the heat pipe. This behavior has also been observed by Sockol and Forman (1970) for a radiation-cooled lithium heat pipe.

### 1.5 CONCLUSIONS

A sodium/stainless steel heat pipe with a simple circumferential screen wick and multiple heat sources was successfully fabricated, processed, and tested, both in air and under vacuum. Detailed measurements of the heat pipe wall and vapor temperatures, multiple evaporator heat inputs, and steady-state heat losses from the evaporator, transport, and condenser sections were made. These tests showed that the startup behavior of a liquid metal heat pipe from the frozen state was greatly dependent upon the heat rejection rate at the condenser. Supersonic vapor velocities occurred in the condenser section during startup, and two-way vapor flow was observed in the evaporator section during several two-evaporator startups. No startup failures (evaporator dryout) were found for single or multiple evaporator operation in air or under vacuum, although startup in air was sonic limited until isothermal operation was reached.

The coil-on sheathed electrical resistance heaters used in the evaporator section were the primary limitation to finding the maximum heat transport capacity of the heat pipe, because approximately 40% of the input

power to the heaters was lost, and not transported to the heat pipe condenser. Even with radiation shield insulation, heat losses from the evaporator and transport sections were significant, but water-cooled calorimeters installed on each section of the heat pipe allowed energy balances approaching 100% to be made during steady-state testing.

---

## Section II

### AN ANALYSIS OF CONTINUUM TRANSIENT AND STEADY-STATE EXPERIMENTAL DATA WITH NUMERICAL PREDICTIONS OF HIGH-TEMPERATURE HEAT PIPES

#### 2.1 SUMMARY

The experimental data presented in Section I were analyzed concerning the heat pipe performance characteristics and design. Post-experiment examination of the loosely-wrapped screen wick revealed annular gaps both between the wick and the heat pipe wall and between adjacent screen layers, which greatly enhanced the maximum heat capacity of the heat pipe compared to the analytical capillary limit for a tightly-wrapped screen wick. A numerical simulation for the transient heat pipe performances including the vapor region, wick structure and the heat pipe wall is given. Numerical results for continuum transient and steady state operation with multiple heat sources were compared with experimental results and is in good agreement.

## 2.2 INTRODUCTION

The experimental profiles for the heat pipe startup from frozen state have been presented in Part I of this report. One of the objectives of the experimental study was to understand the transient and steady-state performance characteristics of the heat pipe, which are very important to heat pipe design and fabrication. In this part of the report, the experimental results of the performance characteristics for the continuum transient and steady-state operation of the heat pipe are presented and analyzed, and the performance limits for operation with varying heat fluxes and locations are determined. Another objective of the experimental study was to provide accurate and complete experimental results for the development and verification of numerical analysis models.

Transient thermal analyses of heat pipes are categorized in three basic types: Vapor flow in the core region including both continuum transient and free molecular conditions; transient liquid flow in the wick with the possibility of melting inside the wick as well as evaporation and condensation at the vapor/liquid interface; and transient heat conduction in the heat pipe wall. A recent detailed literature survey concerning the thermal analysis of heat pipes was given by Chen and Faghri (1990). This review covered both transient and steady operations as well as one- or two-dimensional modeling.

Jang et al. (1990) developed a comprehensive mathematical model and analysis of heat pipe startup from the frozen state. Different startup periods were described and the general mathematical formulation for each period was given. In an attempt to solve the governing equations, the

liquid flow in the porous media was neglected, and the vapor flow was assumed to be one-dimensional. No comparison was made with experimental results.

Cao and Faghri (1990) developed a transient two-dimensional compressible analysis for high-temperature heat pipes with a pulsed heat input. In this model, they also neglected the liquid flow in the wick by assuming the wick to be a pure conduction problem with an effective thermal conductivity.

All of the previous transient models either were not compared to any experimental data or were only compared to a simulated heat pipe using air flow in a porous pipe. In this paper, the numerical model of Cao and Faghri (1990) was adapted to the high-temperature heat pipe with multiple heat sources and sinks. The compressible two-dimensional transient mass, momentum, and energy equations in vapor region, and the energy equations in the wick and wall regions were solved as a conjugate problem. This model also eliminated the use of any empirical model for friction coefficients used in the one-dimensional transient vapor flow models. The transient experimental results for the vapor temperature along the heat pipe with multiple heat sources and sinks is also be compared with the proposed model.

### **2.3 CHARACTERISTICS OF CONTINUUM TRANSIENT AND STEADY-STATE OPERATIONS**

The experimental heat pipe (Section I) was operated with two different fluid charges (30g and 43g). At first it appeared that the change in the fluid charge had a major effect on the steady-state operating temperature

of the heat pipe. Figure 2.1 shows steady-state axial vapor temperature profiles for four-evaporator operation in vacuum before and after the removal of the excess sodium. The steady-state vapor temperature was about 25°C colder with a fluid charge of 30 grams versus the same test with 43 grams. The actual cause of the lower temperatures in the 30-gram fluid charge cases was a slight increase in the emissivity of the heat pipe wall. Sodium was removed from the heat pipe during isothermal operation in air, and an oxide with a higher emissivity was formed on the heat pipe wall. Any effect of the fluid charge on the steady-state vapor temperatures would be negligible since the temperature of a thin liquid pool in the condenser would be close to the equilibrium temperature. Although the operating temperature is a function of the wall emissivity, the total time necessary for startup from the frozen state to a steady-state condition did not change by any significant amount for the two fluid charges, since the heat capacity of the excess sodium was quite small when compared to the thermal mass of the heat pipe assembly.

One of the primary interests in testing the high-temperature heat pipe with multiple heat sources was to determine the capillary limits for operation with varying heat fluxes and locations. Since the capillary limit was not found with the heat pipe horizontal, it was necessary to decrease the available capillary pressure in the wick. This was accomplished by raising the evaporator end of the heat pipe and operating against gravity. Tests were performed with evaporator elevations of 1.4°, 3.0°, and 5.7°. One interesting result of raising the evaporator end of the heat pipe was a decrease in the operating temperature, as shown in Figure 2.2, which occurred during operation both in air and under vacuum.

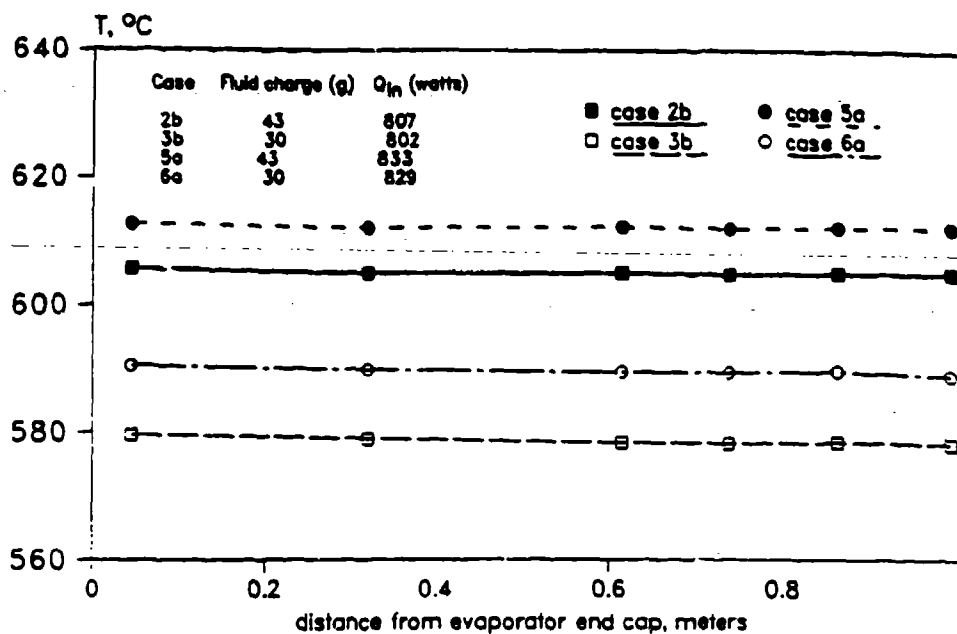


Figure 2.1 Effect of Emissivity on Steady-State Axial Vapor Temperature Profiles

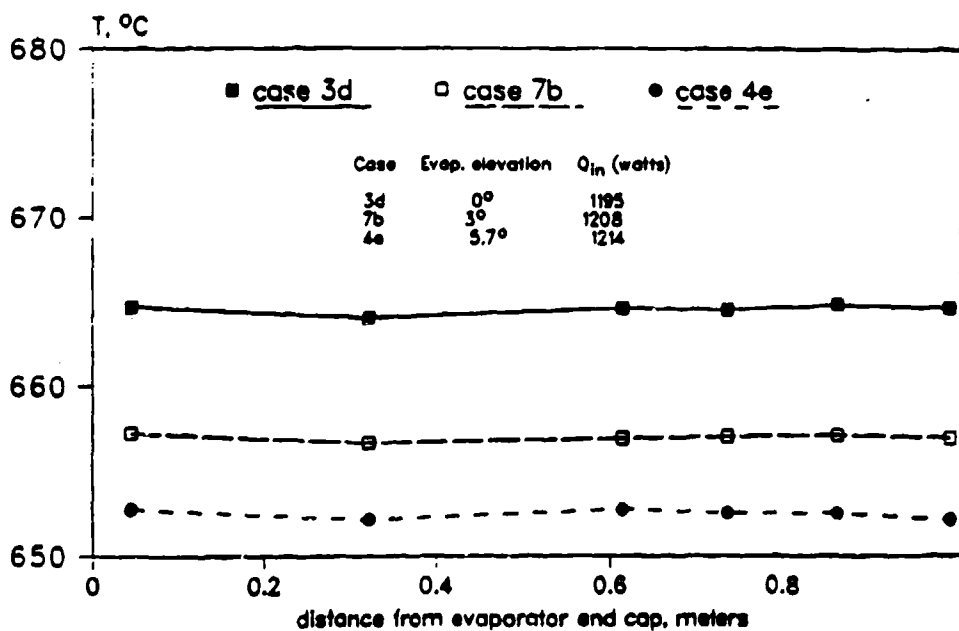


Figure 2.2 Effect of Evaporator Elevation on Steady-State Axial Vapor Temperature Profiles

Previous high-temperature experimental data was available to support the observed temperature drop with increased evaporator elevation. Shaubach et al. (1990) observed a reduction in the temperature drop between the wick-wall interface and the vapor core of a copper-water heat pipe when comparing data from tests performed at evaporator elevations of 5 cm and 30 cm against gravity. When the wick liquid pressure is reduced by the gravity head, the corresponding liquid saturation temperature is reduced, therefore the operating temperature of the heat pipe drops. Figure 2.2 shows that in the case of a high-temperature heat pipe with multiple heat sources the vapor temperature is also reduced by elevating the evaporator end of the heat pipe.

A frequently encountered problem when testing heat pipes is the apparent sensitivity of the heat pipe to sudden increases in the applied heat loads, although the problem is more likely to occur in an arterial or composite wick heat pipe. The multiple heat source heat pipe had a simple circumferential screen wick, and showed no sensitivity to the startup input power level, or to large power increases from a steady-state condition. Figure 2.3a presents steady-state axial vapor temperature profiles for four evaporator operation in vacuum, and shows that the final steady-state temperature reached was independent of the startup power level. Figure 2.3b shows the same phenomenon for single evaporator operation in air. The fact that the initial power level and the size of subsequent power increases had no effect on the final steady-state temperature of the heat pipe (with the final boundary conditions being the same) proves that the experimental results are repeatable.

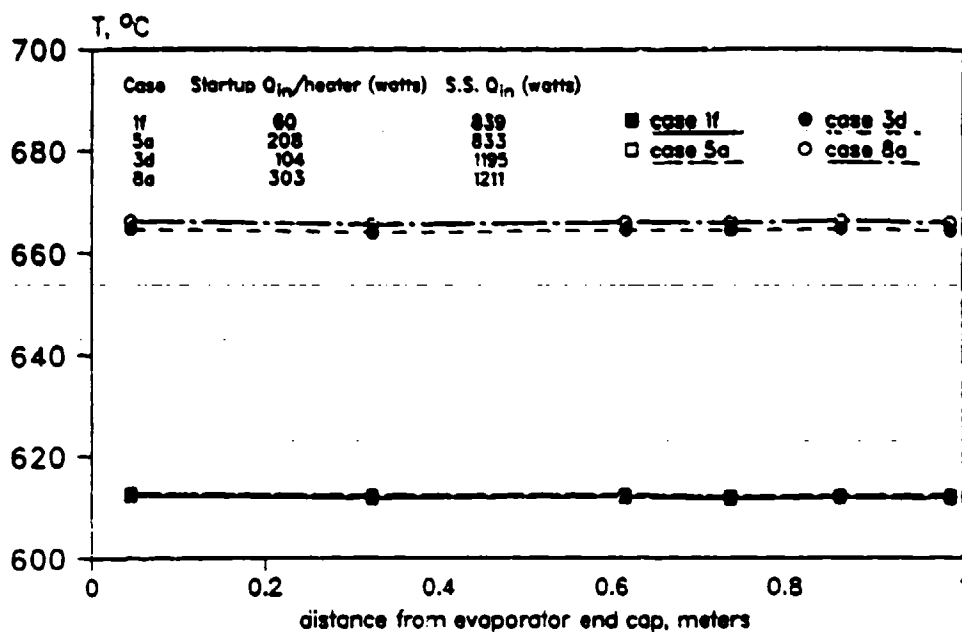


Figure 3a. Four evaporator operation

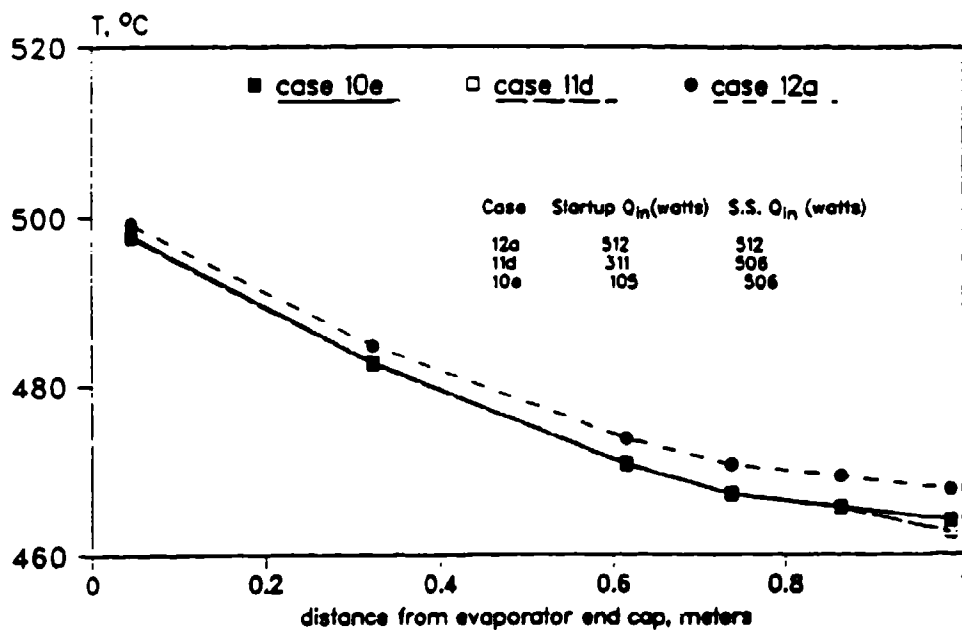


Figure 3b. One evaporator operation

Figure 2.3 Effect of Startup Power Levels on Steady-State Axial Vapor Temperature Profiles

Figures 2.4 through 2.7 are plots of the steady-state condenser power output versus the transport section vapor temperature during operation both in air and under vacuum for various single-evaporator cases, and their corresponding steady-state vapor temperature profiles. Also shown are the condenser radiation heat-transfer limit (calculated as the maximum radiation heat transfer from the condenser surface area for a given condenser wall temperature), and the heat pipe entrainment, sonic, and capillary limit curves. The heat pipe operating limits were calculated from the standard equations found in Chi (1976), assuming that only one evaporator was active. During startup in vacuum the heat pipe operated along the sonic limit until isothermal axial vapor temperatures were achieved (shown in Figures 2.4a through 2.7a), then followed the condenser radiation heat transfer limit. Startup in air always followed the sonic limit curve, even after isothermal vapor temperatures were achieved because of additional heat losses at the condenser that are due to natural convection.

Initial design calculations, based on the standard equations contained in Chi (1976), indicated that the maximum capillary limit for the heat pipe, operating horizontally with evaporator 1 active, should have been approximately 250 watts. The highest condenser power output attained for one-evaporator operation was 357 watts, at an evaporator elevation of  $1.4^{\circ}$  (case 13d), but heater temperature limitations prevented any further power increases. In case 28h, operation in air at an evaporator elevation of  $5.7^{\circ}$ , it appeared that the capillary limit was found for four-evaporator operation. At the time evaporator 1 started to overheat, as shown in Figure 2.8, the total heat input to the heat pipe was 2409 watts. The

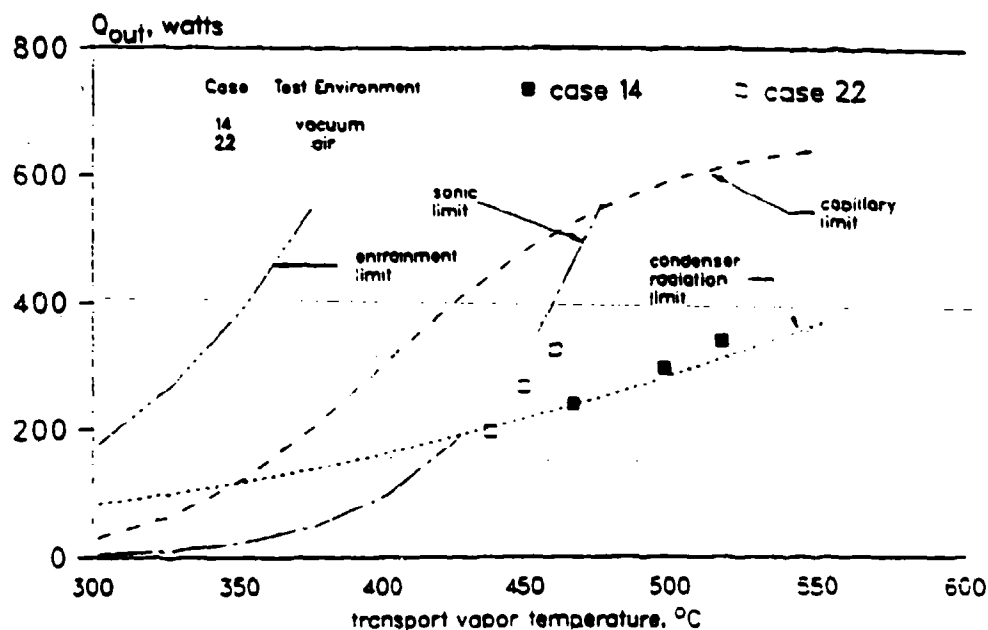


Figure 2.4a Axial Heat-Transfer Limits Versus Transport Vapor Temperature for Operation in Air and Vacuum With Evaporator 1 Active

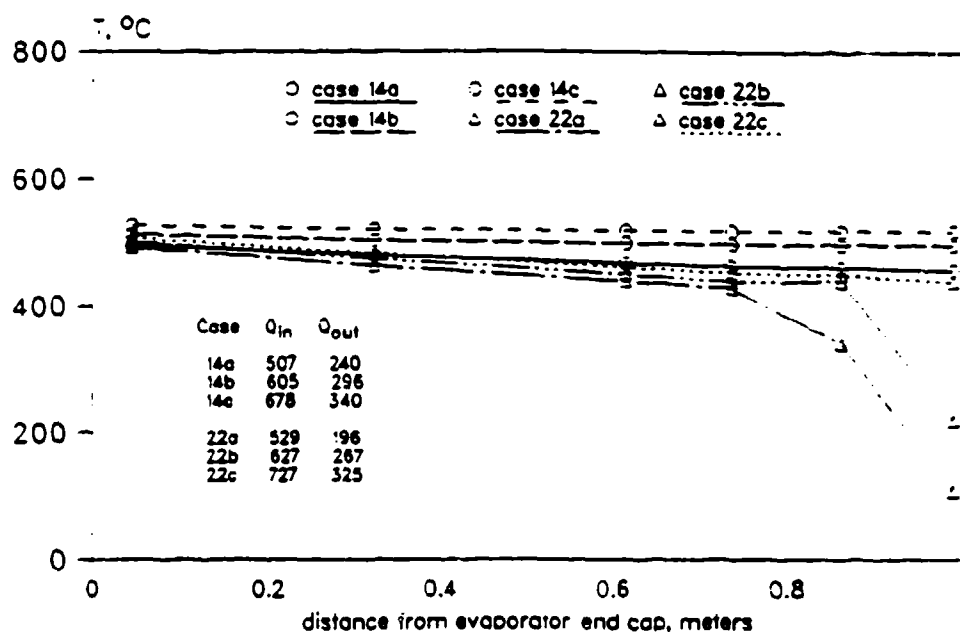


Figure 2.4b Steady-State Axial Vapor Temperature Profiles for Operation in Air and Vacuum With Evaporator 1 Active

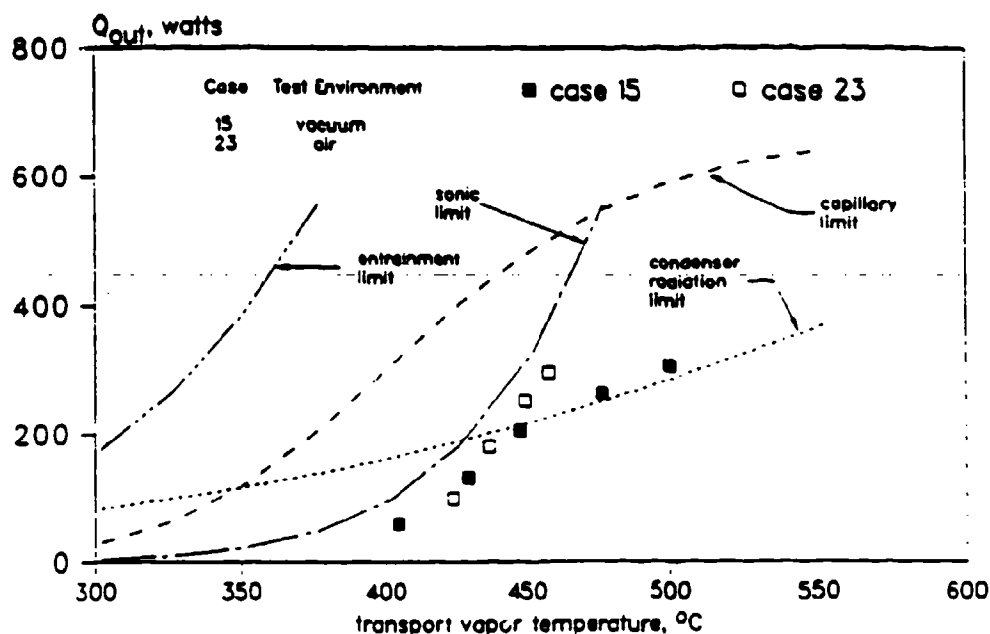


Figure 2.5a Axial Heat-Transfer Limits Versus Transport Vapor Temperature for Operation in Air and Vacuum With Evaporator 2 Active

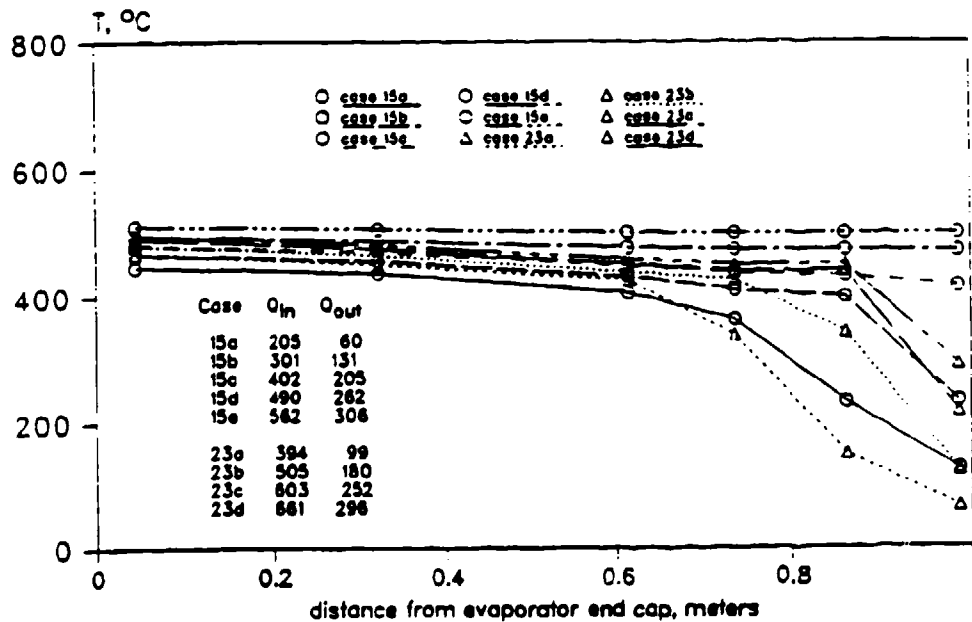


Figure 2.5b Steady-State Axial Vapor Temperature Profiles for Operation in Air and Vacuum With Evaporator 2 Active

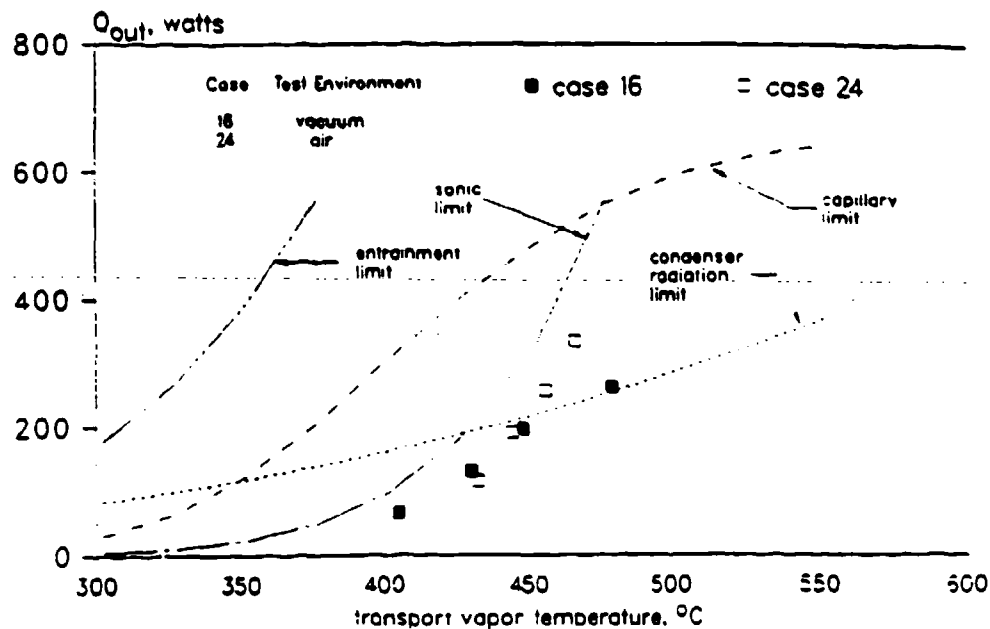


Figure 2.6a Axial Heat-Transfer Limits Versus Transport Vapor Temperature for Operation in Air and Vacuum With Evaporator 3 Active

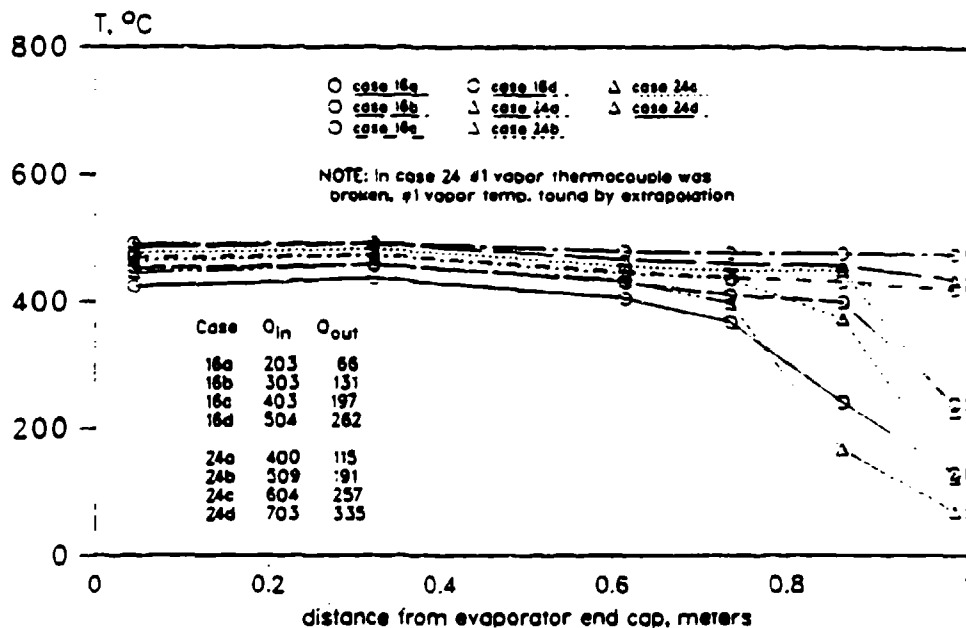


Figure 2.6b Steady-State Axial Vapor Temperature Profiles for Operation in Air and Vacuum With Evaporator 3 Active

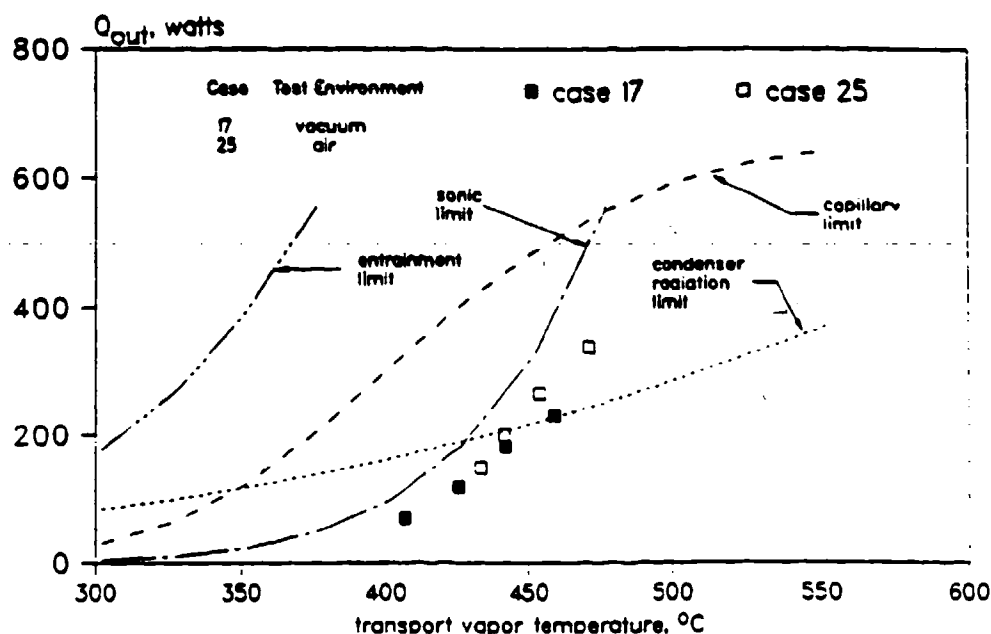


Figure 2.7a Axial Heat-Transfer Limits Versus Transport Vapor Temperature for Operation in Air and Vacuum With Evaporator 4 Active

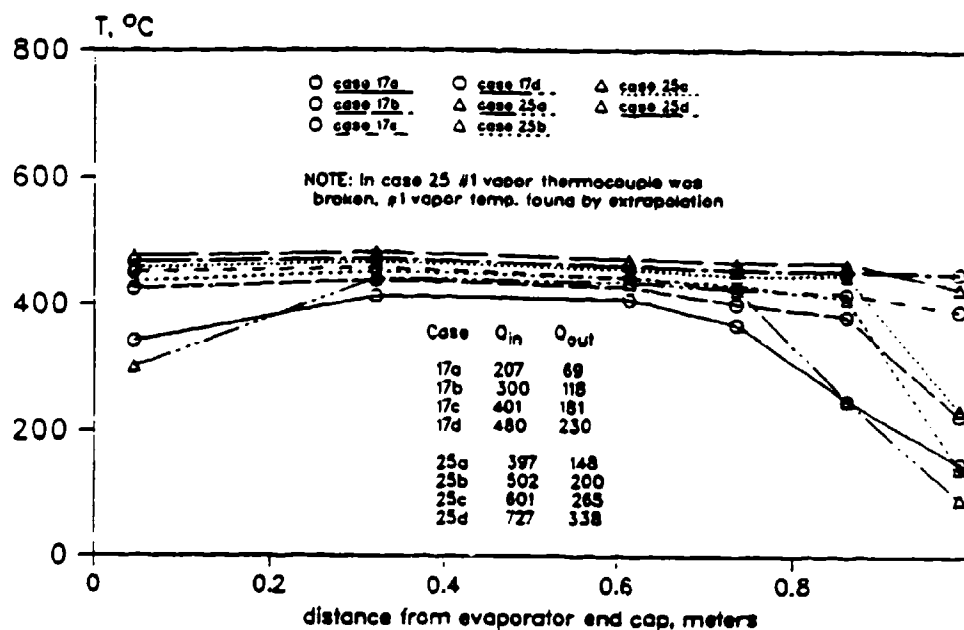


Figure 2.7b Steady-State Axial Vapor Temperature Profiles for Operation in Air and Vacuum With Evaporator 4 Active

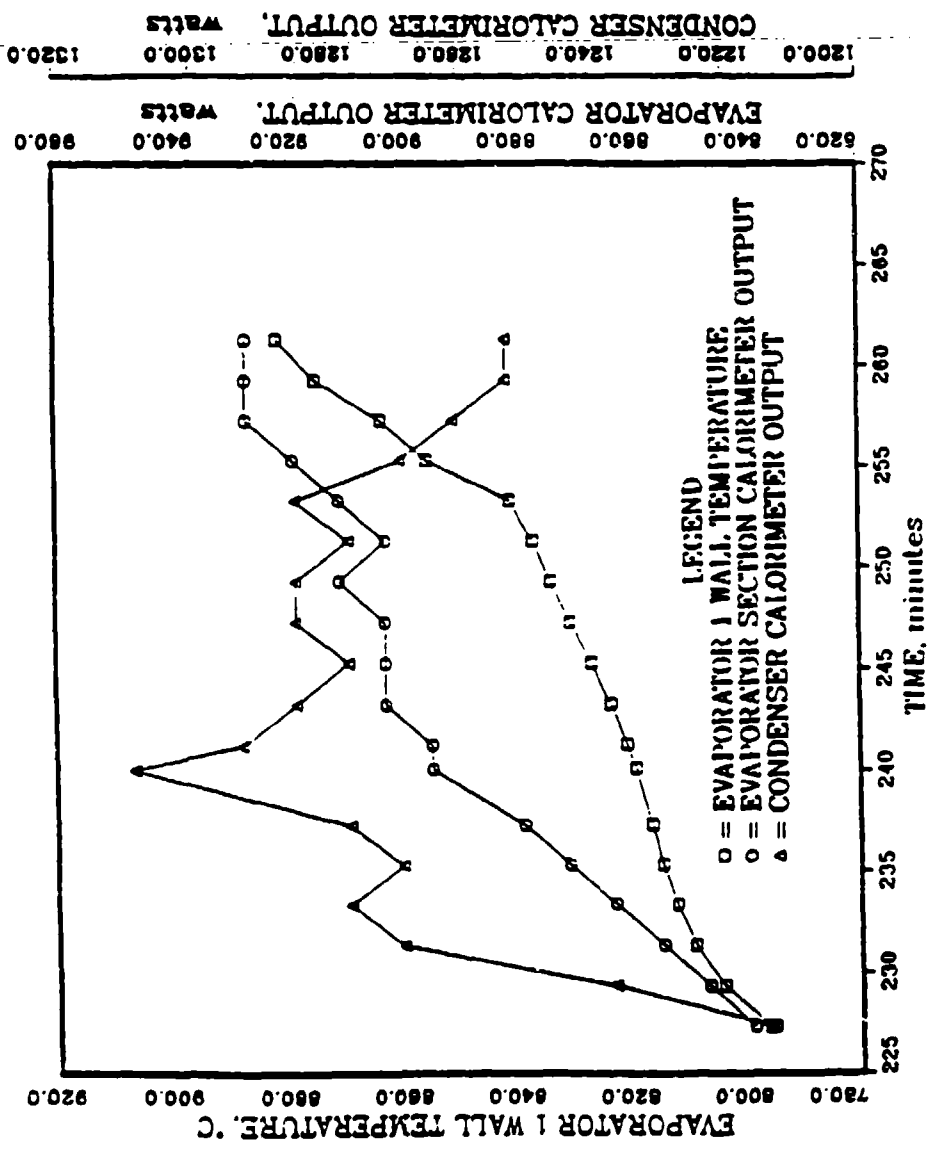


Figure 2.8 Evaporator 1 Dryout For Case 28h Total Power in  
 2409 Watts, Operation in Air With 5.7° Evaporator  
 Elevation

condenser power output peaked at 1309 watts, then suddenly began to drop off, while the evaporator calorimeter output and the evaporator 1 wall temperature continued to rise. The dryout limit data was somewhat tainted by the fact that a pocket of gas started to appear at the end of the condenser vapor space. The test was immediately halted, and an attempt was made to remove this gas from the heat pipe. During the gas removal procedure a even larger quantity of gas suddenly appeared within the condenser vapor space, indicating a possible leak in the heat pipe. Since the heat pipe was being operated in air, any oxygen that entered the heat pipe through the apparent leak would immediately oxidize the sodium and effectively ruin the heat pipe, so all testing was stopped. The heat pipe was disassembled, and the sodium was dissolved with methanol. The heat pipe container and end cap welds were leak-checked with a helium mass-spectrometer leak-detector and no leaks were found.

Post-experiment examination of the heat pipe wick showed that uneven annular gaps existed between the wick and the heat pipe wall, and in places between adjacent layers of screen. The existence of an annulus meant that the heat capacity of the heat pipe was much higher than the design power level, and the heaters were undersized as a result. Examination of the wick under evaporator 1 revealed slight corrosion and a contaminant deposit approximately 7 mm in diameter on the wick surface. A qualitative elemental identification on the contamination was made at Wright State University using a Transmission Electron Microscope. and the contaminant was determined to be composed of copper. The sodium used in the high-temperature heat pipe with multiple heat sources was delivered with a copper content of 5 to 20 ppm, according to the manufacturer. Given the

quantity of copper contamination found in the heat pipe wick it is not plausible that the copper content of the sodium was the sole source of the contamination. At some point in the heat pipe fabrication or fluid loading procedures a small piece of copper must have been introduced to the heat pipe system. Merrigan et al. (1984), Keddy and Martinez (1982), and Tanaka et al. (1990) have previously reported that severe damage can occur in a screen wick from local dryout and evaporator overheating. The combination of the copper contamination and the wick dryout must have led to the formation of the non-condensable gas and the wick corrosion observed in the heat pipe. No gas was observed in the heat pipe prior to the case 28h wick dryout.

## 2.4 NUMERICAL MODELING AND PREDICTIONS

The multiple-evaporator heat pipe configuration and coordinate system for the numerical modeling is schematically shown in Fig. 2.9. The wick is saturated with the liquid phase of the working fluid and the remaining volume of the pipe contains the vapor phase. Heat applied in the evaporators causes the liquid to vaporize into the vapor space. The vapor flows to the condenser and releases the latent heat as it condenses. The released heat is rejected into the environment by radiation or convection from the outer condenser surface.

### 2.4.1 Governing Equations

The experiment conducted by Bowman (1987) showed that the vapor flow was always laminar in the evaporator, while it might become turbulent at the condenser when the axial Reynolds number  $Re$  is relatively high ( $Re > 2000$ ). For the experiment conducted in this paper, the Reynolds number of

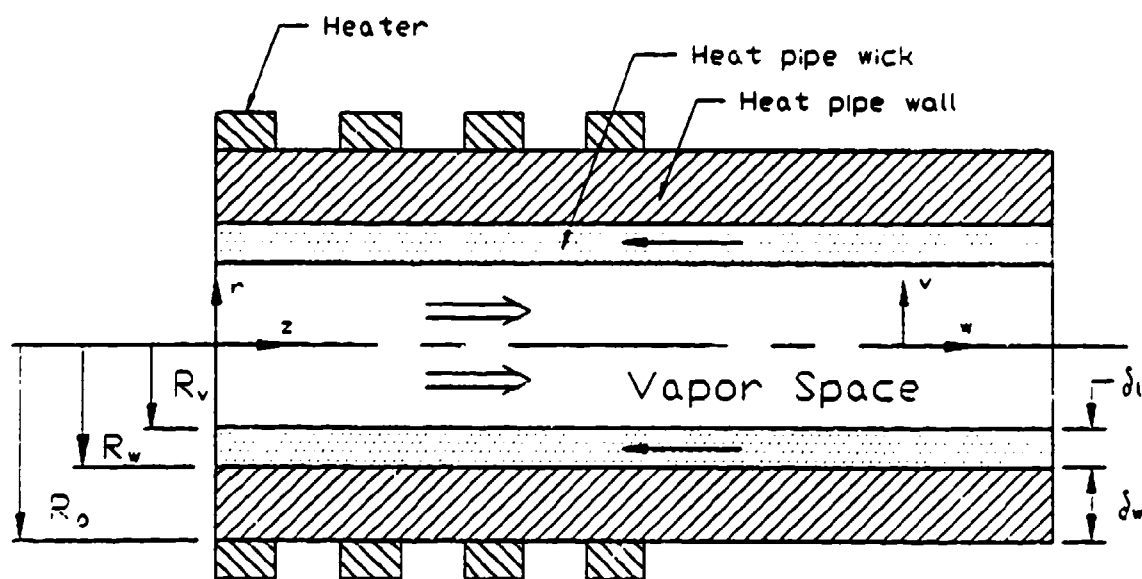


Figure 2.9 The Multiple - Evaporator Heat Pipe and Coordinate System

the vapor flow is relatively low (on the order of 200), therefore, the vapor flow can be assumed to be laminar along the entire heat pipe. The governing equations for transient compressible laminar vapor flow with constant viscosity are given as follows (Ganic et al., 1985).

$$\frac{\partial \rho}{\partial t} + \frac{1}{r} \frac{\partial}{\partial r} (\rho r v) + \frac{\partial}{\partial z} (\rho w) = 0 \quad (2.1)$$

$$\begin{aligned} \frac{\partial(\rho v)}{\partial t} + \frac{1}{r} \frac{\partial}{\partial r} (\rho r v^2) + \frac{\partial}{\partial z} (\rho v w) = & - \frac{\partial p}{\partial r} + \frac{4}{3} \mu \frac{1}{r} \frac{\partial}{\partial r} (r \frac{\partial v}{\partial r}) + \mu \frac{\partial^2 v}{\partial z^2} \\ & + \mu (\frac{1}{3} \frac{\partial^2 w}{\partial z \partial r} - \frac{4}{3} \frac{v}{r^2}) \end{aligned} \quad (2.2)$$

$$\begin{aligned} \frac{\partial(\rho w)}{\partial t} + \frac{1}{r} \frac{\partial}{\partial r} (\rho r v w) + \frac{\partial}{\partial z} (\rho w^2) = & - \frac{\partial p}{\partial z} + \mu \frac{\partial}{\partial r} (r \frac{\partial w}{\partial r}) + \frac{4}{3} \mu \frac{\partial^2 w}{\partial z^2} \\ & + \frac{1}{3} \mu (\frac{1}{r} \frac{\partial v}{\partial z} + \frac{\partial^2 v}{\partial z \partial r}) \end{aligned} \quad (2.3)$$

$$\rho c_p (\frac{\partial T}{\partial t} + v \frac{\partial T}{\partial r} + w \frac{\partial T}{\partial z}) = k [\frac{1}{r} \frac{\partial}{\partial r} (r \frac{\partial T}{\partial r}) + \frac{\partial^2 T}{\partial z^2}] + \frac{Dp}{Dt} + \mu \Phi \quad (2.4)$$

where

$$\Phi = 2 [(\frac{\partial v}{\partial r})^2 + (\frac{v}{r})^2 + (\frac{\partial w}{\partial z})^2] + (\frac{\partial v}{\partial z} + \frac{\partial w}{\partial r})^2 - \frac{2}{3} [\frac{1}{r} \frac{\partial}{\partial r} (r v) + \frac{\partial w}{\partial z}]^2$$

The equation of state is given by

$$p = \rho R T \quad (2.5)$$

The heat transfer through the heat pipe wall is purely by conduction.

The corresponding governing equation is:

$$(\rho c_p)_w \frac{\partial T}{\partial t} = k_w \left[ \frac{1}{r} \frac{\partial}{\partial r} \left( r \frac{\partial T}{\partial r} \right) + \frac{\partial^2 T}{\partial z^2} \right] \quad (2.6)$$

The analysis of Cao and Faghri (1990) showed that the liquid flow in the wick had a negligible effect on the temperature distribution in the heat pipe. In this paper, the model of Cao and Faghri (1990) is adopted, and the governing equations for the wick region can be written as

$$(\rho c_p)_{\text{eff}} \frac{\partial T}{\partial t} = k_{\text{eff}} \left[ \frac{1}{r} \frac{\partial}{\partial r} \left( r \frac{\partial T}{\partial r} \right) + \frac{\partial^2 T}{\partial z^2} \right] \quad (2.7)$$

where

$$(\rho c_p)_{\text{eff}} = \omega (\rho c_p)_\ell + (1 - \omega) (\rho c_p)_s$$

$$k_{\text{eff}} = k_\ell [k_\ell + k_s - (1 - \omega) (k_\ell - k_s)] / [k_\ell + k_s + (1 - \omega) (k_\ell - k_s)]$$

#### 2.4.2 Boundary Conditions

At both ends of the heat pipe, the no-slip condition for velocity and the adiabatic condition for temperature are applied. At  $z = 0$  and  $L$ :

$$v = w = 0 \quad (2.8)$$

$$\frac{\partial T}{\partial z} = 0$$

At the centerline,  $r = 0$ , the symmetry condition implies:

$$\frac{\partial v}{\partial r} = 0, \quad v = 0 \quad (2.9)$$

$$\frac{\partial T}{\partial r} = 0$$

The temperature at the vapor-liquid interface is assumed to be the saturation temperature corresponding to the interface pressure:

$$T_i = 1 / \left( \frac{1}{T_o} - \frac{R}{h_{fg}} \ln \frac{p_i}{p_o} \right) \quad (2.10)$$

where  $p_o$  and  $T_o$  are the reference saturation temperature and pressure.

The interface velocities at  $r = R_v$  are:

$$v_i = (-k_{eff} \frac{\partial T_\ell}{\partial r} + k_v \frac{\partial T_v}{\partial r}) / h_{fg} \rho_i \quad (2.11)$$

$$w = 0$$

The term  $k_v(\partial T_v / \partial r)$  in eqn. (2.11) can be neglected by an order of magnitude analysis. At the condenser interface, vapor condenses and releases its latent heat energy. In order to simulate this process, a heat source

$$q_i = h_{fg} \rho_i v_i \quad (2.12)$$

was applied at the interface grids on the wick side. The suction mass flux  $\rho_i v_i$  can be obtained by a mass balance over the interface grids on the

vapor side.

The boundary condition at the wick-wall interface  $r = R_v$  is:

$$k_w \frac{\partial T}{\partial r} = k_{\text{eff}} \frac{\partial T}{\partial r} \quad (2.13)$$

For the outer pipe wall surface  $r = R_o$ :

evaporator:

$$k_w \frac{\partial T}{\partial r} \Big|_{r=R_o} = q_e \quad (2.14)$$

adiabatic:

$$\frac{\partial T}{\partial r} \Big|_{r=R_o} = 0 \quad (2.15)$$

condenser:

$$-k_w \frac{\partial T}{\partial r} \Big|_{r=R_o} = \begin{cases} h(T_w - T_a) & \text{(convection)} \\ \epsilon \sigma T_w^4 & \text{(radiation)} \end{cases} \quad \begin{matrix} (2.16a) \\ (2.16b) \end{matrix}$$

where  $h$  is the convective heat-transfer coefficient,  $T_w$  and  $T_a$  are the outer wall surface and environment temperatures, respectively,  $\epsilon$  is the emissivity and  $\sigma$  is the Stefan-Boltzmann constant.

### 2.4.3 Numerical Procedure

The vapor flow was solved by employing the SIMPLE algorithm (Patankar, 1980; Patankar 1988). The discretization equations for  $w$ ,  $v$ ,  $T$  and  $p'$  have the general form

$$a_p \phi_p = a_E \phi_E + a_W \phi_W + a_N \phi_N + a_S \phi_S + b \quad (2.17)$$

A combination of the direct method (TDMA) and the Gauss-Seidel method was employed to solve the discretization equations. The pressure was chosen as a dependent variable and the equation of state  $\rho = p/RT$  was directly applied to obtain the vapor density while iterating.

At both ends of the heat pipe, the no-slip boundary condition leads to the prescribed velocity boundary conditions with  $w = v = 0$ . Since no boundary pressure is specified, and all the boundary coefficients in the pressure correction  $p'$  equation are zero, the  $p'$  equation is left without any means of establishing the absolute value of  $p'$ . In this case, the interface value of  $p'$  at the condenser end was assigned to zero. The absolute value of the vapor pressure at this point was calculated using the temperature of the liquid-vapor interface at the liquid side and the Clausius-Clapeyron equation. The absolute values of the vapor pressure along the heat pipe were also adjusted according to the value at this point during the iterations. The sequence of numerical steps was as follows:

1. Initialize the temperature, velocity, and pressure fields. The density values for the vapor are obtained from the current vapor pressure and temperature fields through the equation of state.
2. Calculate the vapor-liquid interface mass velocity  $v_i \rho_i$  using eqn. (2.11) and the previous temperature field. Calculate the interface vapor temperature using the Clausius-Clapeyron equation (eqn. (2.10)).
3. Solve the vapor momentum equation to obtain  $v^*$  and  $w^*$ .
4. Solve the  $p'$  equation and update the current vapor pressure field.

5. Calculate  $v$ ,  $w$  from their starred values using the velocity correction formulas.
6. Calculate the heat source term, eqn. (2.12), applying the mass balance over the interface grids on the vapor side to obtain mass flux  $v_i \rho_i$ .
7. Solve the temperature field for the wick, wall, and vapor regions.
8. Steps (1) - (7) are repeated until convergence is reached for each time step.

#### 2.4.4 Numerical Predictions

The numerical calculations for the transient heat pipe performance were made with the heat pipe configuration shown in Fig. 2.1 presented in Part I of this report. The left end of evaporator 1 was taken to be  $z = 0$ , and the right end of the condenser calorimeter was taken to be  $z = L$ , which made the total length of the numerically simulated heat pipe to be 0.96 m. Different grid sizes for the same problem were tested and it proved that the numerical solutions were essentially independent of grid size used. A change from a grid size of  $(14 \times 54)$  to  $(24 \times 107)$ , for example, resulted in a maximum change in vapor temperature less than 1%, and a maximum vapor velocity change of less than 3%. The present numerical scheme has some restrictions on the radial grid size especially in the wick structure region. The interface velocities are computed using eqn. (2.11). If the effective thermal conductivity  $k_{\text{eff}}$  is large, the temperature difference between the adjacent grids in the wick is very small. As a result, a large numerical error may arise when estimating the temperature gradients in the wick. However, this is not a problem in practice. Since the radius of the vapor core and the thickness of the wick are very small (about 10 mm and 0.5 mm, respectively), a relatively small number of grids in these regions

will simulate the heat pipe performance with sufficient accuracy.

Figure 2.10 compares the numerical vapor temperatures for different time periods with the experimental data for cases 6b-6c presented in Part I of this report. The curve labelled with  $t = 0.0$  is the steady-state condition corresponding to case 6b. In this case, the four evaporators were active with a total power input of  $Q_{in} = 1200$  W. The boundary condition at the condenser was radiative corresponding to eqn. (2.16b). At  $t = 0$ , the power input at the evaporators was suddenly increased to  $Q_{in} = 1300$  W. The transient response of the vapor temperature is presented in the same figure. After about 30 minutes, the heat pipe reached another steady state corresponding to case 6c. The numerical solutions agree very well with the experimental data. The above numerical calculation were made with a grid size of 54 (axial)  $\times$  [10 (radial vapor region) + 4 (radial wick region) + 4 (radial wall region)], and an emissivity  $\epsilon = 0.645$  from experimental data. It took about 1.5 hours CPU time on a VAX 6420 to run the case.

The vapor temperatures for different time periods are compared with the experimental data for cases 19c-19d in Fig. 2.11 with evaporators 1 and 4 active. The agreement between the numerical solutions and the experimental data is also good.

The numerical interface vapor temperatures are compared with the corresponding experimental data for cases 21d-21e in Fig. 2.12. The numerical axial velocity and pressure profiles along the centerline of the heat pipe for the same cases are also given in Figs. 2.13-2.14. Figure

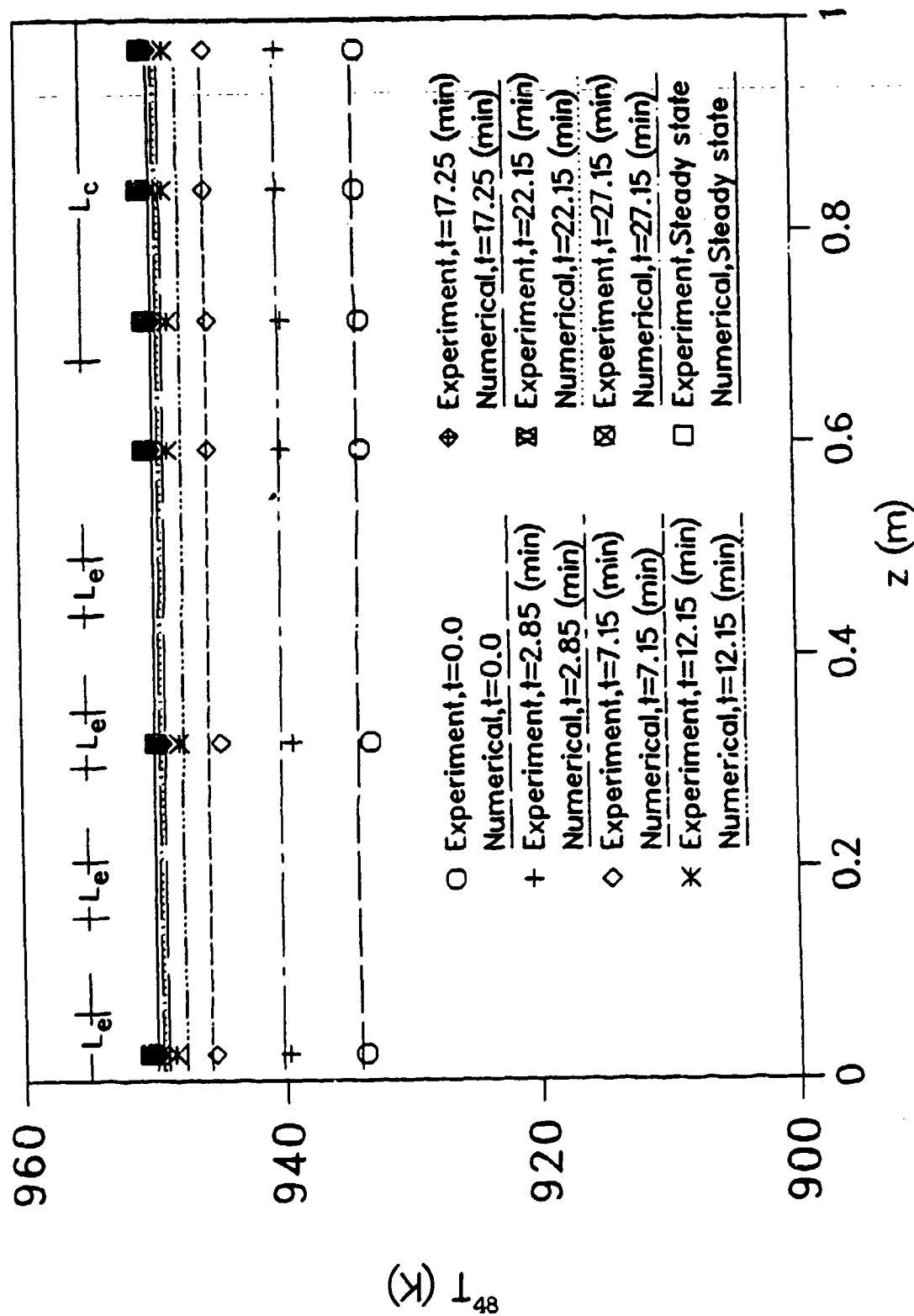


Figure 2.10 The Vapor Temperature for Different Time Periods Compared With the Experimental Data for Cases 6b-6c

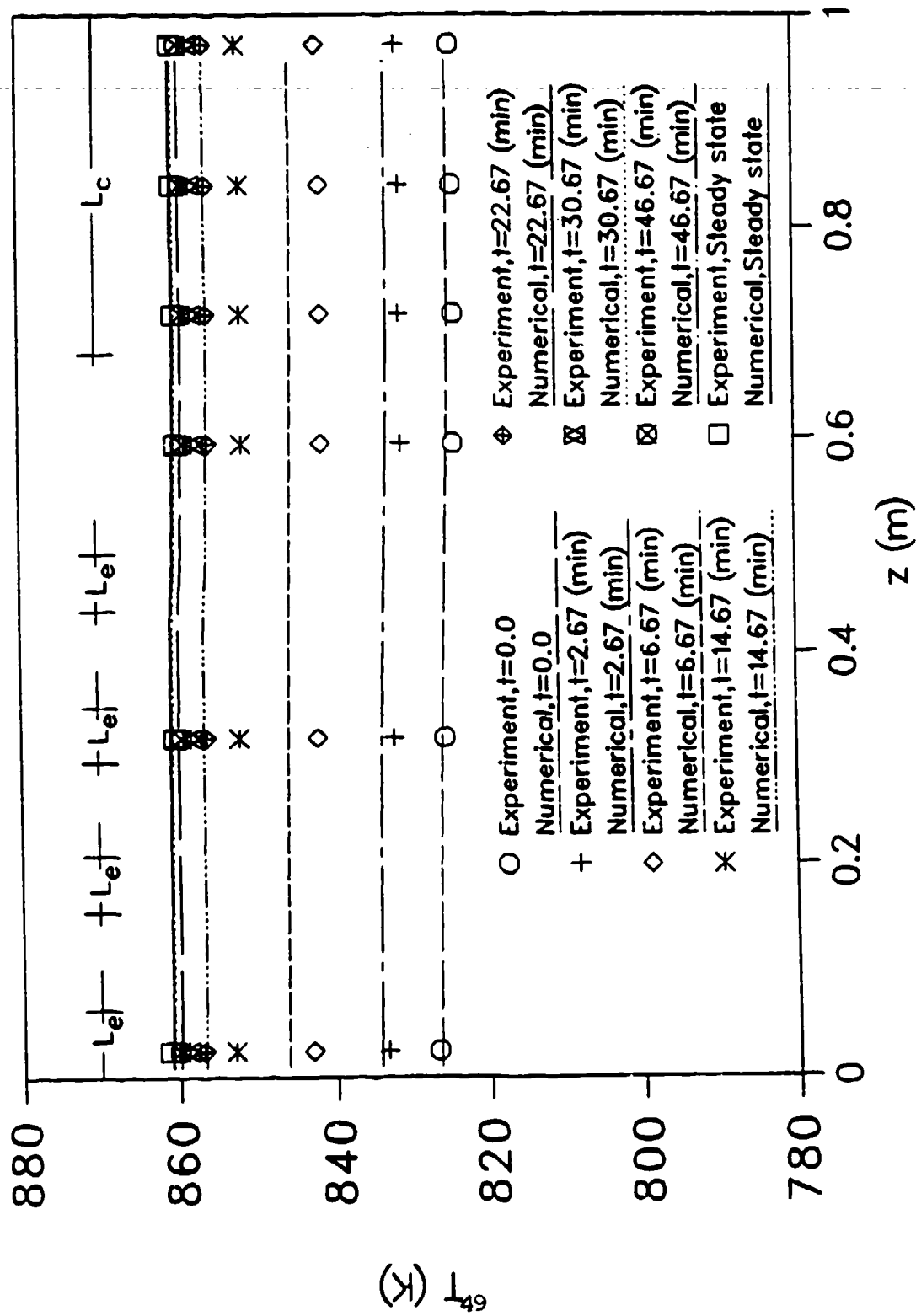


Figure 2.11 The Vapor Temperature for Different Time Periods Compared With the Experimental Data for Cases 19c-19d

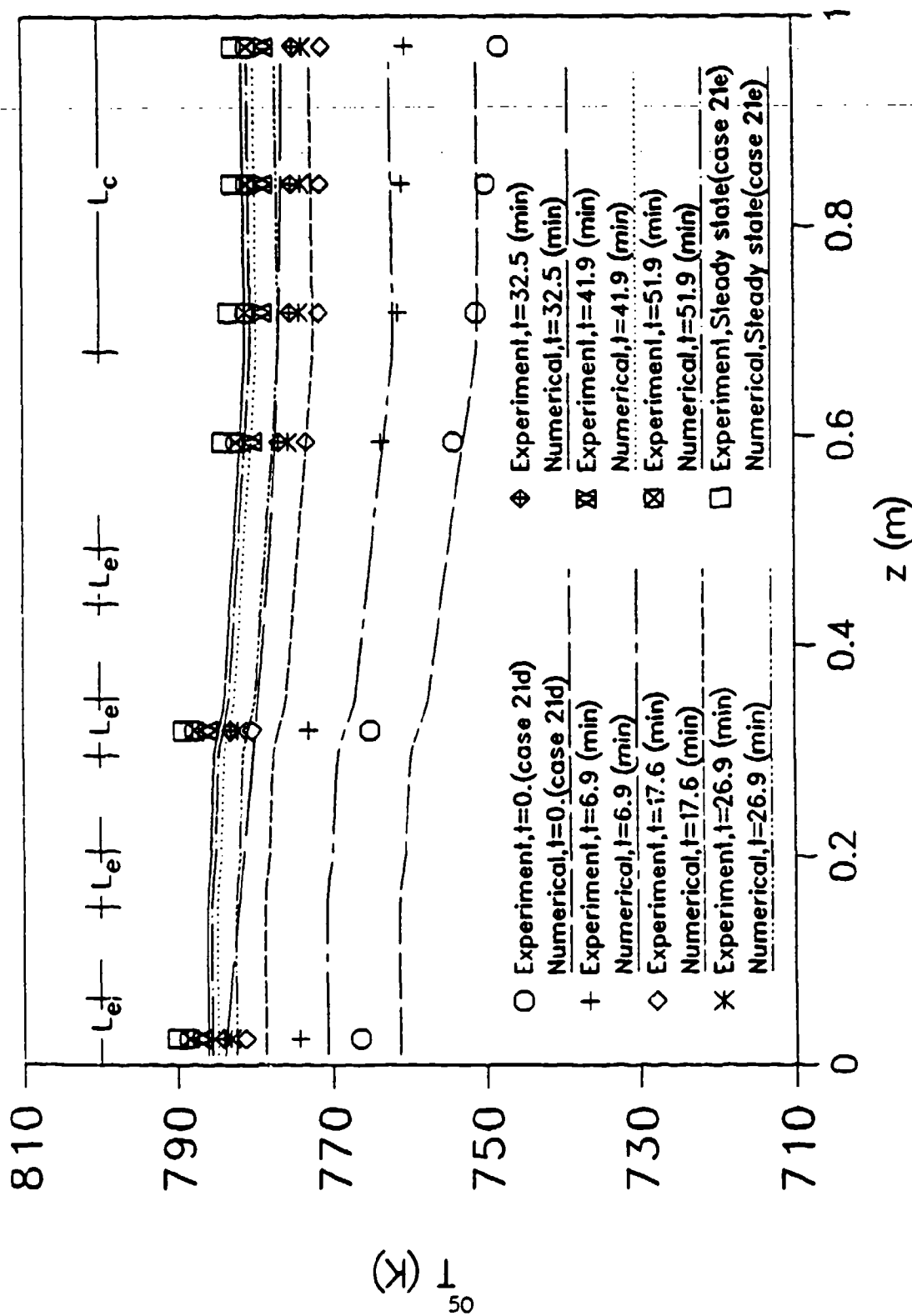


Figure 2.12 The Vapor Temperature for Different Time Periods Compared With the Experimental Data for Cases 21d-21e

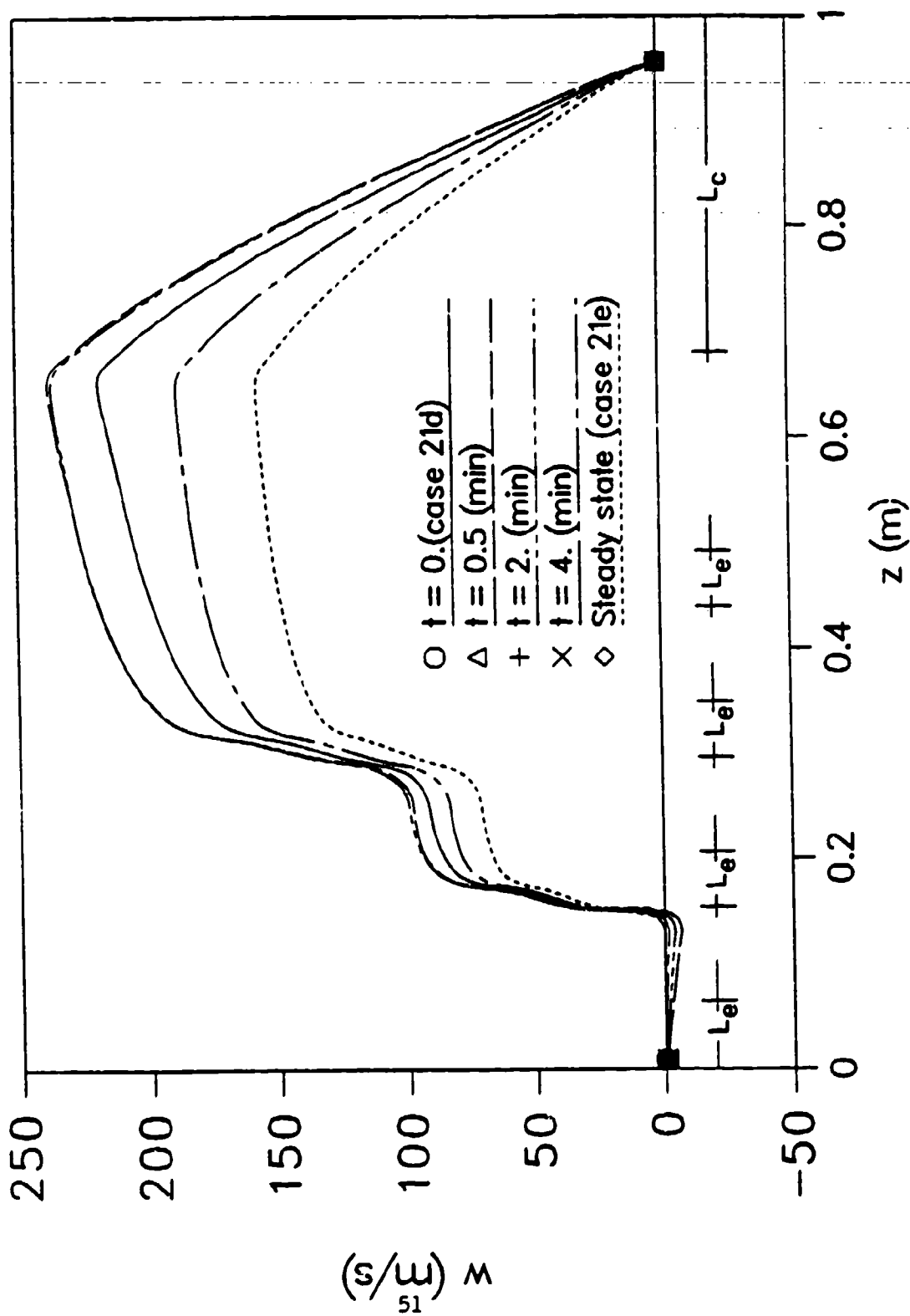


Figure 2.13 The Axial Velocity Profile Along the Centerline for Different Time Periods With Cases 21d-21e

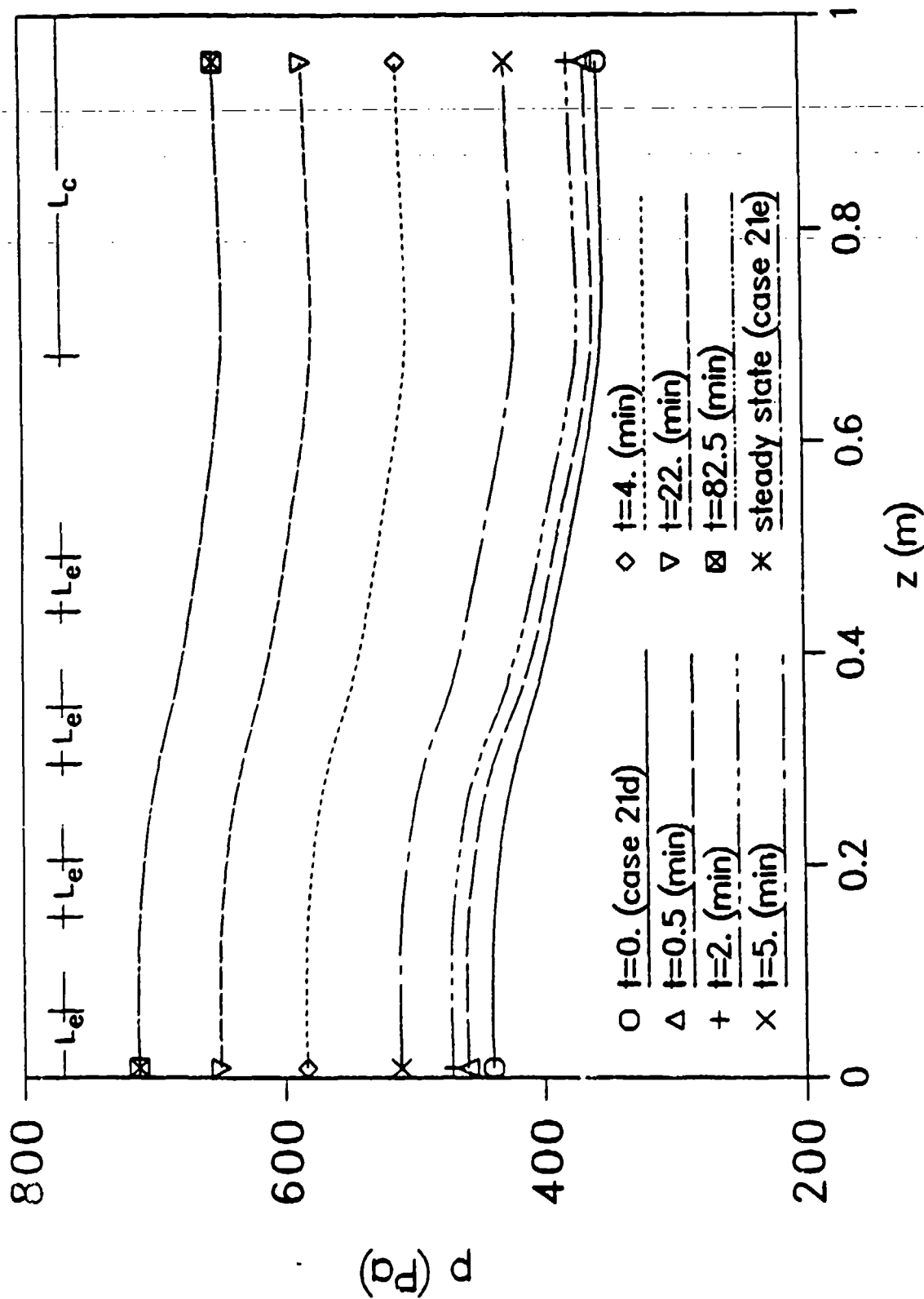


Figure 2.14 The Axial Pressure Profile Along the Centerline of the Heat Pipe for Different Time Periods With Cases 21d-21e

2.13 shows that since only evaporators 2 and 3 are active, the axial velocity curves are stepwise in the evaporator section. Also, the two-way vapor flow was observed near the left end of the evaporator section during the transient period. This was due to the sudden heat input increase to the active evaporators, which caused the temperature in the active part of the evaporator section to be higher than that in the inactive part. However, after the steady state was reached, the two-way vapor flow phenomenon disappeared because of the adiabatic boundary condition imposed on the inactive part of the evaporator section. Another trend worth notice was that shortly after the power input was increased from case 21d, the magnitude of the axial velocity increased slightly and then decreased gradually to another steady-state condition. This trend was also observed by Cao and Faghri (1990). Unlike the velocity curves, the vapor pressure increased monotonically from a lower level to a higher level as the power input at the evaporator section was increased. Also, near the left end of inactive part of the evaporator section, the pressure curves were relatively flat.

In the numerical modeling, the vapor flow was assumed to be laminar along the whole heat pipe. The numerical results above revealed that the axial vapor flow Reynolds number at the transport section in the heat pipe is in the range of 200-400, indicating that the laminar assumption is valid for the numerical simulation.

## 2.5 CONCLUSIONS

Steady-state tests showed that a change in the emissivity of the heat pipe wall can have a significant effect on the operating temperature of the

heat pipe. Raising the evaporator end of the heat pipe decreased the saturation pressure and temperature of the working fluid in the evaporator wick, and lowered the operating temperature of the heat pipe. The final steady-state operating temperature of the heat pipe is independent of the startup power levels and the size of subsequent power increases.

A capillary limit for four-evaporator steady-state operation was found while testing in air, at a evaporator elevation of  $5.7^{\circ}$ . A combination of the evaporator 1 wick dryout and copper contamination of the working fluid caused noncondensable gas to be formed within the heat pipe, and corrosion was found in the wick under evaporator 1.

Post-experiment examination of the heat pipe wick revealed that the loosely-wrapped circumferential screen wick contained significant annular gaps between the wick and the heat pipe wall, and between adjacent screen layers. The annular gaps enhanced the maximum heat transport capability of the heat pipe, but increased the difficulty in predicting the capillary limits and in calculating the optimal heat pipe fluid charge.

The numerical results agree favorably with the experimental vapor temperature, proving that the numerical model presented in this paper is capable of simulating heat pipe performance and would be very useful for heat pipe design.

### Section III

#### **EXPERIMENTAL ANALYSIS AND GENERALIZED ANALYTICAL PREDICTION OF CAPILLARY LIMITS OF CIRCUMFERENTIALLY-HEATED AND BLOCK-HEATED HEAT PIPES**

##### **3.1 SUMMARY**

An experimental analysis of several operating parameters for a low temperature, copper-water heat pipe under uniform circumferential heating and block heating has been performed. The transient wall and vapor temperature behavior under different step heat inputs was determined. The experimental and analytical capillary limit and the rise time to a 60°C vapor temperature was found for both modes of heating.

### 3.2 INTRODUCTION

Electronic circuitry has traditionally been cooled by forced or natural convection, but as VLSI techniques have improved, the amount of excess heat generated by electronic chips has increased dramatically. It has been proposed to employ heat pipes to remove this heat by directly attaching the heat pipe to the surface of the chip. This heating situation will be termed "block heating," as opposed to "circumferential heating," which is normally associated with cylindrical heat pipes.

Experimental data has been reported for circumferential heating in both low- and high-temperature heat pipe applications under steady-state and transient operation. The most recent efforts in this respect were those of Faghri and Thomas (1989) concerning annular heat pipes and Faghri and Buchko (1990) for heat pipes with multiple heat sources. The experimental heat pipe used by Rosenfeld (1987) consisted of a cylindrical pipe with a narrow block-heated evaporator called a line heater, and a circumferentially symmetric condenser section with a sintered-metal artery wick. The liquid-filled artery was on the side opposite the line heater. The experimental data taken from this heat pipe were strictly for steady-state operation, and no data were reported concerning the transient operating characteristics or capillary limit.

In the present study, the wall and centerline vapor temperatures and heat output were obtained for a circumferentially-heated and block-heated heat pipe. The objectives were: determine the elapsed time to reach a 60°C vapor temperature from an initial ambient temperature of 21°C after a step heat input, observe any differences in the steady-state wall and vapor

temperatures, and compare the experimental capillary limit of the heat pipe over a range of vapor temperatures to the generalized analytical capillary limits developed in this study for block-heated heat pipes.

### 3.3 EXPERIMENTAL SETUP AND TEST PROCEDURES

The schematic of the experimental heat pipe test stand is shown in Figure 3.1. The low-temperature heat pipe consisted of a copper pipe with sealed, copper end caps containing two wraps of copper screen of 1968.5 meshes per meter for the wick and degassed, distilled water as the working fluid. The heat pipe was 1000-mm long with a 25.4-mm outer diameter and a 1.7-mm wall thickness. Table 3.1 shows the physical dimensions and properties of the materials used in the experimental low temperature copper-water heat pipe.

Two Minco Thermofoil heaters, each with a maximum heat input of 250 W at 250°C, were used as evaporators. The circumferential heater covered the entire circumference of the pipe from 0.015 m to 0.079 m measured from the evaporator end cap, and the block heater covered the top half of the circumference from 0.089 m to 0.216 m as shown in Figure 3.2. The surface area of the circumferential heater was  $5.107 \times 10^{-3} \text{ m}^2$  and the block heater  $5.080 \times 10^{-3} \text{ m}^2$ . This resulted in the heat fluxes from the heaters being within 0.5% for a fixed total heat input. The heat input was determined by measuring the voltage and the amperage with a FLUKE-77 digital multimeter. The combined uncertainty of the power reading was  $\pm 3\%$ . The voltage was regulated using a variable AC transformer. The vapor temperature of 60°C was chosen as the reference temperature to keep the heaters from exceeding their safe operating temperatures.

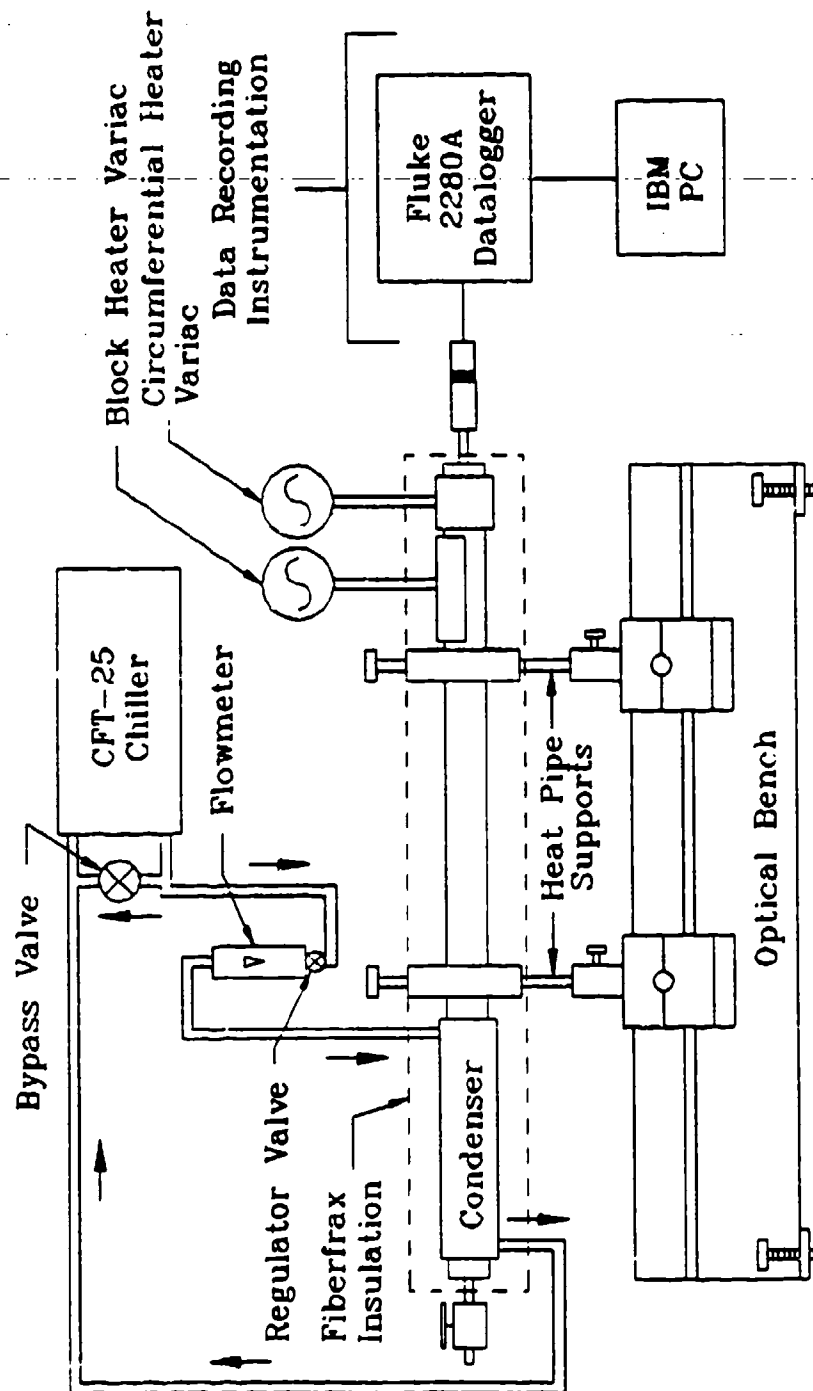


Figure 3.1 Schematic of Experimental Setup

**TABLE 3.1**

**Physical Dimensions and Material Properties of the  
Circumferentially-Heated and Block-Heated Heat Pipe**

Pipe and end cap material	Copper
Pipe O.D	$2.54 \times 10^{-2} \text{ m}$
Pipe I.D	$2.20 \times 10^{-2} \text{ m}$
Pipe length	1.0 m
End cap thickness	$3.175 \times 10^{-3} \text{ m}$
Wick material	Copper
Screen mesh number	$1.97 \times 10^3 \text{ m}^{-1}$
Wick thickness	$7.12 \times 10^{-4} \text{ m}$
Wick pore radius	$1.78 \times 10^{-4} \text{ m}$
Vapor core diameter	$2.058 \times 10^{-2} \text{ m}$
Working fluid	Distilled water
Fluid charge	40 cm <sup>3</sup>
Circumferential evaporator length	$6.4 \times 10^{-2} \text{ m}$
Block evaporator length	$1.27 \times 10^{-1} \text{ m}$
Circumferential mode transport length	$6.01 \times 10^{-1} \text{ m}$
Block mode transport length	$4.61 \times 10^{-1} \text{ m}$
Condenser length	$2.69 \times 10^{-1} \text{ m}$

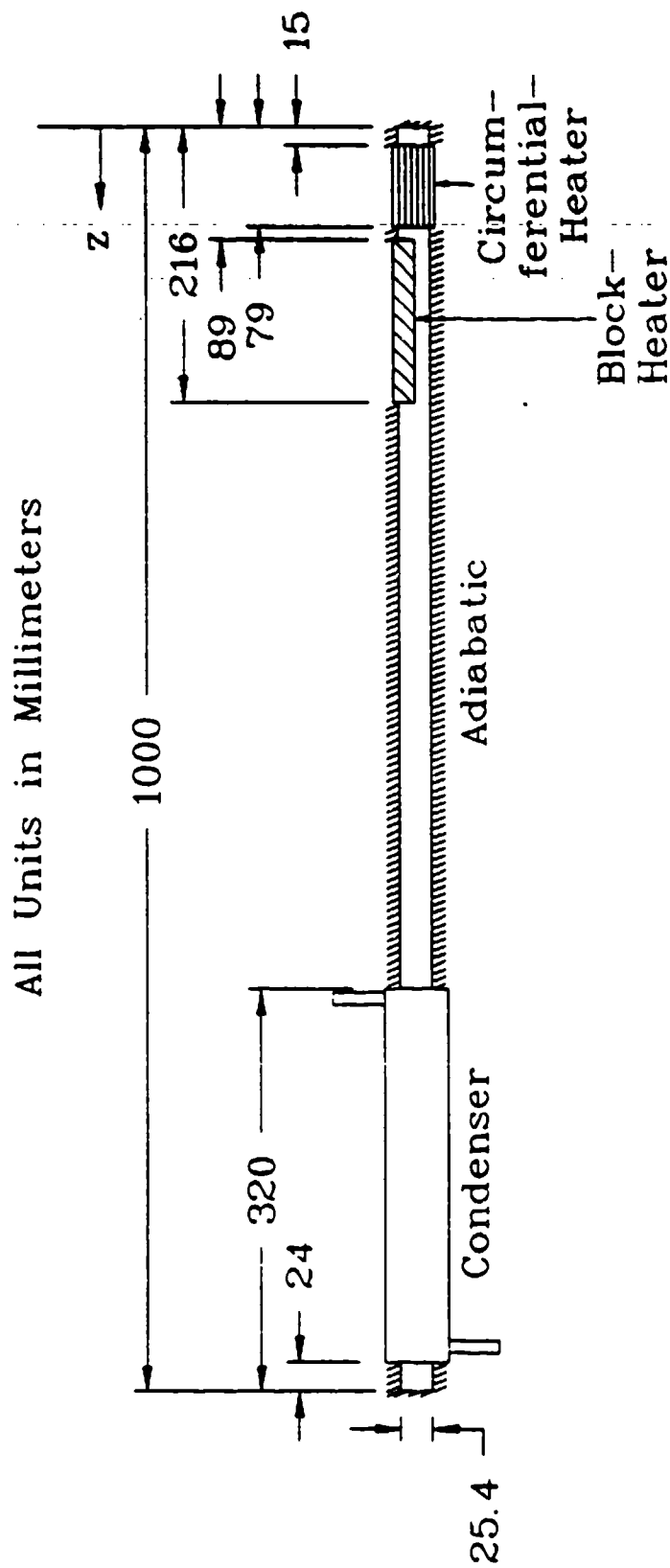


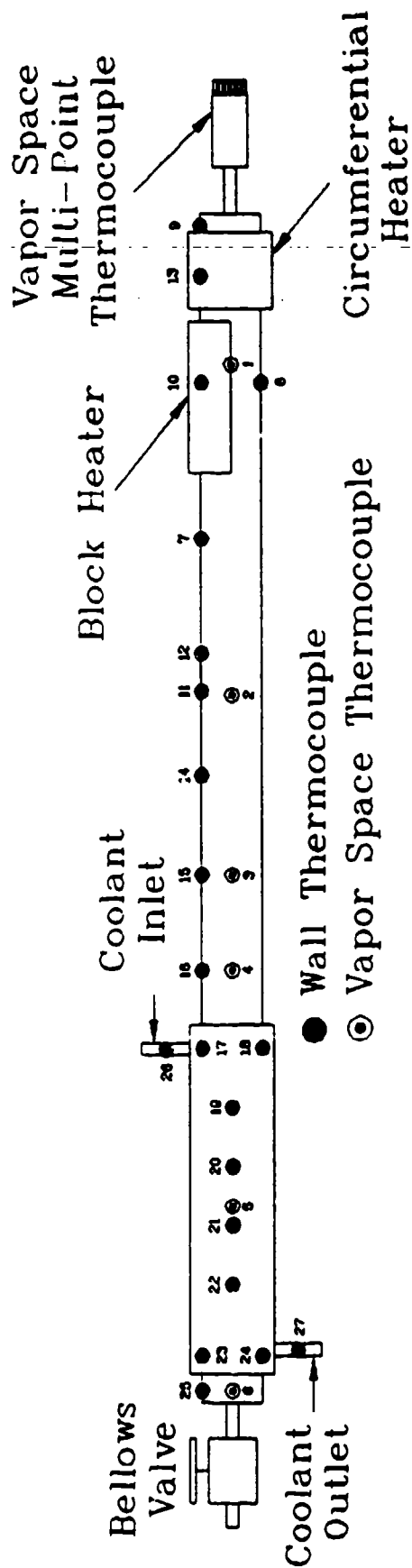
Figure 3.2 Experimental Heat Pipe Configuration

A Neslab CFT-25 chiller supplied water at a constant inlet temperature to the condenser. The chiller had a maximum capacity of 500 W over a coolant temperature range of 5°C to 30°C. A calibrated flowmeter was used to determine the volumetric flow rate of water through the condenser. The heat pipe was mounted on an optical bench to facilitate leveling. The condenser, coolant plumbing, and heat pipe were insulated with at least 2 inches of Fiberfrax ceramic fiber insulation.

The heat pipe was instrumented with 14 outer wall and 6 vapor centerline Type K and Type T thermocouples, which had uncertainties of  $\pm 0.5^\circ\text{C}$ . Two Type K thermocouples measured the inlet and outlet temperatures of the condenser coolant. Figure 3.3 shows the physical location of the thermocouples.

The elapsed time required for the copper-water heat pipe to reach a vapor temperature of 60°C after the application of a uniform step heat input of 25, 50, 75, 100, 125, and 150 W was determined for circumferentially-heated and block-heated operation. After the vapor temperature exceeded 65°C, the coolant flow was started through the condenser and the heat pipe was allowed to reach a steady-state condition. The inlet temperature of the coolant was held constant at  $27.5 \pm 2.5^\circ\text{C}$ , and the flow rate was adjusted to maintain vapor temperatures of 65-75°C. Higher heat inputs were not tested because the peak wall temperature under the heaters would have exceeded their design limitations. Wall and vapor temperatures and the heat output from the condenser were recorded. Between each test, a minimum of 8 hours was allowed for the heat pipe to cool to room temperature.

The capillary limit was defined as the heat input at which the wall



All distances measured from evaporator end cap

TC	Location (mm)	TC	Location (mm)	TC	Location (mm)
1	125	10	140	19	750
2	403	11	400	20	800
3	554	12	368	21	850
4	634	13	52	22	900
5	834	14	470	23	960
6	990	15	554	24	960
7	271	16	634	25	990
8	140	17	700	26	n/a
9	10	18	700	27	n/a

Figure 3.3 Heat Pipe Thermocouple Locations

temperature directly underneath the heater exhibited a continuous sudden temperature rise. This condition occurs when the amount of condensate being evaporated exceeds that being brought into the evaporator region by the capillary action of the wick, which dries out the wick and causes the evaporator wall temperature to increase.

For both heating modes, the capillary limit was determined by starting the heat pipe with a heat input of 50 W until the desired vapor temperature was reached. The coolant was then regulated through the condenser to keep the vapor temperature constant. For the tests performed at vapor temperatures below room temperature, the coolant was used to lower the vapor temperature to the test condition, and then the heater was turned on. After the coolant temperature had stabilized, the heat input was slowly increased in increments of approximately 50 W until the heat input was close to capillary limit. The heat input increments were then changed to 5 to 10 W until the capillary limit was reached. The heat pipe was allowed to reach steady-state conditions at each heat input by waiting a minimum of 20 minutes after the vapor temperatures had stabilized. The temperature directly underneath the heater was allowed to continuously rise for 25°C to verify that the wick had dried out. Two runs were performed for each vapor temperature under each heating mode to assure repeatability.

### 3.4 GENERALIZED ANALYTICAL PREDICTION OF CAPILLARY LIMIT FOR BLOCK HEATING

A simple, two-dimensional analysis was developed to predict the capillary limit based on the physical and material properties of the pipe, wick, and working fluid. The following assumptions were made: uniform heat addition in the heated region and heat removal in the condenser section, uniform vapor and

liquid temperatures, laminar liquid and vapor flow, steady-state operation, and axisymmetric liquid flow about the centerline in the wick of the adiabatic and condenser sections. This analysis does not assume an axisymmetric liquid flow about the centerline in the evaporator section. This development is an extension of the conventional method by Chi (1976) for circumferential heating to block heating. The pressure balance in a closed heat pipe is:

$$P_c(z) = [P_v(z) - P_v(z_{ref})] + [P_\ell(z_{ref}) - P_\ell(z)] \quad (3.1)$$

As the heat load increases, the capillary pressure given by equation (3.1) increases. This is caused by the increase in the pressure difference in both the liquid and vapor regions. For a given liquid-wick combination, the maximum capillary pressure generated is:

$$P_{cm} = \frac{2\sigma}{r_p} \quad (3.2)$$

The liquid pressure gradient is related to the frictional drag and the gravitational force (Chi, 1976):

$$[P_\ell(z) - P_\ell(z_{ref})] = \int_0^L -F_\ell Q^* \pm \rho L g \sin \psi \, dz \quad (3.3)$$

where  $z = 0$  refers to the condenser end cap and

$$F_\ell = \frac{\mu_\ell}{KA_w h_{fg} \rho_\ell}$$

$$K = \frac{d^2 \epsilon^3}{122(1 - \epsilon)^2}$$

$$\epsilon = 1 - \frac{\pi CD}{2(1 + C)}$$

$$A_w = \frac{\pi}{4} (d_i^2 - d_w^2)$$

Similarly, the vapor pressure drop can be expressed in terms of the local axial heat flow rate.

$$[P_v(z_{ref}) - P_v(z)] = \int_0^L \left[ F_v Q^* - D_v \frac{Q^*}{dz} \right] dz \quad (3.4)$$

where

$$F_v = \frac{(f_v Re_v) \mu_v}{2A_v r_{h,v}^2 \rho_v h_{fg}}$$

For cylindrical heat pipes,

$$(f_v Re_v) = 16$$

$$A_v = \frac{\pi}{4} d_v^2$$

$$r_{h,v} = \frac{d_w}{2}$$

For closed heat pipe systems (Chi, 1976),

$$\int_0^L -D_v \frac{dQ^*}{dz} dz = 0$$

so equation (3.4) simplifies to:

$$[P_v(z_{ref}) - P_v(z)] = \int_0^L F_v Q^* dz \quad (3.5)$$

In the block-heated heat pipe, the circumferential distribution of the local axial heat rate is not uniform in the evaporator section; therefore, the local axial heat rate is defined as:

$$Q^*(z) = \int_0^{2\pi} Q'(z, \theta) R_{ave} d\theta \quad (3.6)$$

where  $Q'(z, \theta)$  is the axial heat rate per unit circumferential length and  $R_{ave}$  is the average radius of the liquid-wick.

The maximum possible capillary pressure is reduced by the effects of the gravitational field on the circumferential movement of liquid in the wick (Chi, 1976).

$$P_{pm} = P_{cm} - P_n \quad (3.7)$$

where,

$$P_n = \rho L g d_i \cos \psi \quad (3.8)$$

Substituting equations (3.2), (3.3), (3.5), (3.7), and (3.8) into equation (3.1) and assuming a zero inclination angle yields:

$$\frac{2\sigma}{r_p} - \rho L g d_i = \int_0^L (F_v Q^* + F_\ell Q^*) dz$$

Collecting the constants and substituting equation (3.6) gives:

$$\frac{\frac{2\sigma}{r_p} - \rho L g d_i}{F_v + F_\ell} = \int_0^L Q^* dz = \int_0^L \int_0^{2\pi} Q'(z, \theta) R_{ave} d\theta dz \quad (3.9)$$

The capillary limit is determined by integrating equation (3.9) and then solving the resulting equation for the capillary limit. In the uniform, circumferentially-heated heat pipe, the integral with respect to  $d\theta$  simplifies to a constant times  $Q^*(z)$  since  $Q'(z, \theta)$  is uniform in the circumferential direction.

$$Q^*(z) = Q'(z, \theta) 2\pi R_{ave} \quad (3.10)$$

For circumferentially-heated heat pipes equation (3.6) becomes:

$$\frac{\frac{2\sigma}{r_p} - \rho L g d_i}{F_v + F_\ell} = \int_0^L Q^*(z) dz \quad (3.11)$$

For the block-heated heat pipe, the capillary heat transport factor is two-dimensional in the evaporator, so  $Q'(z, \theta)$  is defined for each section of the heat pipe. For the condenser and adiabatic sections, a uniform axial heat

rate is assumed.

For  $0 \leq z \leq L_c$ :

$$Q'(z, \theta) = \frac{Q_{c, \max} z}{2\pi R_{\text{ave}} L_c} \quad (3.12)$$

For  $L_c \leq z \leq L_c + L_a$ :

$$Q'(z, \theta) = \frac{Q_{c, \max}}{2\pi R_{\text{ave}}} \quad (3.13)$$

Two separate equations are needed for the axial heat rate per unit circumferential distance for the heated region and the insulated region in the evaporator section. The uniform radial heat flux in the heated region creates a linear relationship in the axial heat rate from the uniform value at the adiabatic/evaporator section boundary to zero at the evaporator end cap. The heat rate per unit circumferential length in the heated region of the evaporator section is described by the following equation.

For  $L_c + L_a \leq z \leq L$  and  $0 \leq \theta \leq \pi$ :

$$Q'(z, \theta) = \left[ \frac{L - z}{L_e} \right] \left[ \frac{1}{\pi R_{\text{ave}}} \right] \left[ \frac{Q_{c, \max}}{2} \right] \quad (3.14)$$

Since there is no heat transfer through the walls of the insulated region of the evaporator section, the liquid must be transported from the insulated

region to the heated region before it can be evaporated. An average transport length was developed from the maximum and minimum transport lengths. The minimum transport length is along the interface between the heated and insulated regions of the liquid-wick and is equal to the evaporator length. The maximum transport length in the evaporator occurs for flow entering the evaporator section directly opposite of the center of the heater. The maximum travel length for this flow is the evaporator length plus one half the circumference. The average of these two values is:

$$\frac{(L) + (L + \pi R_{ave})}{2} = L + \frac{\pi}{2} R_{ave} \quad (3.15)$$

Equation (3.15) was then used to determine a linear equation for  $Q'(z, \theta)$  in the insulated region of the evaporator.

For  $L_c + L_a \leq z \leq L_{eff}$  and  $\pi \leq \theta \leq 2\pi$ :

$$Q'(z, \theta) = \left[ \frac{L_{eff} - z}{L_e + \frac{\pi}{2} R_{ave}} \right] \left[ \frac{1}{\pi R_{ave}} \right] \left[ \frac{Q_{c, max}}{2} \right] \quad (3.16)$$

where  $L_{eff}$  is the effective travel length and is equal to  $L + \frac{\pi}{2} R_{ave}$  in this case.  $Q'(z, \theta)$  is then substituted into equation (3.9) and a solution found in terms of  $Q_{c, max}$ .

$$\frac{\frac{2\sigma}{r} - \rho L g d_i}{F_v + F_l} = \int_0^{2\pi} \int_0^{L_c} \left[ \frac{Q_{c,max}}{2\pi L} \right] \left[ \frac{z}{L_c} \right] dz R_{ave} d\theta + \int_0^{2\pi} \int_{L_c}^{L_c+L_a} \left[ \frac{Q_{c,max}}{2\pi R_{ave}} \right] dz R_{ave} d\theta$$

$$+ \int_0^{2\pi} \int_{L-L_e}^L \left[ \frac{L-z}{L_e} \right] \left[ \frac{1}{\pi R_{ave}} \right] \left[ \frac{Q_{c,max}}{2} \right] dz R_{ave} d\theta$$

$$+ \int_0^{2\pi} \int_{L-L_e}^{L_{eff}} \left[ \frac{L + \frac{\pi}{2} R_{ave} - z}{L_e + \frac{\pi}{2} R_{ave}} \right] \left[ \frac{1}{\pi R_{ave}} \right] \left[ \frac{Q_{c,max}}{2} \right] dz R_{ave} d\theta$$

$$Q_{c,max} = \frac{\frac{\frac{2\sigma}{r} - \pi L g d_i}{F_v + F_l}}{\left[ \frac{L_c}{2} + L_a + \frac{L_e}{2} + \frac{\pi}{8} R_{ave} \right]} \quad (3.17)$$

The term  $\frac{\pi}{8} R_{ave}$  cancels out during the integration for circumferential heating and the resulting equation is identical to that given by Chi (1976).

### 3.5 RESULTS AND DISCUSSION

The time needed for the heat pipe vapor temperature to reach 60°C was recorded under circumferential heating and block heating. A comparison of the elapsed time between the two modes of heating is discussed. The vapor and wall temperatures during the transient startup and the steady-state conditions are presented. The experimental and analytical capillary limits using both modes of heating were determined for several vapor temperatures. A comparison between the two modes of heating and between the analytical and experimental results is made.

### 3.5.1 Elapsed Time to 60°C Vapor Temperature

Figure 3.4 presents the time required for the heat pipe vapor temperature to reach 60°C was measured to compare the transient response of the heat pipe in circumferential and block heating modes. There was no significant difference in the response time between the two operating modes. The differences that were seen can be attributed to the variations in the starting vapor temperature and the resolution of the transient data. The data were taken at 50-second intervals and so the resolution of the transient data was limited to  $\pm 50$  seconds. This was the minimum time required by the data recording instrumentation for the calculation, display, and recording of the temperatures. The starting temperature of the heat pipe varied from 21°C to 24°C. By an energy balance, as heat was put into the heat pipe and no heat removed by the condenser, the internal energy of the heat pipe increased. As the heat input was increased, the rate at which the internal energy rose also increased and therefore the vapor temperature rose more quickly. We concluded that the heat pipe time response to a step heat input was the same for both heating modes.

### 3.5.2 Transient and Steady-State Temperature Comparisons

The transient vapor and wall temperatures for step heat inputs of 50 W and 150 W are shown in Figures 3.5 and 3.6 for circumferential heating, and in Figures 3.7 and 3.8 for block heating, respectively. The wall temperatures shown in these figures are from the top of the heat pipe. The transient vapor centerline temperature profiles for both circumferential (Figures 3.5a and 3.6a) and block heating (Figures 3.7a and 3.8a) modes show very little axial variance in the vapor temperature of the heat pipe at these heat inputs. This flat axial profile is common in low-temperature heat pipes in which no

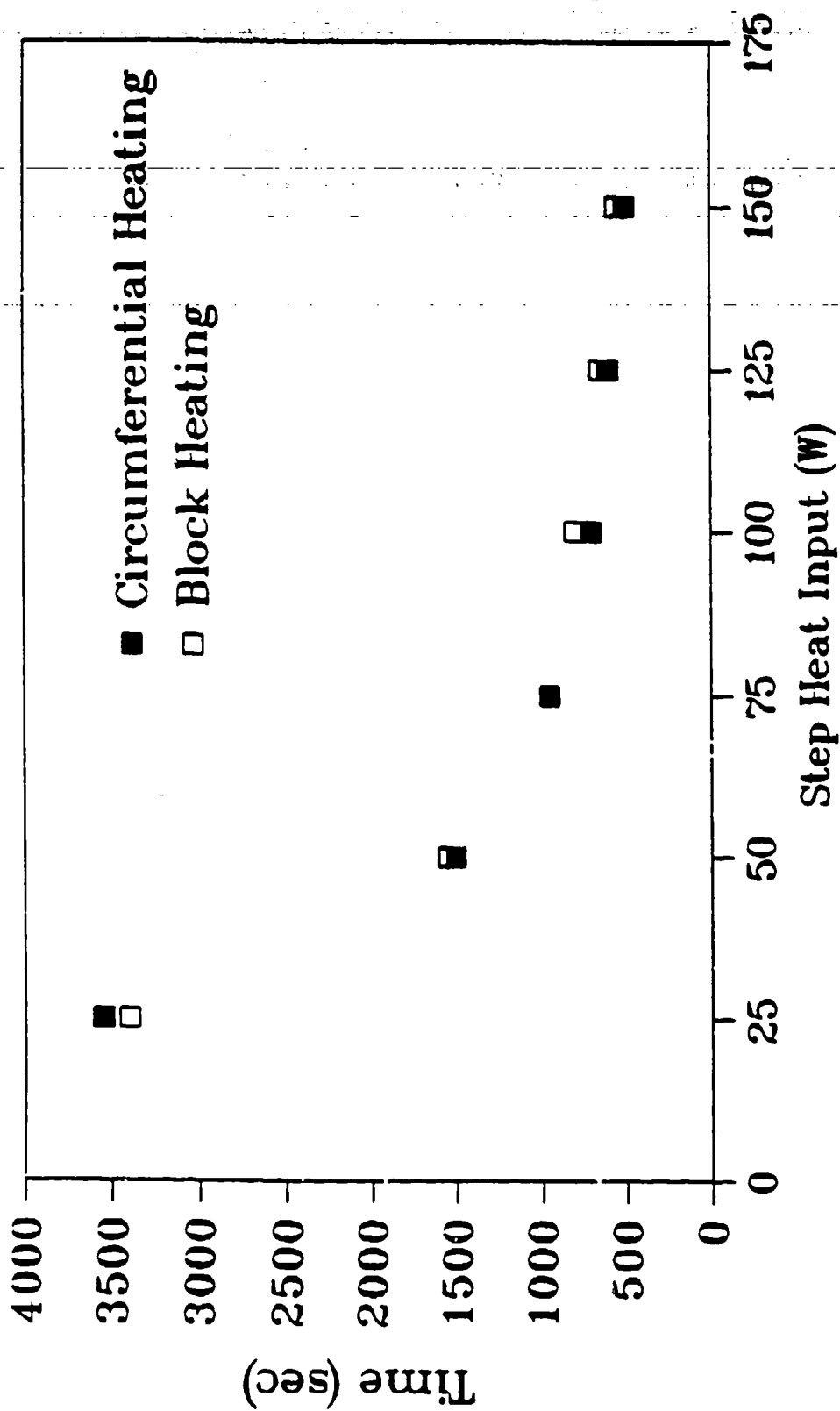
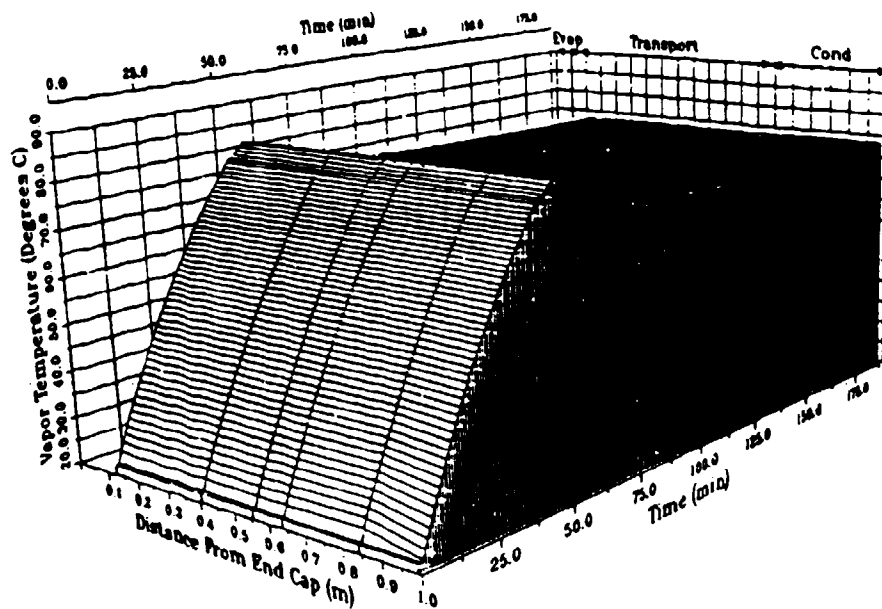
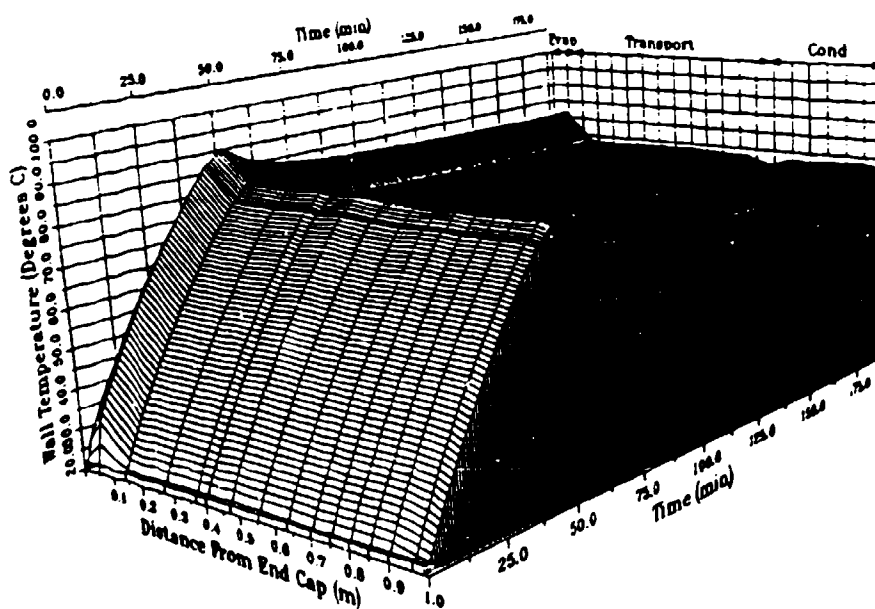


Figure 3.4 Time for Heat Pipe Vapor Temperature to Reach 60°C Versus Step Heat Input

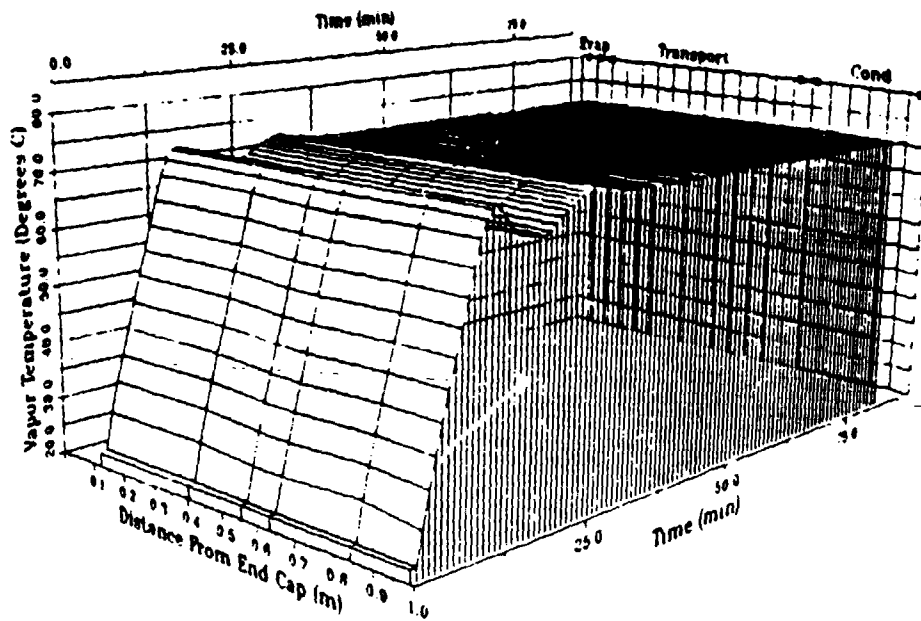


5a Vapor Temperatures

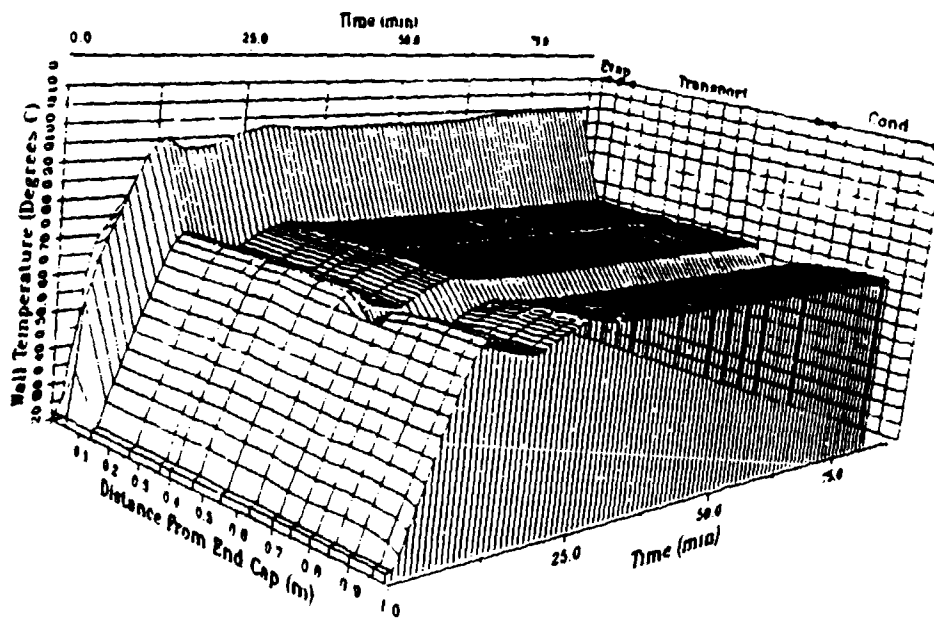


5b Wall Temperatures

Figure 3.5 Transient Starting Temperature Profiles of the Circumferentially-Heated Heat Pipe for 50 W

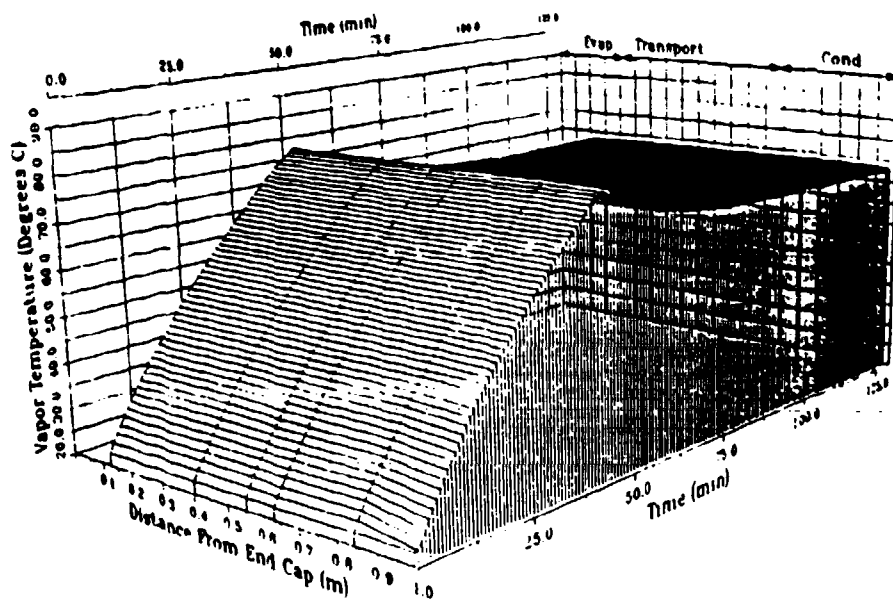


6a Vapor Temperatures

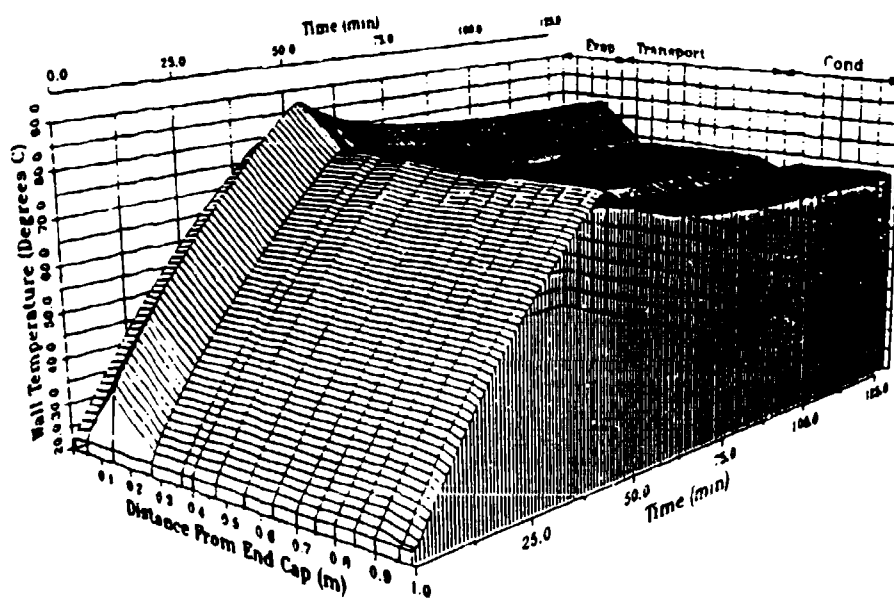


6b Wall Temperatures

Figure 3.6 Transient Starting Temperature Profiles of the Circumferentially-Heated Heat Pipe for 150 W

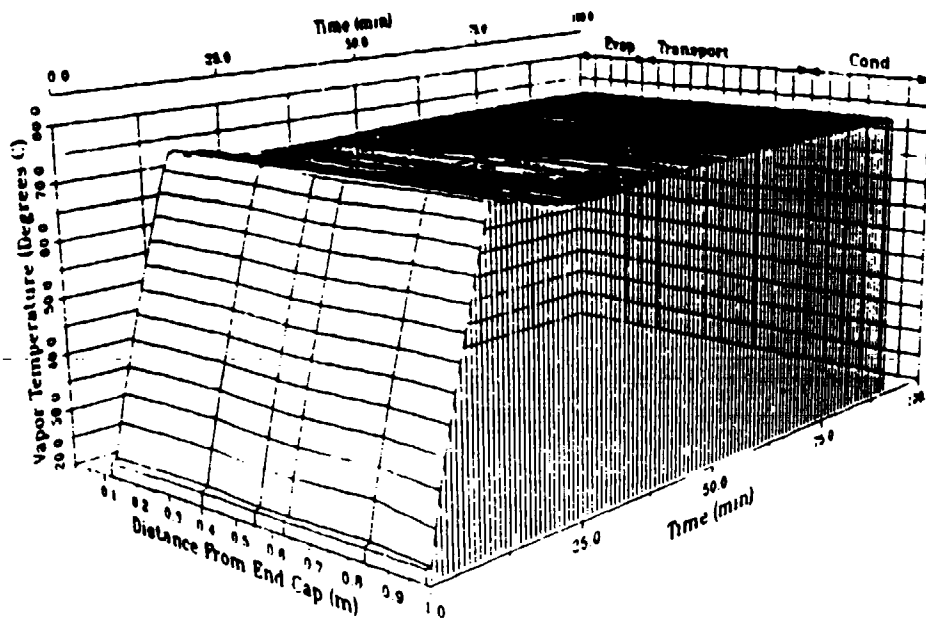


7a Vapor Temperatures

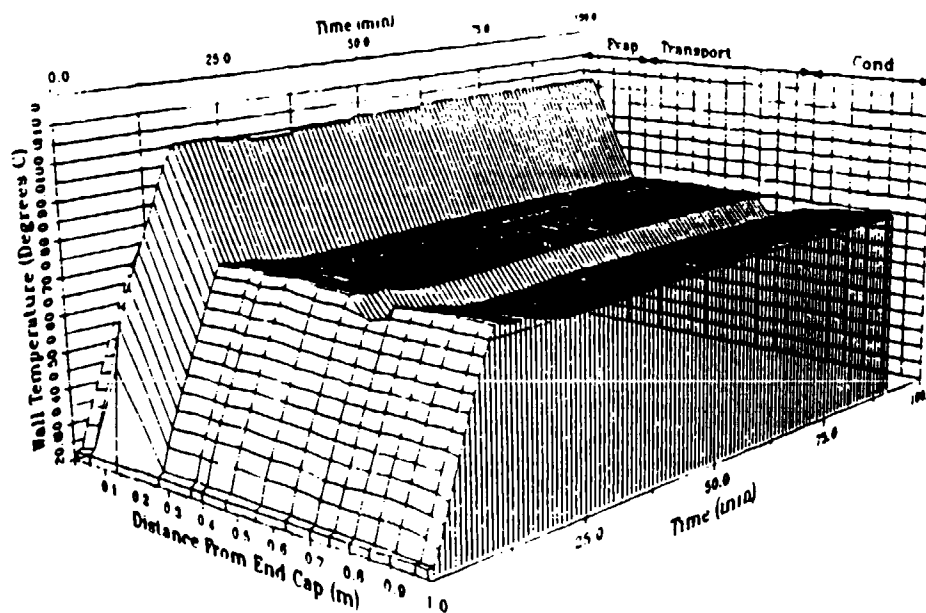


7b Wall Temperatures

Figure 3.7 Transient Starting Temperature Profiles of the Block-Heated Heat Pipe for 50 W



8a Vapor Temperatures



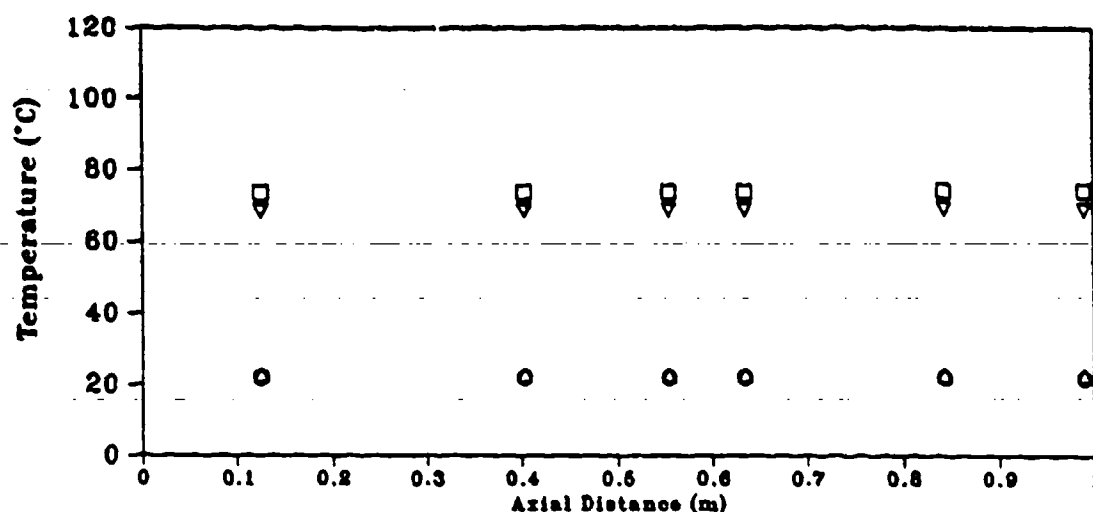
8b Wall Temperatures

Figure 3.8 Transient Starting Temperature Profiles of the Block-Heated Heat Pipe for 150 W

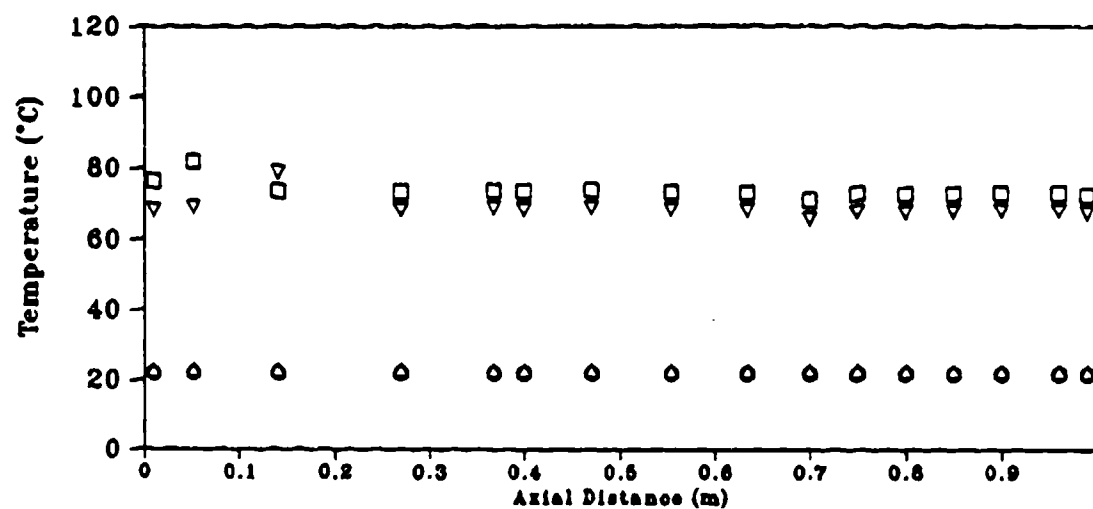
noncondensable gases are present in the heat pipe (Chi, 1976; Faghri and Buchko, 1990).

The transient wall temperature profiles for both circumferential (Figures 3.5b and 3.6b) and block heating (Figures 3.7b and 3.8b) modes show that the temperature spike directly underneath the heater develops almost immediately upon the application of heat. Also, the remainder of the wall temperatures remain axially uniform throughout the transient period. Except for the fact that the peak temperature in the block heating mode was higher than the circumferential heating mode for a given heat input, no significant differences were observed in the transient response of the heat pipe.

After the coolant had been started through the condenser, the heat pipe was allowed to reach a steady-state condition. Figures 3.9 and 3.10 show a comparison of the initial and final wall and vapor temperatures for both heating modes for heat inputs of 50 and 150 W. No effort was made to match the final vapor temperatures between the circumferential and block heating modes. Instead, a constant coolant flow rate and constant inlet temperature was maintained for each heat input. This was the cause for the slight difference in the steady-state vapor and wall temperatures in the 50 W heat input test. When this difference was taken into account, we determined that the steady-state vapor and wall temperatures for both heating modes were similar, except for the wall temperatures in the region around the evaporator. Since the two evaporators were not in the same physical location, the difference in the location of the wall temperature peaks was expected. The peak wall temperature for the block-heated mode was higher than the circumferentially-heated mode for all heat inputs studied.



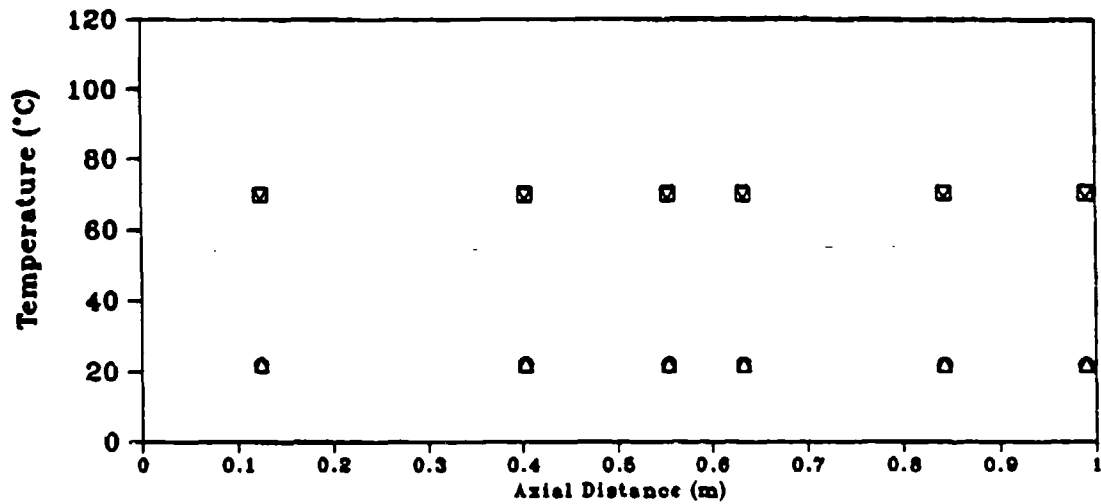
(a) Vapor Temperatures



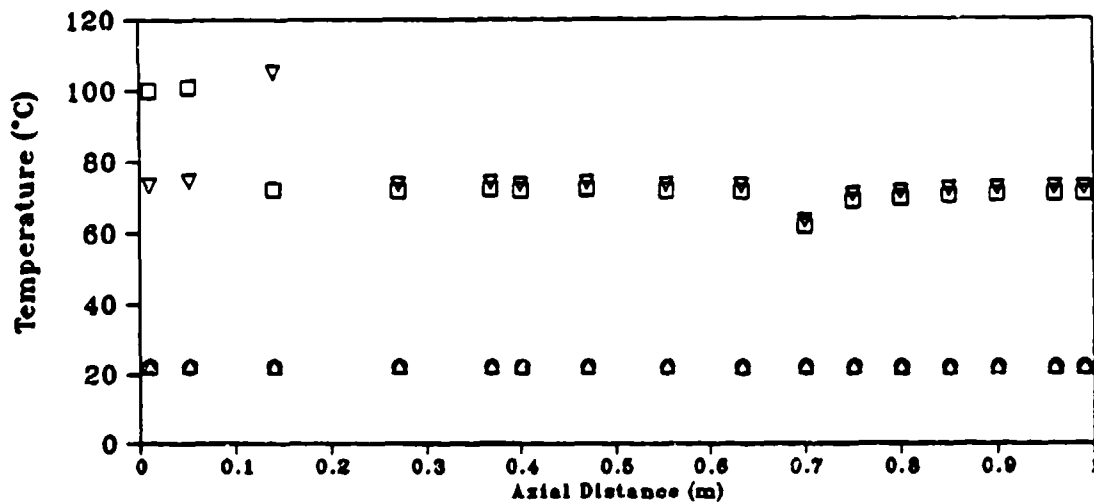
(b) Wall Temperatures

- Initial Temperatures Circumferential Heating
- Steady-State Temperatures Circumferential Heating
- △ Initial Temperatures Block Heating
- ▽ Steady-State Temperatures Block Heating

Figure 3.9 Vapor and Wall Temperature Versus Axial Distance From Evaporator End Cap for 50 Watt Step Heat Input



(a) Vapor Temperatures



(b) Wall Temperatures

- Initial Temperatures Circumferential Heating
- Steady-State Temperatures Circumferential Heating
- △ Initial Temperatures Block Heating
- ▽ Steady-State Temperatures Block Heating

Figure 3.10 Vapor and Wall Temperature Versus Axial Distance From Evaporator End Cap for 150 Watt Step Heat Input

At the higher heat inputs, a temperature trough developed at the beginning of the condenser section when the coolant was allowed to flow through the condenser. This was caused by the large temperature difference between the coolant inlet temperature and the wall temperature at the beginning of the condenser.

### 3.5.3 Capillary Limit

The experimentally determined capillary limits for both modes of heating were compared to the analytical predictions with an excellent agreement. The physical dimensions of the heat pipe and the material properties of water were substituted into equation (3.17) and the analytical capillary limit was determined for several vapor temperatures as shown in Figure 3.11. The experimental capillary limits are also shown in this figure.

The analytical methods used to determine the capillary limits were in agreement with the experimental data for both heating modes. For the block-heated experiment, the experimental capillary limit at 20°C vapor temperature was unobtainable because of insufficient coolant flow capacity in the condenser. The experimental capillary limits for the block heating mode at 80°C and 100°C could not be determined because the limit was above the maximum heat input of the heater. For the experimental capillary limits reported, there was good agreement with the analytical calculations. The analytical prediction provides a conservative estimation of the capillary limit of the heat pipe under block heating. There was a maximum error of 10% between the experimental limits and the analytical limits for the circumferentially-heated heat pipe, and a maximum of 25% for the block-heated heat pipe.

The experimental capillary limits for block heating are higher than those for circumferential heating. This was partially caused by the shorter adiabatic section in the block-heated heat pipe. Faghri and Buchko (1990) showed that decreasing the adiabatic transport length significantly increased the capillary limit. The analytical capillary limits calculated for this study also show this trend. In both the analytical and experimental predictions we observed a significant increase in the capillary limit for both modes of heating as the vapor temperature increased. This was due to the decrease of the viscosity of liquid water.

### 3.6 CONCLUSIONS

A copper-water heat pipe with both circumferential and block heaters was used to determine several transient and steady operating characteristics under each heating mode. There were only very small differences in the elapsed time for the heat pipe to reach 60°C between the circumferential heating and block heating modes, with the largest differences at the low heat inputs. The vapor temperatures remained within 1°C of each other during the entire transient startup. The fast time response of the heat pipe to block heating makes it as effective in electronic cooling as other conventional applications. The peak wall temperature during transient startup for the block-heated heat pipe was slightly higher than the circumferentially-heated heat pipe. The vapor and wall temperatures at steady-state were not significantly different either, except the wall temperatures in the region around the evaporator.

The experimental capillary limits determined for a copper-water heat pipe in circumferential and block heating modes were compared to the analytical

values calculated using equation (3.17). The analytical predictions were within 25% of the experimental limits. The capillary limits for block-heated operation were slightly higher than the circumferentially-heated limits. This can be partially attributed to the shorter adiabatic transport section of the block-heated heat pipe. The capillary limit increased significantly with an increase in vapor temperature for both heating modes.

## Section IV

### THREE-DIMENSIONAL NUMERICAL MODELING OF CIRCUMFERENTIALLY-HEATED AND BLOCK-HEATED HEAT PIPES

#### 4.1 SUMMARY

A general three-dimensional numerical heat pipe model which includes the pipe wall, wick, and vapor flow as a conjugate heat-transfer problem has been developed. The model was employed to solve for the operating characteristics of a circumferentially-heated and block-heated heat pipe. These numerical results were compared to experimental data from the heat pipe described in Section III. A good agreement between the experimental data and the numerical results was obtained for both heating modes.

## 4.2 INTRODUCTION

The three-dimensional numerical solution of block-heated heat pipes as a conjugate problem has not been performed in the past because of the complexity of the problem and the lack of sufficient computer capacity. Circumferentially-heated cylindrical heat pipes have been modeled numerically in two dimensions using cylindrical coordinates for steady-state (Chen and Faghri, 1990) and transient (Cao and Faghri, 1990) conditions. The evaporator region of a block-heated cylindrical heat pipe has been modeled numerically by assuming that the pipe diameter is significantly larger than the wall thickness and the heated region is much longer than its width (Rosenfeld, 1987; Cao et al., 1989). These assumptions allowed the circumference of the evaporator to be modeled in Cartesian coordinates.

Rosenfeld (1987) developed a numerical method to determine the steady-state wall temperature profile in the azimuthal direction for a block-heated heat pipe using a power-law assumption to represent the boiling of the working fluid. The geometry of the model was a cylindrical pipe with evaporator and condenser sections and no adiabatic transport section. A narrow block heater was placed along the axial direction. We assumed that the evaporator length was much longer than its width and the temperature difference across the wall in the radial direction was negligible because the wall was thin and had a high thermal conductivity. We also assumed that the vapor temperature was uniform and constant. The exponent of the power law used to model the boiling of the working fluid can vary from 0.5 to 6.0 for different wall materials and thicknesses, although values between 1.0 and 2.0 are most common. A model of the evaporator region was developed using a one-dimensional Cartesian coordinate system to represent the azimuthal

direction. Two different sets of boundary conditions were applied. The first case applied to heat pipes with large diameters, thin walls, and low wall thermal conductivities, and was solved analytically by simple integration. The second case pertained to thick walls and high thermal conductivities, resulting in a boundary-value problem which was solved using the shooting method.

Cao et al. (1989) numerically analyzed the outside wall temperature profile in the evaporator section of high- and low-temperature cylindrical heat pipes with localized heating under steady-state conditions. The evaporator for the high-temperature heat pipe was a point source (spot-heated) with the remainder of the heat pipe operating as the condenser. The low-temperature heat pipe consisted of a block-heated evaporator that covered a larger portion of the circumference than the spot heater, a short adiabatic transport region and a circumferential condenser. The vapor temperature was assumed constant throughout the entire vapor space. The diameter of the heat pipe was assumed to be much larger than the wall thickness, thus allowing a two-dimensional Cartesian coordinate system to represent the axial and azimuthal directions. The finite-difference method based on the control-volume formulation was used to solve the two-dimensional energy conservation equation. We determined that for high-temperature spot-heated heat pipes, the thermal conductivity of the wall played an important role in limiting the peak wall temperature directly underneath the heater.

Chen and Faghri (1990) numerically analyzed the steady-state operating characteristics of circumferentially-heated cylindrical heat pipes with single

or multiple heat sources using a two-dimensional conjugate heat transfer model. The use of a conjugate model allowed the vapor temperature to be solved for directly instead of being assumed constant. It also eliminated the need for a power-law assumption to model the boiling of the working fluid at the liquid-wick/vapor interface as was done in previous studies (Rosenfeld, 1987; Cao et al., 1989). Both the elliptic and partially-parabolic forms of the conservation equations were examined. The mass, momentum, and energy equations were solved for the velocity, pressure, and temperature fields for the entire heat pipe domain: vapor, liquid-wick, and pipe wall regions in the evaporator, adiabatic transport, and condenser sections. The heat transfer in the liquid-wick region was modeled as pure conduction. Conjugate axial conduction, vapor compressibility, flow reversal, and viscous dissipation effects were discussed.

The objective of this study was to develop a three-dimensional numerical model for determining the temperature, pressure and velocity distributions in the entire domain of a circumferentially-heated and a block-heated heat pipe as a conjugate problem without assuming a uniform vapor temperature (Rosenfeld, 1987; Cao et al., 1989). The problem was solved such that it was not necessary to model the boiling at the liquid-wick/vapor interface with a power-law assumption. This model was an extension of that developed by Chen and Faghri (1990) from two dimensions to three dimensions with the addition of block heating in the evaporator.

#### 4.3 MATHEMATICAL MODELING

Schematics of the computational domains used for the block-heated and circumferentially-heated heat pipes are shown in Figures 4.1 and 4.2,

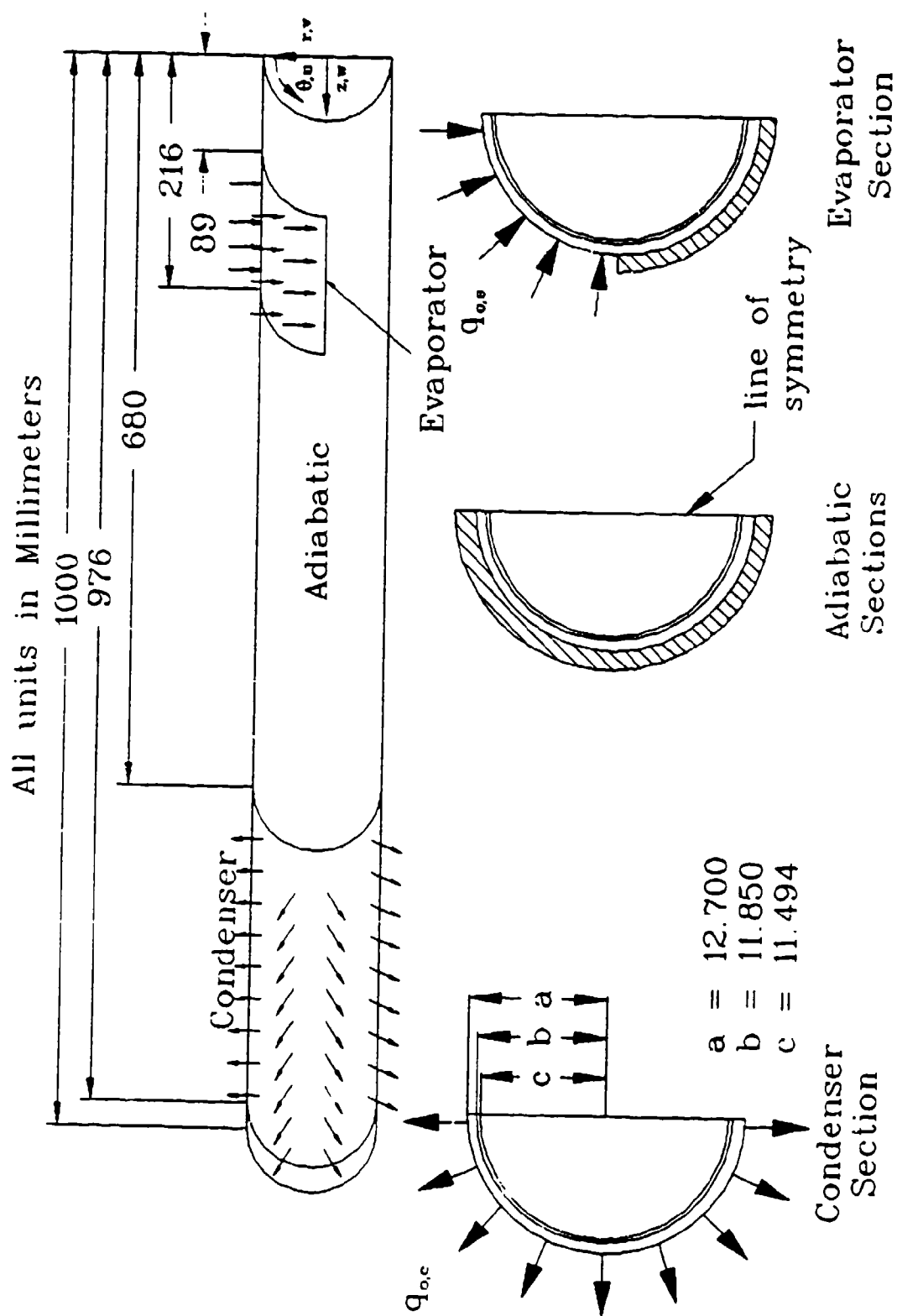


Figure 4.1 Block-Heated Heat Pipe Model

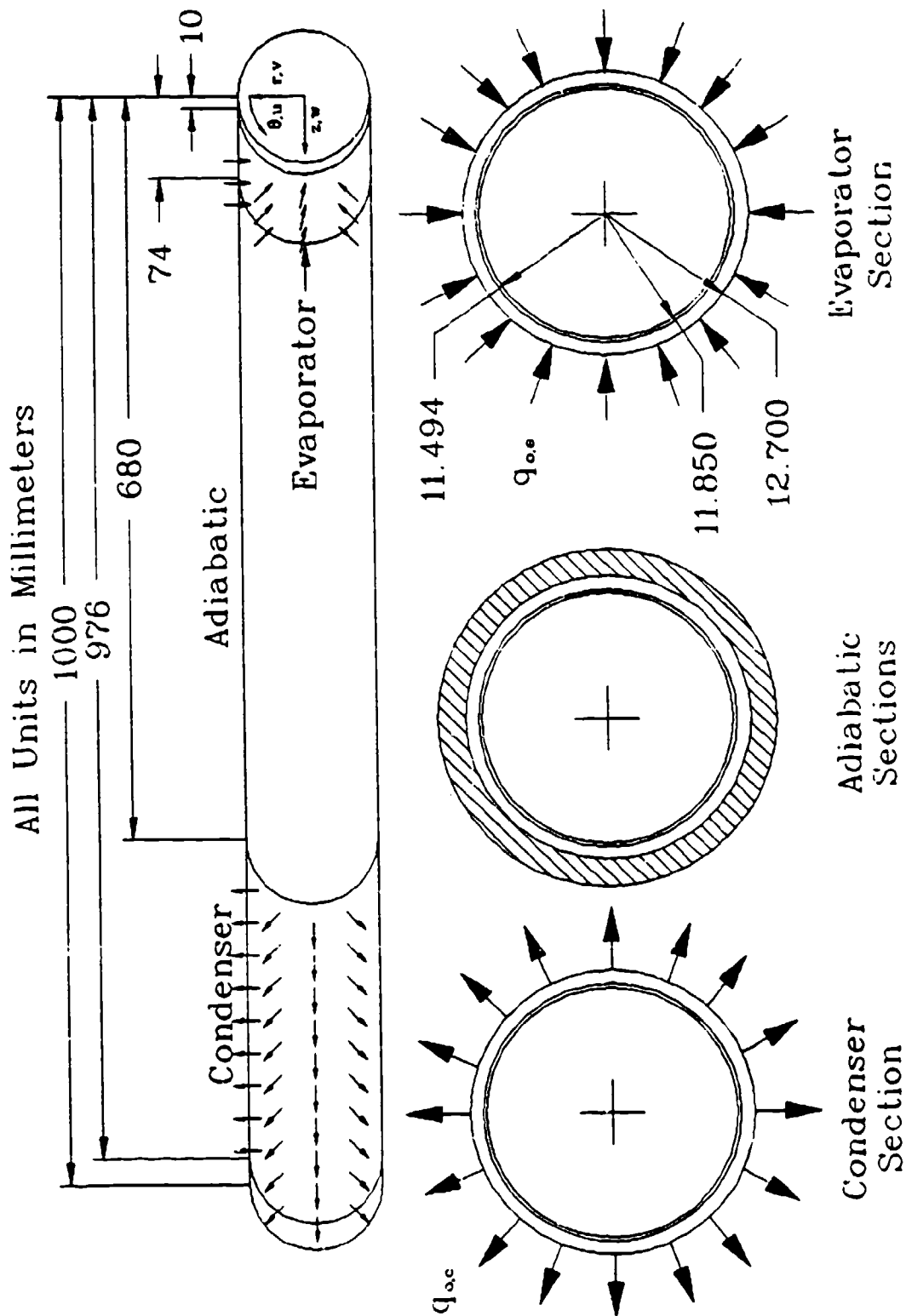


Figure 4.2 Circumferentially-Heated Heat Pipe Model

respectively. The components of velocity in the  $r$ ,  $\theta$ , and  $z$  directions were  $v$ ,  $u$ , and  $w$ , respectively. In the block-heated model, a plane of symmetry along the  $r$  and  $z$  axes was established so that only half of the heat pipe needed to be modeled.

The flow in the vapor region was considered to be compressible, laminar, and steady. The heat transfer through the liquid-wick region was modeled as pure conduction with no fluid flow by using the effective thermal conductivity of the working fluid and wick material. The properties of the working fluid and wall material were constant and the vapor density of the working fluid followed the perfect-gas law. Evaporation and condensation occurred only at the inner radius of the liquid-wick region. At the liquid-wick/vapor interface, the vapor temperature was calculated using the Clausius-Clapeyron equation. At the liquid-wick/vapor and liquid-wick/wall interfaces, the harmonic mean of the thermal conductivity was used in the energy equation. The elliptic versions of the conservation equations were solved as a one-domain conjugate problem. Gravity and other body force terms were neglected.

Under these assumptions, the conservation equations in the vapor region are (Ganic et al., 1985):

Mass:

$$\frac{1}{r} \frac{\partial}{\partial r} (\rho r v) + \frac{1}{r} \frac{\partial}{\partial \theta} (\rho u) + \frac{\partial}{\partial z} (\rho w) = 0 \quad (4.1)$$

$r$ -momentum:

$$\begin{aligned}
\rho \left[ v \frac{\partial v}{\partial r} + \frac{u}{r} \frac{\partial v}{\partial \theta} - \frac{u^2}{r} + w \frac{\partial v}{\partial z} \right] &= - \frac{\partial P}{\partial r} \\
+ \frac{1}{r} \frac{\partial}{\partial r} \left[ 2r\mu \left[ \frac{\partial v}{\partial r} - \frac{1}{3} \left[ \frac{1}{r} \frac{\partial}{\partial r} (rv) + \frac{1}{r} \frac{\partial u}{\partial \theta} + \frac{\partial w}{\partial z} \right] \right] \right] &+ \frac{1}{r} \frac{\partial}{\partial \theta} \left[ \mu \left[ r \frac{\partial}{\partial r} \left( \frac{u}{r} \right) + \frac{1}{r} \frac{\partial v}{\partial \theta} \right] \right] \\
- \frac{2\mu}{r^2} \left[ \frac{\partial u}{\partial \theta} + v - \frac{1}{3} \left[ \frac{\partial}{\partial r} (rv) + \frac{\partial u}{\partial \theta} + r \frac{\partial w}{\partial z} \right] \right] &+ \frac{\partial}{\partial z} \left[ \mu \left[ \frac{\partial w}{\partial r} + \frac{\partial v}{\partial z} \right] \right] \quad (4.2)
\end{aligned}$$

$\theta$ -momentum:

$$\begin{aligned}
\rho \left[ v \frac{\partial u}{\partial r} + \frac{u}{r} \frac{\partial u}{\partial \theta} + \frac{vu}{r} + w \frac{\partial u}{\partial z} \right] &= - \frac{1}{r} \frac{\partial P}{\partial \theta} + \frac{1}{r^2} \frac{\partial}{\partial r} \left[ r^3 \mu \left[ \frac{\partial}{\partial r} \left( \frac{u}{r} \right) + \frac{1}{r^2} \frac{\partial v}{\partial \theta} \right] \right] \\
+ \frac{1}{r} \frac{\partial}{\partial \theta} \left[ \frac{2\mu}{r} \left[ \frac{\partial u}{\partial \theta} + v - \frac{1}{3} \left[ \frac{\partial}{\partial r} (rv) + \frac{\partial u}{\partial \theta} + r \frac{\partial w}{\partial z} \right] \right] \right] &+ \frac{\partial}{\partial z} \left[ \mu \left[ \frac{\partial u}{\partial z} + \frac{1}{r} \frac{\partial v}{\partial \theta} \right] \right] \quad (4.3)
\end{aligned}$$

$z$ -momentum:

$$\begin{aligned}
\rho \left[ v \frac{\partial w}{\partial r} + \frac{u}{r} \frac{\partial w}{\partial \theta} + w \frac{\partial w}{\partial z} \right] &= - \frac{\partial P}{\partial z} + \frac{1}{r} \frac{\partial}{\partial r} \left[ r\mu \left[ \frac{\partial w}{\partial r} + \frac{\partial v}{\partial z} \right] \right] \\
+ \frac{1}{r} \frac{\partial}{\partial \theta} \left[ \mu \left[ \frac{\partial u}{\partial z} + \frac{1}{r} \frac{\partial v}{\partial \theta} \right] \right] &+ \frac{\partial}{\partial z} \left[ 2\mu \left[ \frac{\partial w}{\partial z} - \frac{1}{3r} \left[ \frac{\partial}{\partial r} (rv) + \frac{\partial u}{\partial \theta} + r \frac{\partial w}{\partial z} \right] \right] \right] \quad (4.4)
\end{aligned}$$

Energy:

$$\begin{aligned}
\rho C_p \left[ v \frac{\partial T}{\partial r} + \frac{u}{r} \frac{\partial T}{\partial \theta} + w \frac{\partial T}{\partial z} \right] &= \\
k_v \left[ \frac{1}{r} \frac{\partial}{\partial r} \left[ r \frac{\partial T}{\partial r} \right] + \frac{1}{r^2} \frac{\partial^2 T}{\partial \theta^2} + \frac{\partial^2 T}{\partial z^2} \right] &+ 2\mu \left[ \left[ \frac{\partial v}{\partial r} \right]^2 + \left[ \frac{1}{r} \left[ \frac{\partial u}{\partial \theta} + v \right] \right]^2 + \left[ \frac{\partial w}{\partial z} \right]^2 \right] \\
+ \mu \left[ \left[ \frac{\partial u}{\partial z} + \frac{1}{r} \frac{\partial v}{\partial \theta} \right]^2 + \left[ \frac{\partial w}{\partial r} + \frac{\partial v}{\partial z} \right]^2 + \left[ \frac{1}{r} \frac{\partial v}{\partial \theta} + r \frac{\partial}{\partial r} \left( \frac{u}{r} \right) \right]^2 \right] & \\
- \frac{2}{3} \mu \left[ \frac{1}{r} \frac{\partial}{\partial r} (rv) + \frac{1}{r} \frac{\partial u}{\partial \theta} + \frac{\partial w}{\partial z} \right]^2 &+ v \frac{\partial P}{\partial r} + \frac{u}{r} \frac{\partial P}{\partial \theta} + w \frac{\partial P}{\partial z} \quad (4.5)
\end{aligned}$$

For the wall and the liquid-wick regions the energy equation simplified to:

$$\frac{k}{r} \frac{\partial}{\partial r} \left[ r \frac{\partial T}{\partial r} \right] + \frac{k}{r^2} \left[ \frac{\partial^2 T}{\partial \theta^2} \right] + k \left[ \frac{\partial^2 T}{\partial z^2} \right] = 0 \quad (4.6)$$

In the pipe wall, the thermal conductivity in equation (4.6) is  $k_s$ . The effective thermal conductivity for the liquid-wick region,  $k_{eff}$ , was calculated for a screen mesh wick as follows (Chi, 1976):

$$k_{eff} = \frac{k_\ell [k_\ell + k_w - (1 - \epsilon) (k_\ell - k_w)]}{k_\ell + k_w + (1 - \epsilon) (k_\ell - k_w)} \quad (4.7)$$

where  $k_\ell$  is the thermal conductivity of the liquid and  $k_w$  is that of the wick material. The wick porosity in equation (4.7) was given by Chang (1987):

$$\epsilon = 1 - \frac{\pi CD}{2(1 + C)} \quad (4.8)$$

where  $C$  is the ratio of the wire diameter to the opening width of the screen, and  $D$  is the ratio of the wire diameter to the screen thickness.

The Clausius-Clapeyron equation was used to determine the vapor temperature from the saturation vapor pressure at the liquid-wick/vapor interface.

$$T_v = \frac{1}{\frac{1}{T_0} - \frac{R}{h_{fg}} \ln \frac{P_v}{P_0}} \quad (4.9)$$

where  $T_0$  and  $P_0$  are the reference saturation temperature and pressure imposed at the evaporator end cap. If  $P_0$  is set to a datum pressure, the absolute pressure distribution in the vapor region can be found.

The ideal gas law was needed to solve for the density because of compressibility effects.

$$P_v = \rho R T_v \quad (4.10)$$

The various boundary condition specifications required for the conservation equations are summarized in Table 4.1.

#### 4.4 NUMERICAL SOLUTION PROCEDURE

The circumferentially-heated and block-heated models were solved as a single domain, convection-conduction problem with three radial regions: pipe wall, liquid-wick, and vapor. The heat transfer through the wall and liquid-wick was treated as pure conduction by neglecting the liquid flow in the wick. To account for the discontinuity in the thermal conductivity at the liquid-wick/wall and the liquid-wick/vapor interfaces, the transport coefficient in the energy equation was evaluated using the harmonic mean of values from each side of the interface (Patankar 1980).

The generalized finite-difference method of solution developed by Spalding (1980) was used to solve the elliptic conservation equations with the

**TABLE 4.1**  
**Boundary Conditions for Circumferentially-Heated and**  
**Block-Heated Heat Pipe Models**

	Evaporator ( $0 \leq z \leq L_e$ )	Adiabatic ( $L_e \leq z \leq L_e + L_a$ )	Condenser ( $L_e + L_a \leq z \leq L$ )
Outer Pipe Wall ( $r = r_w$ )  (circumferential heating)	$0 \leq \theta \leq 2\pi$ : $q_{o,e} = -k_s \frac{\partial T_s}{\partial r}$  = constant	$\frac{\partial T_s}{\partial r} = 0$	$q_{o,c} = -q_{o,e}$ $= -k_s \frac{\partial T_s}{\partial r}$ = constant
Outer Pipe Wall ( $r = r_w$ )  (block heating)	$0 \leq \theta \leq \frac{\pi}{2}$ : $q_{o,e} = -k_s \frac{\partial T_s}{\partial r}$  = constant  $\frac{\pi}{2} \leq \theta \leq \pi$ : $\frac{\partial T_s}{\partial r} = 0$	$\frac{\partial T_s}{\partial r} = 0$	$q_{o,c} = q_{o,e} \frac{\lambda_c}{\lambda_e}$ $= -k_s \frac{\partial T_s}{\partial r}$ = constant
Wall/Liquid-Wick Interface ( $r = r_v + t_w$ )	$T_{lw} = T_s, k_s \frac{\partial T_s}{\partial r} = k_{eff} \frac{\partial T_{lw}}{\partial r}$		
Liquid-Wick/Vapor Interface ( $r = r_v$ )	$w_v = u_v = 0, v = \frac{\dot{m}}{\rho_v}, T_v = \left[ \frac{1}{T_0} - \frac{R}{h_{fg}} \ln \frac{P_v}{P_0} \right]^{-1}$  $q = \dot{m} h_{fg} = k_v \frac{\partial T_v}{\partial r} - k_{eff} \frac{\partial T_{lw}}{\partial r}$		
Centerline ( $r=0$ ) (circumferential heating)	$\frac{\partial u}{\partial r} = \frac{\partial w}{\partial r} = v = \frac{\partial T}{\partial r} = \frac{\partial P}{\partial r} = 0$		
Centerline ( $r = 0$ ) (block heating)	$u = \frac{\partial w}{\partial r} (0, \frac{\pi}{2}, z) = v = \frac{\partial T}{\partial r} (0, \frac{\pi}{2}, z) = \frac{\partial P}{\partial r} (0, \frac{\pi}{2}, z) = 0$		
End Caps ( $z = 0, L$ )	$u = v = w = \frac{\partial T}{\partial z} = 0, P(z = 0) = P_0$		
Periodic	All the dependent variables are assumed to be periodic with a period of $2\pi$		

boundary conditions given in Table 4.1. The finite-domain equations were derived by integration of the differential conservation equations over a control volume surrounding a grid node. The integrated source term caused by viscous dissipation and the pressure term in the energy equation were linearized and the SIMPLEST practice (Spalding, 1980) was used to solve the momentum equations. The SIMPLEST method of solution involves guessing the pressure field and then solving the momentum equations to obtain the velocity components. The pressure is then corrected and the entire procedure repeated until convergence is achieved. The difference between SIMPLE and SIMPLEST lies in the way that the convection terms were handled in the momentum finite difference equations (FDEs). In SIMPLEST, the momentum FDEs are initially solved using diffusion contributions only. The conduction terms are then added when the pressure distribution is corrected. The hybrid scheme was used to determine the coefficients. When the absolute value of a cell Peclet number was greater than 2, the upwind differencing scheme was used. Otherwise, a central-difference scheme was used combined with a three-line approximation of the coefficients.

The pressure and temperature terms were solved using a whole-field approach which takes into account the effects from all three directions simultaneously. The velocity components were solved using a slab-by-slab approach in the axial direction. A false time step relaxation factor equal to the average cell transverse time was used to aid in convergence of the velocity components.

The term  $\dot{m}h_{fg}$  was added to the source term in the energy balance at the liquid-wick/vapor interface in the evaporator and condenser sections to

account for the latent heat of evaporation and condensation. The heat flux at the liquid-wick/vapor interface was assumed to be equal that at the outer wall for the first 150 iterations, and then corrected to an exact energy balance for the remaining iterations. This was done to reduce the possibility of divergence in the initial iterations.

Convergence was determined by examining the difference in the absolute values of the dependent variables between two successive iterations in a single cell. If the difference was less than  $10^{-4}$ , the cell was considered to be converged. A centerline cell near the condenser end cap was used for this convergence check. Also, when the sum of the absolute volumetric errors over the whole field was less than  $10^{-7}$  and steadily decreasing with increasing iterations, the solution was considered to be converged. In the circumferentially-heated heat pipe model, the number of grids in the axial and radial directions were doubled until the converged solution did not vary by more than 1% with grid size. In the block-heated model, the number of grids in the radial and axial directions were increased by 10% and the azimuthal direction was doubled until the converged solution did not vary with grid size. There was a limitation on the amount of computer memory available for the block-heated model, which was the reason that the number of grids was not doubled in each axis for the grid independence check. An axial by radial by circumferential grid of 50 x 34 x 16 was used for the circumferentially-heated model and a 50 x 34 x 50 grid was used for the block-heated model for the final numerical results presented in this study.

#### 4.5 RESULTS AND DISCUSSION

The numerical model developed for this study for the two different

heating distributions was examined for a 100-W heat input. The outer wall temperatures from both models were compared to experimental wall temperatures. Excellent agreement was found between the experimental data and the numerical models. The axial component of the velocity at several axial locations was compared between the two heating modes. The outer wall temperature, and centerline pressure and Mach number for the circumferentially-heated model were compared to the two-dimensional model developed by Faghri and Chen (1989). The radial and circumferential components of the velocity in the block-heated model were examined and the existence of swirling flow was discovered.

#### 4.6 CIRCUMFERENTIALLY-HEATED HEAT PIPE MODEL

A 100-W heat input was specified in the evaporator of the circumferentially-heated copper-water heat pipe model. Figure 4.3 shows the wall temperature, centerline pressure, and centerline Mach number comparisons between the present three-dimensional model and the numerical results given by Chen and Faghri (1990). Wall temperature measurements from the experimental setup discussed in Part I are also shown for comparison. The agreement is excellent between the three-dimensional and two-dimensional models in all three figures. This was expected because of the symmetry of the model in the azimuthal direction. Figure 4.3a shows the outer wall temperatures along the top of the experimental heat pipe and the numerical model. The difference between the numerical wall temperatures and the experimental data in the condenser section was due to the simplifying assumption of uniform heat removal in the numerical model. Figure 4.3b shows the relative pressure distribution. The reference pressure at the evaporator end cap was fixed to zero. If the operating pressure at the evaporator end cap is added to this

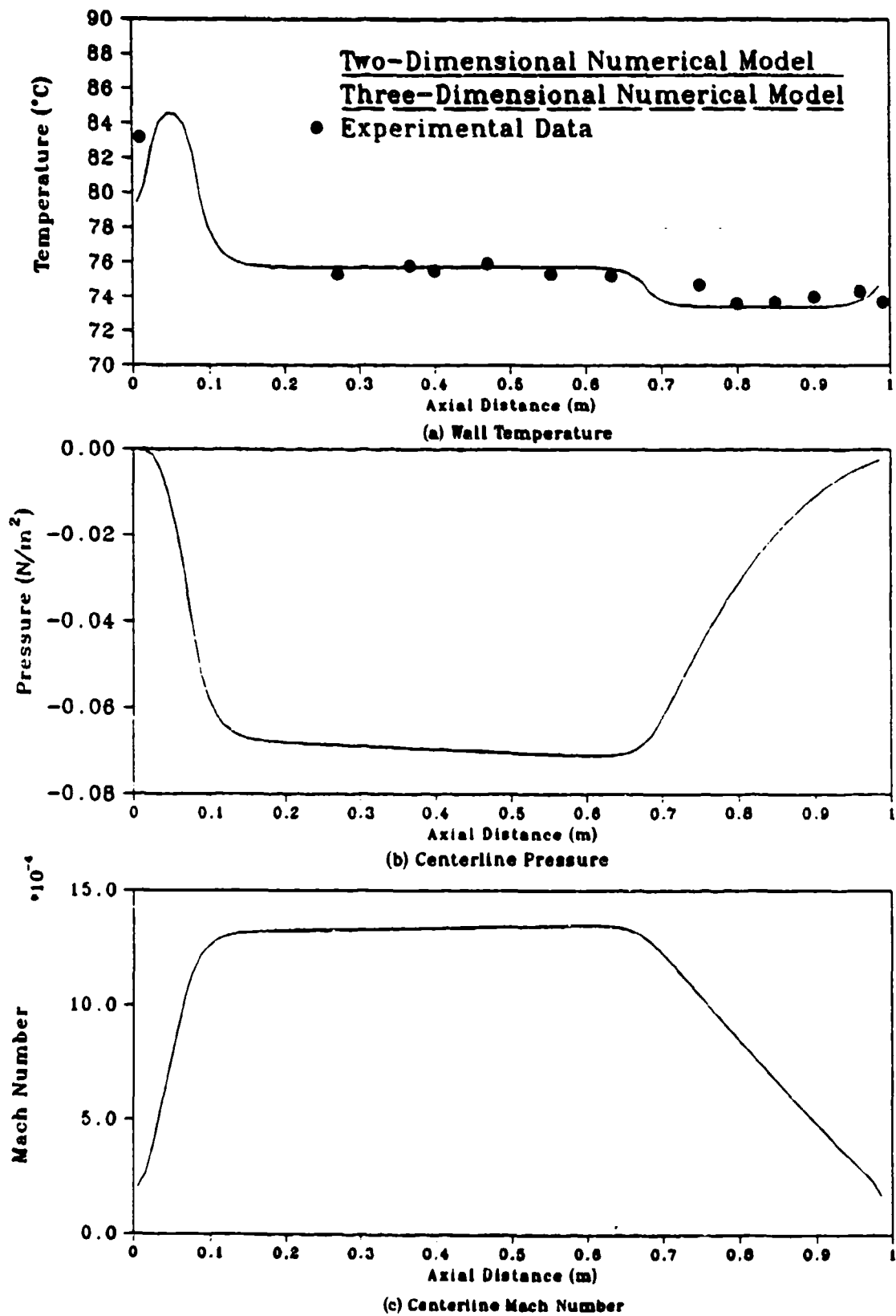
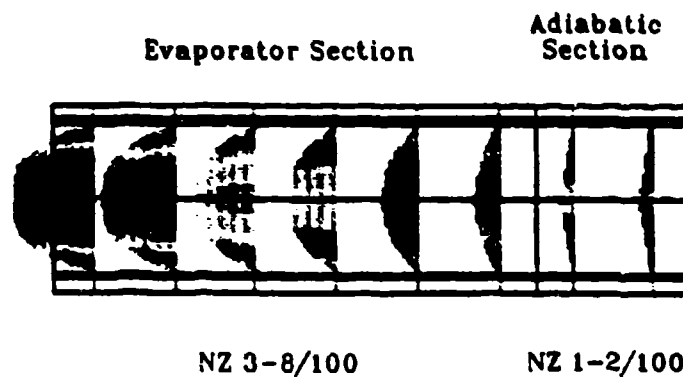


Figure 4.3 Circumferentially-Heated Heat Pipe,  $Q = 100$  W

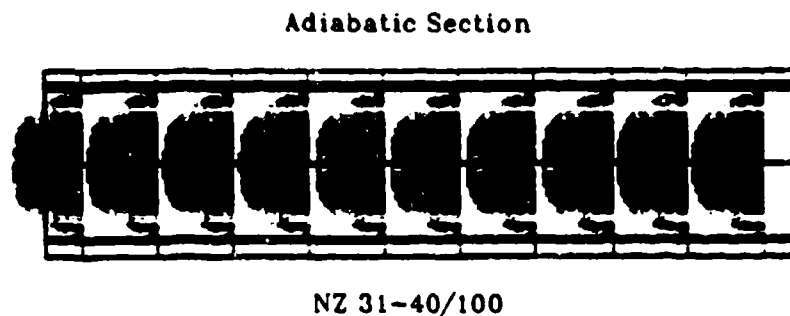
pressure distribution, the actual pressure profile can be found.

Two opposite azimuthal grids were used in Fig. 4.4 to show the symmetry of the velocity profile about the centerline at various axial locations. Figure 4a shows the axial variation of the velocity profile in the region around the evaporator section. As expected, the velocity profile was symmetric about the heat pipe centerline and the magnitude increased from the evaporator end cap because of the addition of mass from evaporation. Figure 4.4b shows the axial variation of the velocity profile in the middle of the adiabatic section. The flow field appears to be fully developed in this section. There was little or no change in the velocity profile in the axial grids about the center of the adiabatic region. Figure 4.4c shows the velocity profile in the condenser section of the heat pipe model, which also shows the symmetry of the velocity profile about the centerline. The magnitude of the velocity profile was reduced as the amount of vapor decreases because of condensation. Vapor flow reversal occurred near the liquid-wick/vapor interface, which was caused by the significant amount of pressure recovery.

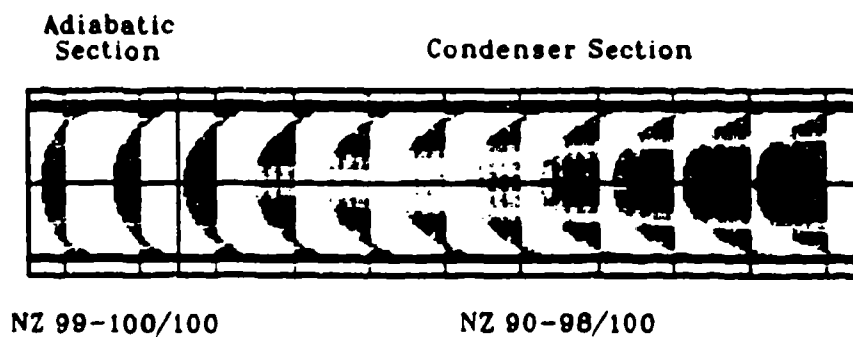
Figure 4.5 shows the outer wall temperature profile along the circumferentially-heated model, which was uniform around the circumference. The wall temperature quickly dropped along the axial direction in the region around the center of the evaporator. The wall temperature in the adiabatic section was uniform in the axial direction throughout most of its length. The condenser had the coldest wall temperatures which were uniform in the axial direction except at the beginning and the end.



(a) Evaporator Section



(b) Adiabatic Section



(c) Condenser Section

Figure 4.4      Axial Variation of Velocity for the Circumferentially-Heated Heat Pipe,  $Q = 100 \text{ W}$

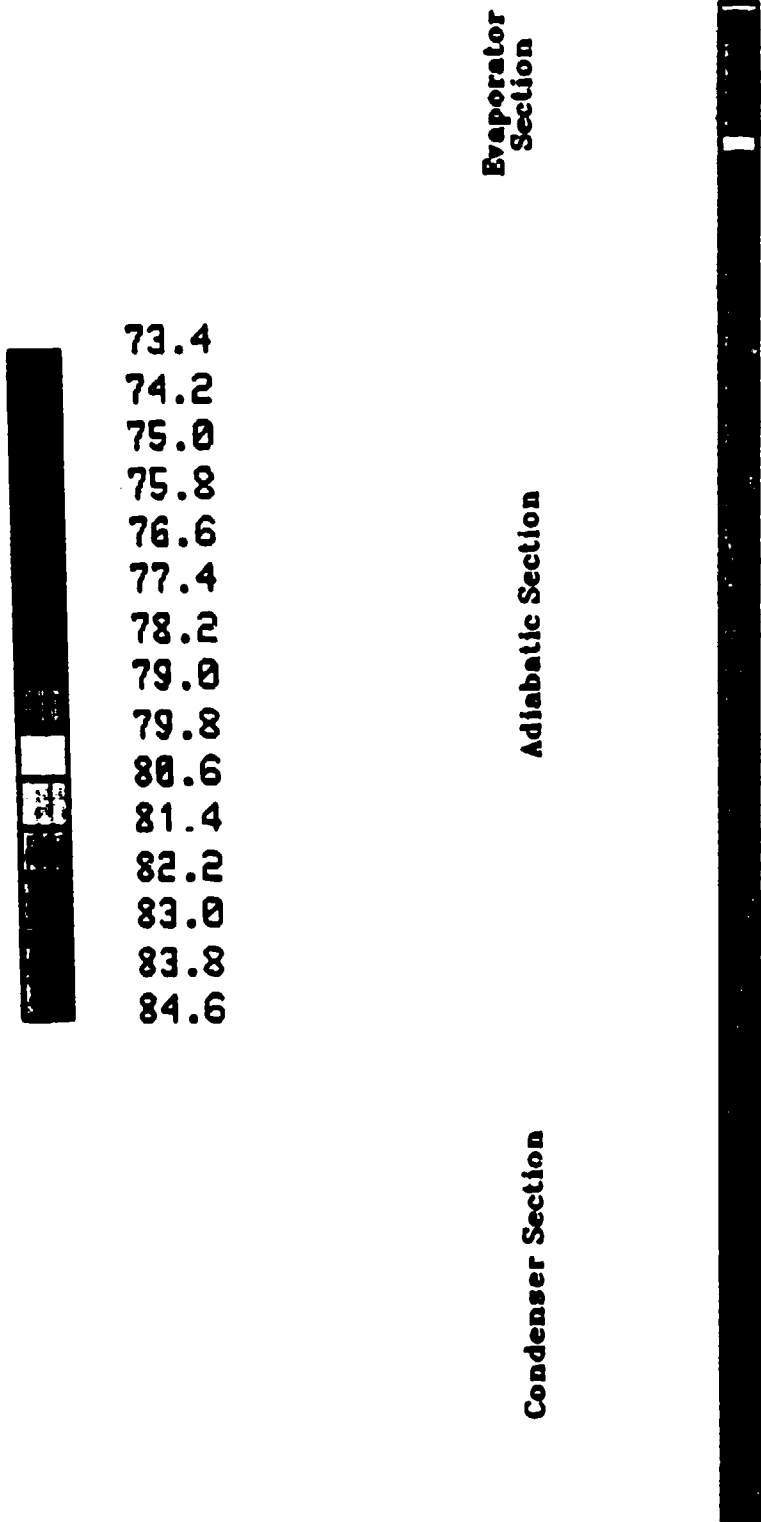


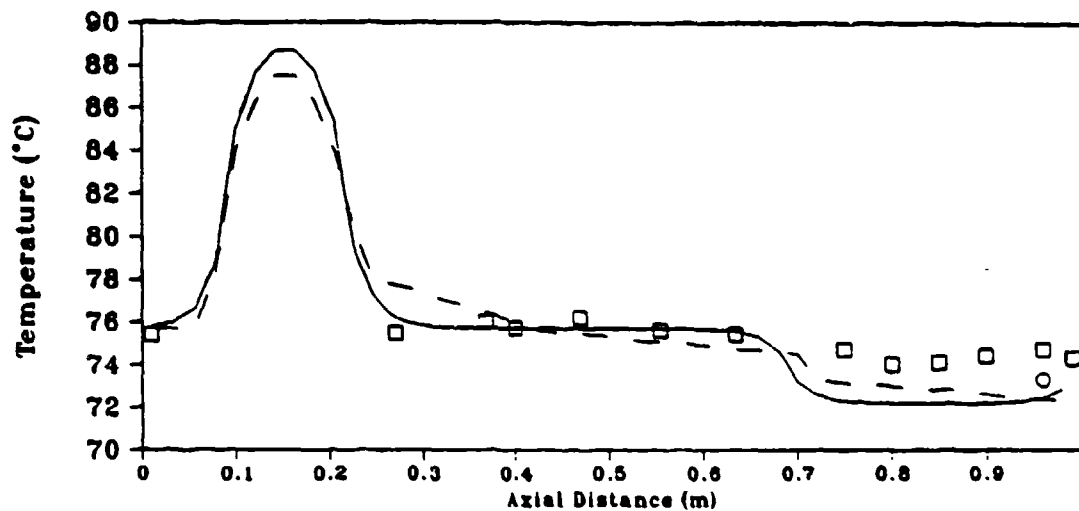
Figure 4.5 Outer Wall Temperature for the Circumferentially-Heated Heat Pipe ( $^{\circ}\text{C}$ ),  $Q = 100\text{ W}$

#### 4.7 BLOCK-HEATED HEAT PIPE MODEL

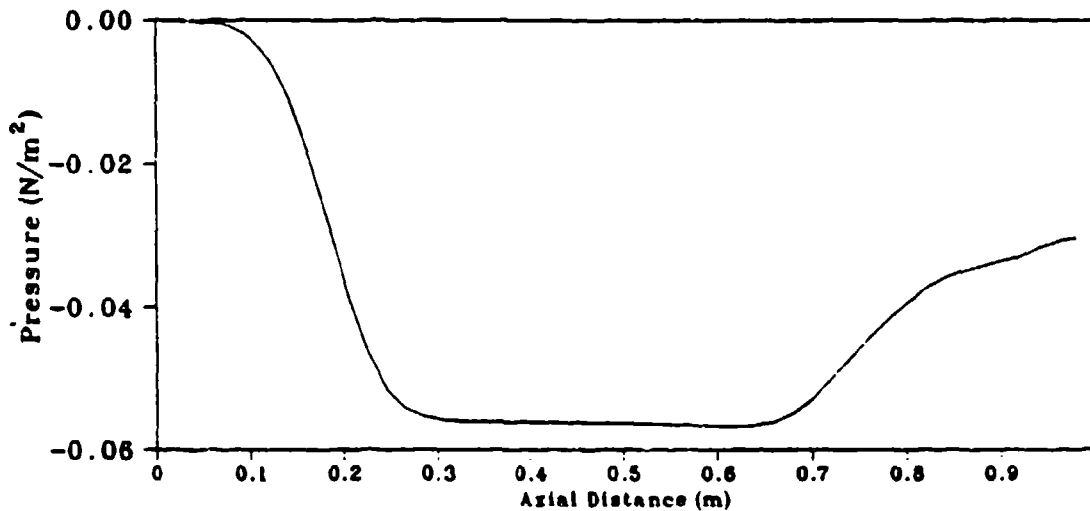
The numerical results of the block-heated heat pipe model were compared to experimental data taken from the block-heated copper-water heat pipe (Part I) with a heat input of 100 W. Figure 4.6a shows the experimental outer wall temperatures along the top of the heat pipe compared to the numerical model. The agreement between the numerical model and the experimental data was excellent except in the condenser section. These differences were again due to the assumption of a uniform heat flux in the condenser of the numerical model. The centerline pressure distribution is shown in Fig. 4.6b. Because the velocity profile was asymmetric in the circumferential direction, the pressure profile was also asymmetric about the centerline. The circumferential location taken for the centerline in Fig. 4.6b is the same as the one examined in the circumferentially-heated model (Fig. 4.3b). The fluctuations in the pressure near the condenser end cap were due to the significant variations in the vapor velocity that is swirling. The relative pressure distribution is shown in Fig. 4.6b.

Figure 4.7a shows the axial variation of the velocity vector profile in the region around the evaporator. From the evaporator end cap to the heated region, the axial component was symmetric about the heat pipe centerline because conjugate heat conduction tends to spread the heat over the entire circumference. From the beginning of the heated region to the condenser end cap, the location of the maximum velocity shifted toward the bottom of the heat pipe. This was due to the blowing in the evaporator section at the top of the heat pipe model.

The axial variation of the velocity profile near the center of the



(a) Wall Temperatures



(b) Centerline Pressure

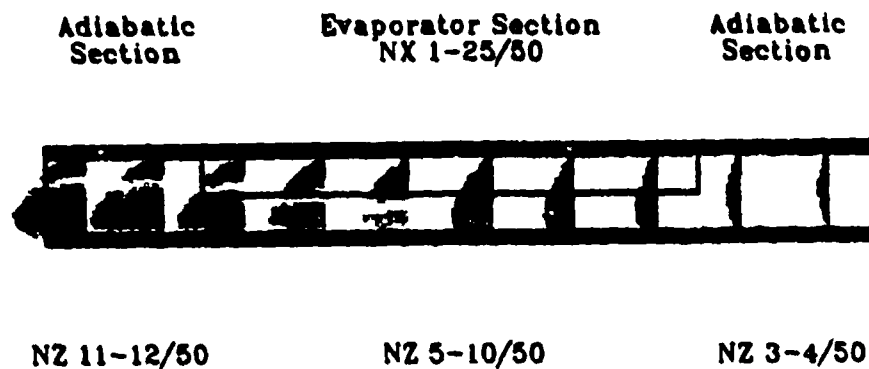
Numerical Model, Top of Pipe

□ Experimental Data, Top of Pipe

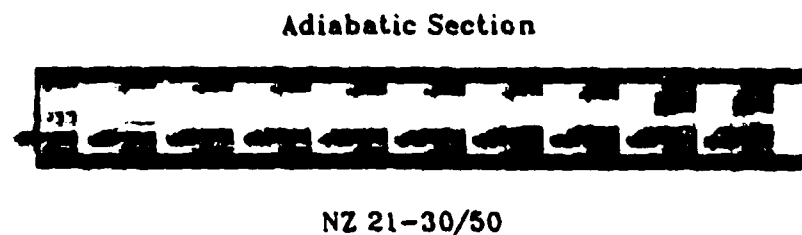
Numerical Model, Bottom of Pipe

○ Experimental Data, Bottom of Pipe

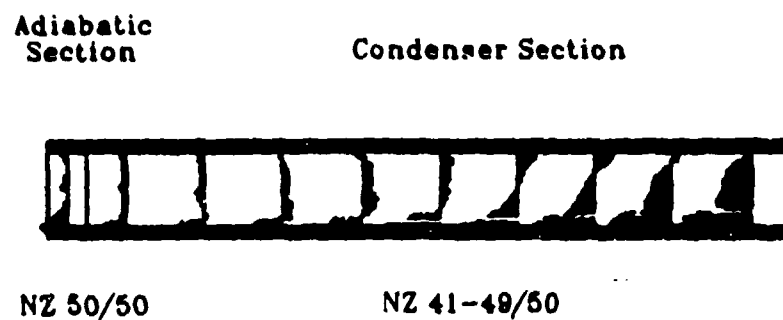
Figure 4.6 Block-Heated Heat Pipe  $Q = 100 \text{ W}$



(a) Evaporator Section



(b) Adiabatic Section



(c) Condenser Section

Figure 4.7 Axial Variation of Velocity for the Block-Heated Heat Pipe Model,  $Q = 100 \text{ W}$

adiabatic section is given in Fig. 4.7b. Unlike the circumferentially-heated model, the velocity profile peak changed slightly in both magnitude and location over the length of the adiabatic region. The vapor velocity field began to exhibit a significant amount of swirling which started in the heated region and grew as the flow moved away from the evaporator end cap. This swirling caused considerable asymmetry in the velocity profile in the condenser section. The swirling will be shown and discussed in more detail in Figs. 4.9-4.11.

Figure 4.7c shows the axial variation of the velocity profile near the condenser end cap. Because the swirling was dispersed throughout the vapor region, there was no smooth transition in the velocity profile from the top to the bottom of the model in the last six axial grids.

In comparing Figs. 4.4 and 4.7, significant differences were found between the circumferentially-heated and the block-heated models. The circumferentially-heated heat pipe velocity profile was symmetric about the centerline of the model and was fully developed in the adiabatic region. This was shown by the lack of significant changes in the velocity profile through several axial locations in the adiabatic section (Fig. 4.4b). The block-heated model shows no symmetry about the centerline except for the small adiabatic section between the evaporator end cap and the heated region. Even in the condenser section of the block-heated model, the flow remains asymmetric, with most of the reverse flow taking place at the top of the vapor space. The blowing from the block heater causes the vapor flow to move to the bottom of the vapor region and the length of the pipe was insufficient for the flow field to develop to a symmetric flow about the centerline.

Figure 4.8 shows the wall temperature of the block-heated heat pipe model. The heat pipe wall temperature was symmetric in the azimuthal direction throughout most of its length, except in the region about the block heater.

Figures 4.9-4.11 present the radial and circumferential components of the velocity vector as seen looking down the pipe axis. Figure 4.9a is from the first axial grid of the evaporator section of the block-heated heat pipe model. Along the top half of the model, the blowing representing the evaporation of the working fluid from the heated region was present. In conjunction with Fig. 4.7a, it was determined that the majority of the vapor from the blowing region flowed around the circumference to the bottom and then down the length of the heat pipe.

Figure 4.9b is from the second grid in the evaporator section. The flow field was similar to that in Fig. 4.9a except for the appearance of a small amount of counterclockwise swirling in the vapor flow field near the liquid-wick/vapor interface, just below the point where the heated region and the insulated region meet. Further down the heat pipe, this swirling encompassed an increasing amount of the vapor region. Figure 4.9c is from the middle of the evaporator section. The flow field followed the same general pattern as in Figs. 4.9a and 4.9b, but the area of swirling grew in size and magnitude. Figure 4.9d is from the end of the evaporator section. The swirling developed even more and affected about half the vapor radius in the region near the circumferential point where the heater and insulated regions meet.

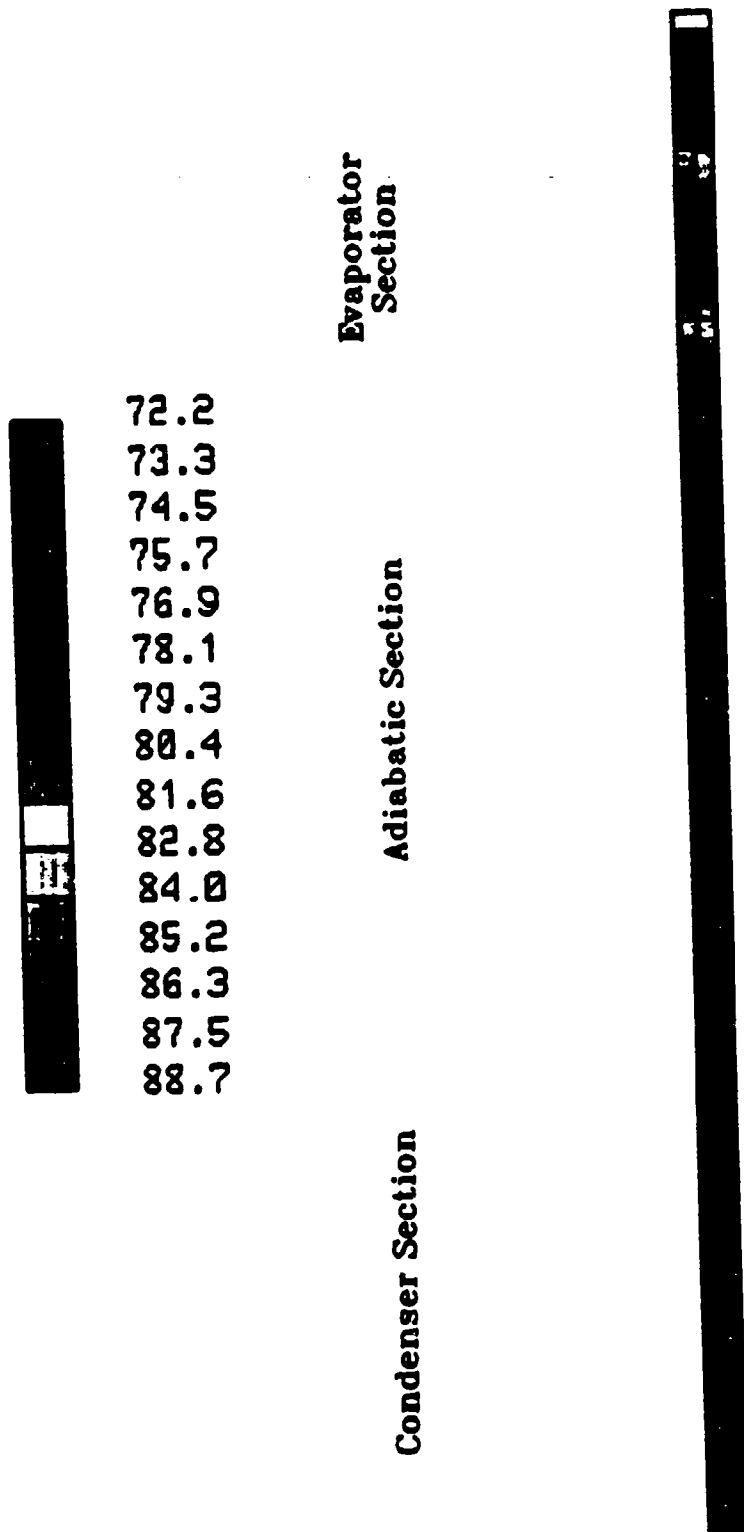
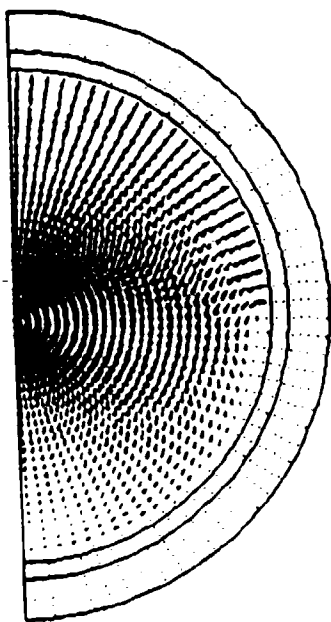
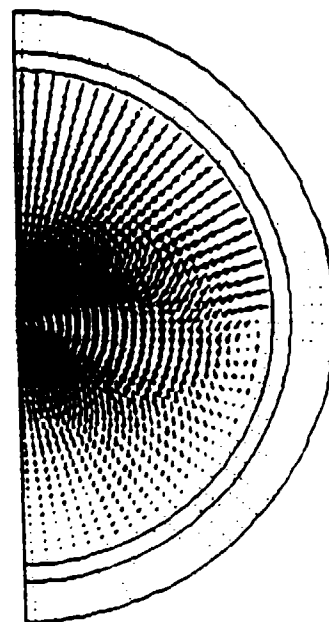


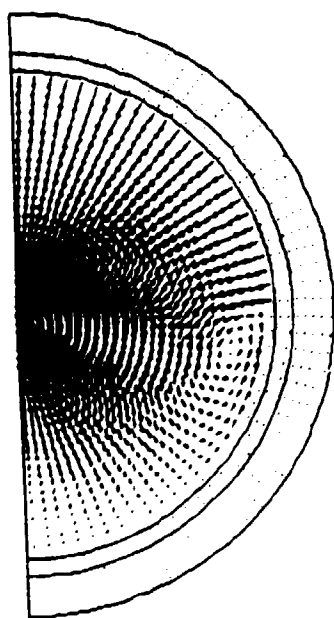
Figure 4.8 Outer Wall Temperatures for the Block-Heated Heat Pipe Model ( $^{\circ}\text{C}$ ),  $Q = 100 \text{ W}$



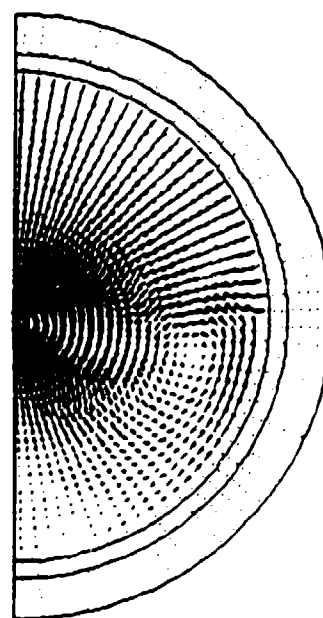
(a) NZ 5/50



(b) NZ 6/50

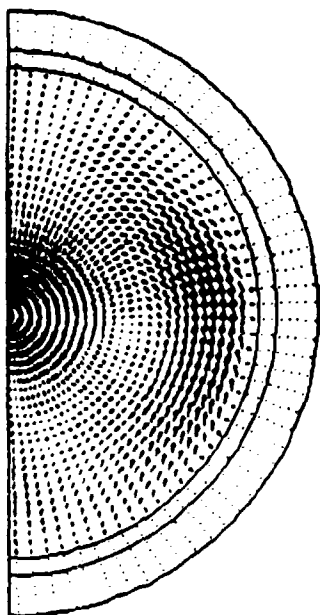


(c) NZ 8/50

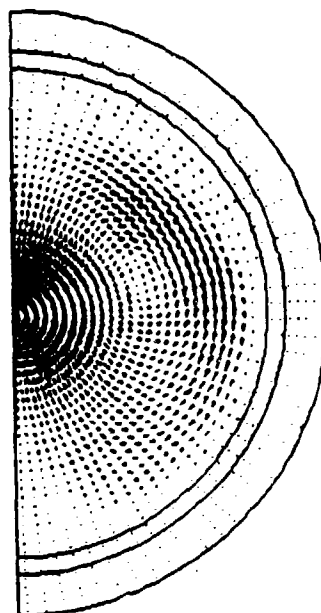


(d) NZ 10/50

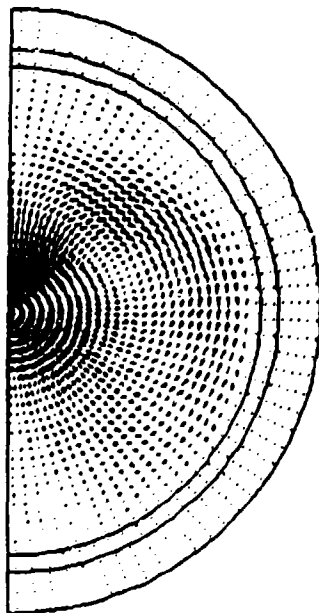
Figure 4.9 Velocity Variation in the Radial and Circumferential Directions in the Evaporator Section of the Block-Heated Heat Pipe Model,  $Q = 100 \text{ W}$



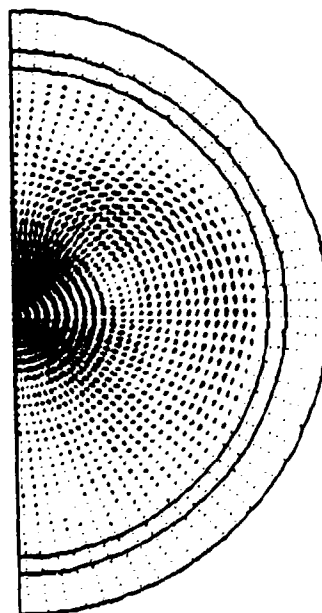
(a) NZ 11/50



(b) NZ 15/50

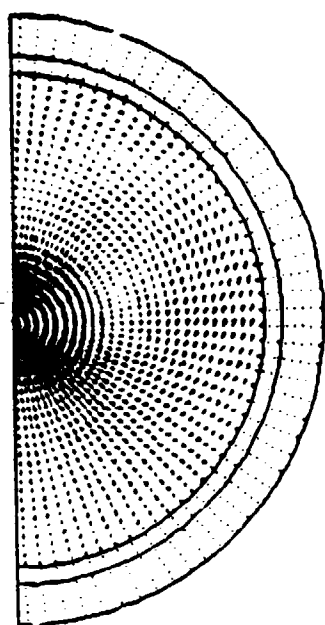


(c) NZ 20/50

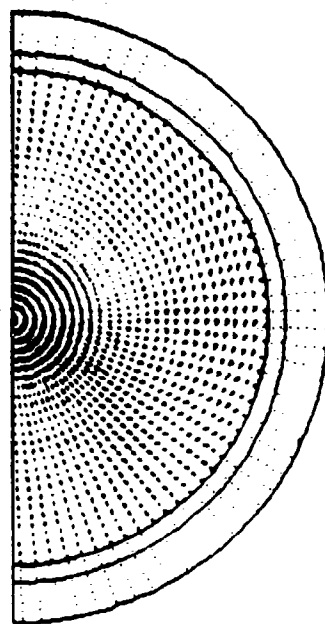


(d) NZ 25/50

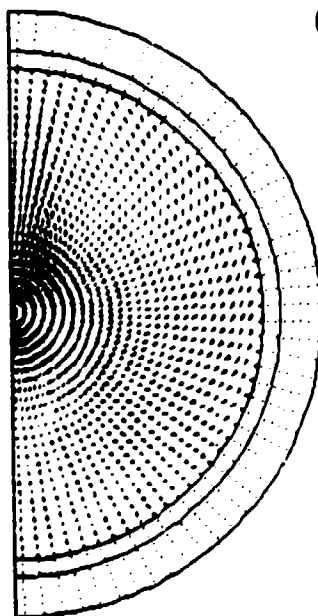
Figure 4.10 Velocity Variation in the Radial and Circumferential Directions in the Adiabatic Section of the Block-Heated Heat Pipe Model,  $Q = 100$  W



(a) NZ 35/50



(b) NZ 40/50



(c) NZ 45/50

Figure 4.11 Velocity Variation in the Radial and Circumferential Directions in the Condenser Section of the Block-Heated Heat Pipe Model,  $Q = 100 \text{ W}$

Figure 4.10a is from the first axial grid of the adiabatic section. With the elimination of most of the blowing along the top of the vapor region, the swirling moved into the top half of the model. Even though most of the flow field was affected by the swirling, the first and last grid in the circumferential direction were not, and so when viewed from the side (Fig. 4.7a) a smooth transition from the top to the bottom of the model still appeared in the velocity flow field.

Figure 4.10b is from a few grids further from the evaporator than Fig. 4.10a. From this axial location onwards, the swirling affected the entire vapor region. The magnitude of the swirling had a profound effect on the location of the maximum velocity. Figure 4.10c is an axial view of the radial and circumferential components of the velocity at the middle of the adiabatic section. The center of the swirling migrated into the top half of the vapor space. Figure 10d is at the end of the adiabatic section. The swirling continued to grow in magnitude and became more uniform about the vapor space. The center of the swirling shifted slightly towards the top of the pipe.

Figure 4.11a is at the beginning of the condenser section. The uniform suction about the circumference of the liquid-wick/vapor interface can be seen in this figure. The swirling lost some of its momentum from the axial location shown in Fig. 4.10d. This was caused by the removal of mass from the vapor region. Figure 4.11b is from the middle of the condenser section. Although the swirling had lost considerable magnitude, it was still significant at this location. The magnitude of the swirling was no longer uniform about the vapor space. Near the liquid-wick/vapor interface, the magnitude of the swirling was much higher than at the centerline. This

nonuniformity in the swirling caused significant variation in the axial component of the velocity. Figure 4.11c is at the end of the condenser. The center of the swirling had disappeared, but there still was a significant component of the swirling in the vapor space. The remaining effects of the swirling caused the major part of the reversed flow shown in Fig. 4.7c to move to the top of the vapor region. The swirling observed in the numerical model of the block-heated heat pipe was caused by end effects in the circumferential direction at the heater edge.

#### 4.8 CONCLUSIONS

Three-dimensional numerical models of a circumferentially-heated and a block-heated heat pipe were developed. The wall temperatures from both models were compared to experimental data with an excellent agreement. The vapor velocity profiles for block heating were examined and compared to the profiles of the circumferential heating model.

The numerical vapor velocity profiles showed the symmetric nature of the circumferentially-heated heat pipe about the centerline. In the same regions of the block-heated heat pipe, the vapor flow first moves radially away from the heater with only a small portion turning axially before it reaches the far side. There are significant end effects at the edge of the block heater. These caused a significant amount of swirling, which greatly increased the asymmetric nature of the vapor flow. Although the maximum axial velocities of the two models were almost the same, the location of the maximum axial component was significantly different. The maximum velocity of the circumferentially-heated heat pipe occurred at the centerline, whereas the location of the maximum velocity for the block-heated heat pipe stayed near

the liquid-wick/vapor interface opposite the heated section. The flow reversal showed that the pressure recovery in the circumferentially-heated heat pipe occurred near the liquid-wick/vapor interface, but in the block-heated heat pipe it occurred near the plane of symmetry.

## Section V

### TRANSIENT ANALYSIS OF NONCONVENTIONAL HEAT PIPES WITH UNIFORM AND NONUNIFORM HEAT DISTRIBUTIONS

#### 5.1 SUMMARY

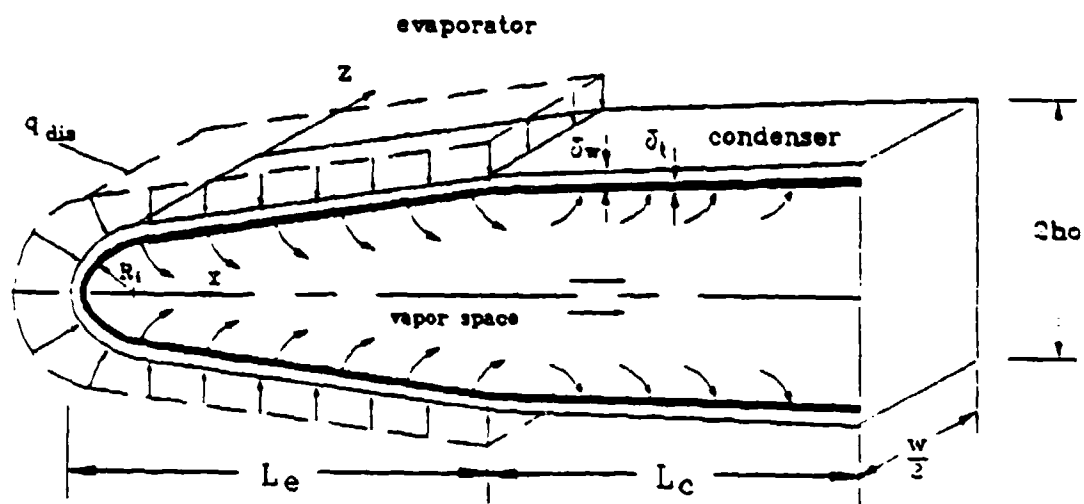
A numerical analysis of transient heat pipe performance including nonconventional heat pipes with nonuniform heat distributions is presented. A body-fitted grid system was applied to a three-dimensional wall and wick model which was coupled with a transient compressible quasi - one-dimensional vapor flow model. The numerical results were first compared with experimental data from cylindrical heat pipes with good agreement. Numerical calculations were then made for a leading edge heat pipe with localized high heat fluxes. Performance characteristics different from conventional heat pipes are illustrated and some operating limits concerning heat pipe design are discussed.

## 5.1 INTRODUCTION

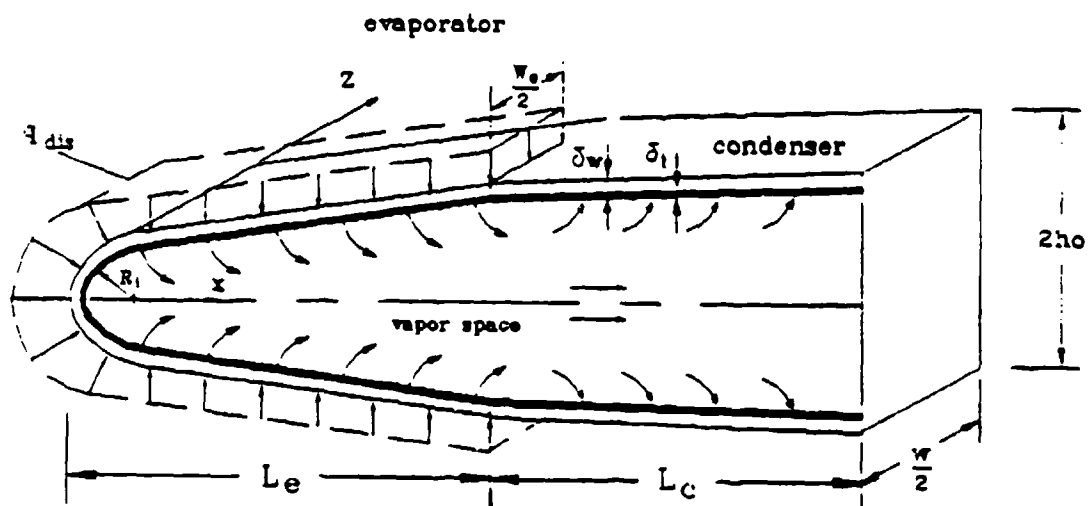
The study of heat pipe dynamics is important in many areas such as the design and operation of space satellite radiators, cooling the leading edges of re-entry vehicles and hypersonic aircraft, electronic equipment cooling, and the cooling of nuclear and isotope reactors.

Since the heat pipe is a very complex system which involves many heat transfer modes, it is very difficult to obtain a generalized analytical solution for the heat pipe dynamics. In recent years, researchers have concentrated on the numerical analysis of transient heat pipe operation. These include Chang and Colwell (1985), Hall and Doster (1990), Bowman and Hitchcock (1988), Jang et al. (1990), and Cao and Faghri (1990). The numerical models involve different assumptions and are at different stages of development. However, most of these numerical analyses deal with conventional cylindrical heat pipes with heat distributions which are uniform around the circumference. Jang (1988) was the only numerical study related to a leading edge heat pipe using a finite element method. Mathematical models have been developed for heat pipe startup from the frozen state. The emphasis of Jang's study was the early transient period of heat pipe startup involving the change of phase in the wick. Neither the coupling of the vapor flow with the wick and wall nor the continuum transient vapor analysis was completed.

The configuration of a leading edge heat pipe is shown in Fig. 5.1, which is considered to be one of the most promising candidates for cooling the leading edges of re-entry vehicles and hypersonic aircraft. In the basic cooling concept, the heat pipe covers the leading edge to be protected. The intense aerodynamic heat is absorbed mainly at the leading edge, and



a) Uniform heating along the heat pipe width



b) Nonuniform heating along the heat pipe width

Figure 5.1 Schematic of the Leading Edge Heat Pipe

transported through the heat pipe to the condenser, where it is rejected by radiation or convection. This nonconventional heat pipe differs from the conventional cylindrical heat pipe in several aspects:

1. The special geometric configuration of the heat pipe makes it difficult to simulate the heat pipe operation with the cartesian or cylindrical coordinate systems since the vapor cross-sectional area changes along the heat pipe length. In this case, one has to resort to the finite element or the finite difference method with body-fitting coordinates.
2. Extremely high heat fluxes at the leading edge make the thickness or the thermal conductivity of the heat pipe wall and wick to be one of the dominant factors of the heat pipe operation. For the conventional heat pipe with a moderate heat flux, the temperature drop across the wall and wick can be neglected without causing a significant error when analyzing the heat pipe operation. However, this is not the case for leading edge heat pipes.
3. The heat distribution at the leading edge is usually not uniform. This makes the heat transfer in the wall and wick generally three-dimensional.

In this report, a numerical modeling for the transient analysis of nonconventional heat pipes with variable cross-sectional areas and nonuniform heat distributions is presented which implemented the above concerns. The numerical results are compared with the relevant experimental data for conventional cylindrical heat pipes, and then the numerical results for a leading edge heat pipe are elaborated.

### 5.3 MATHEMATICAL MODELING

The mathematical formulation for the conventional heat pipe has been given by Jang et al. (1990) and by Cao and Faghri (1990). However, neither study solved the governing equations completely because of the complexity of the problem. The effect of the liquid flow in the wick structure was neglected and the wick structure was assumed to be saturated by the working substance. These assumptions were justified because the thermal conductivity of the liquid metal is high and the thickness of the wick is very thin. This does not mean that the liquid flow in the porous wick is not important. While the liquid flow has a negligible influence on the temperature distribution in the wick, it is very important in the determination of the capillary limit of the heat pipe. In the present study, the liquid flow in the porous wick was considered as a decoupled process and Darcy's law was applied to determine the capillary limit.

As for the transient vapor flow, most of the previous works used one-dimensional models which incorporated friction coefficients found from two-dimensional numerical results or experiments. Cao and Faghri (1990) employed a two-dimensional transient vapor flow model coupled with a two-dimensional wall and wick model. Unfortunately, the scheme could not be directly applied to the present problem because of the nonconventional configuration as well as the three-dimensional heat transfer in the wall and wick. For the multidimensional modeling of the present transient vapor flow, a body-fitting system is needed which would result in a very complicated numerical model. Another concern for the multidimensional modeling of the vapor was that although it eliminated the need for friction coefficients, the computational time needed was dramatically increased. Based on the above

arguments and the fact that the vapor temperature in the transverse directions is rather uniform, a transient compressible quasi - one-dimensional vapor flow model with variable cross-sectional area coupled with a three-dimensional heat transfer model in the wall and wick was chosen in the present study.

To simplify the analysis for the wall and the wick, the heat pipe was assumed to be symmetric about the stagnation line so that only the upper half of the heat pipe was considered. A typical vapor space channel with width  $W$  was considered for the mathematical formulation with the symmetric thermal boundary condition applied on both sides.

### 5.3.1 Heat Pipe Wall and Wick

A body-conforming coordinate system using a multiblock approach was employed in which the region of interest was split into two blocks, each of which was mapped separately with different coordinates. When lower-order blending functions were used, the grid lines usually had some kinks at the nonphysical boundaries. Solution techniques, particularly those based on the Taylor series expansion, might be sensitive to kinks in the grid lines. The finite control-volume methods used here were found to be less sensitive since they are based on flux balances in the cells (Karki, 1986). The body-fitted grid for the heat pipe wall and wick is shown in Fig. 5.2. A cylindrical coordinate system was used at the leading edge up to  $\theta = 90^\circ$ . The energy equation in this region is:

$$(c_p \rho) \frac{\partial T}{\partial t} = \frac{1}{r} \frac{\partial}{\partial r} (rk \frac{\partial T}{\partial r}) + \frac{1}{r^2} \frac{\partial}{\partial \theta} (k \frac{\partial T}{\partial \theta}) + \frac{\partial}{\partial z} (k \frac{\partial T}{\partial z}) \quad (5.1)$$

For the rest of the heat pipe, a cartesian system is used. The corresponding

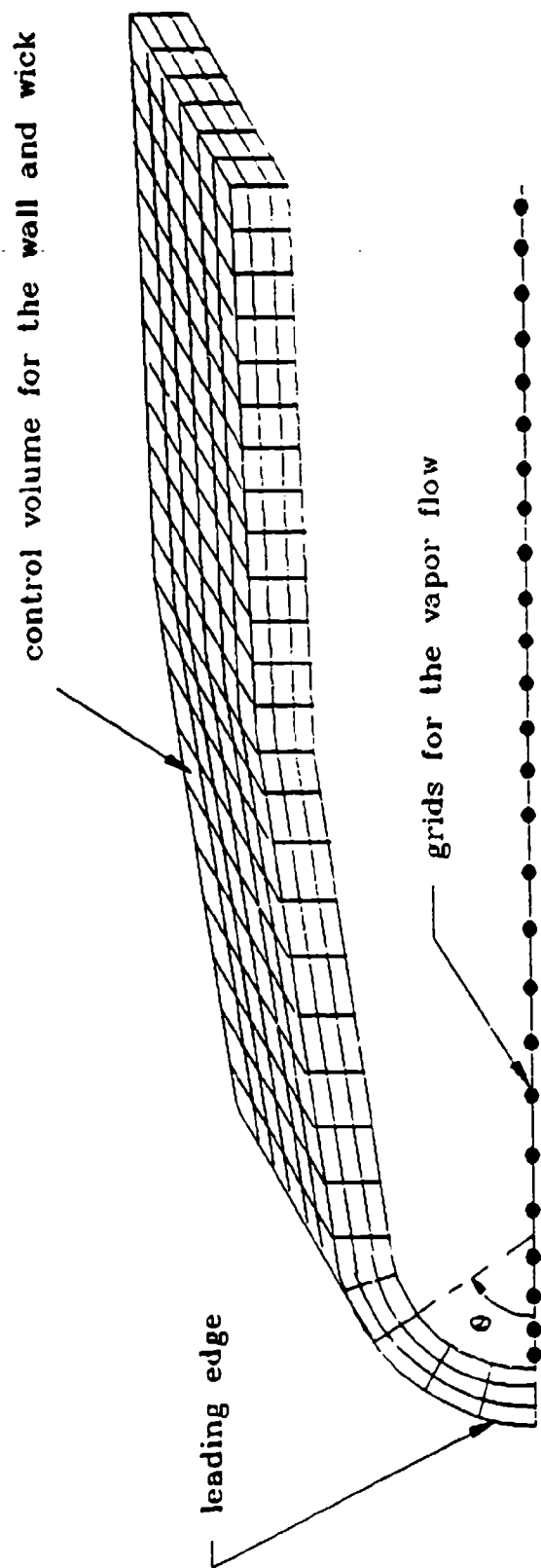


Figure 5.2 Body-Fitted Grids for the Wall and Wick Region  
(not to scale)

energy equation is:

$$(c_p \rho) \frac{\partial T}{\partial t} = \frac{\partial}{\partial x} (k \frac{\partial T}{\partial x}) + \frac{\partial}{\partial y} (k \frac{\partial T}{\partial y}) + \frac{\partial}{\partial z} (k \frac{\partial T}{\partial z}) \quad (5.2)$$

where

$$k = \begin{cases} k_w & \text{for the wall} \\ k_{\text{eff}} & \text{for the wick} \end{cases} \quad (5.3)$$

$$(c_p \rho) = \begin{cases} c_w \rho_w & \text{for the wall} \\ \omega(c_p \rho)_\ell + (1 - \omega)(c_p \rho)_s & \text{for the wick} \end{cases} \quad (5.4)$$

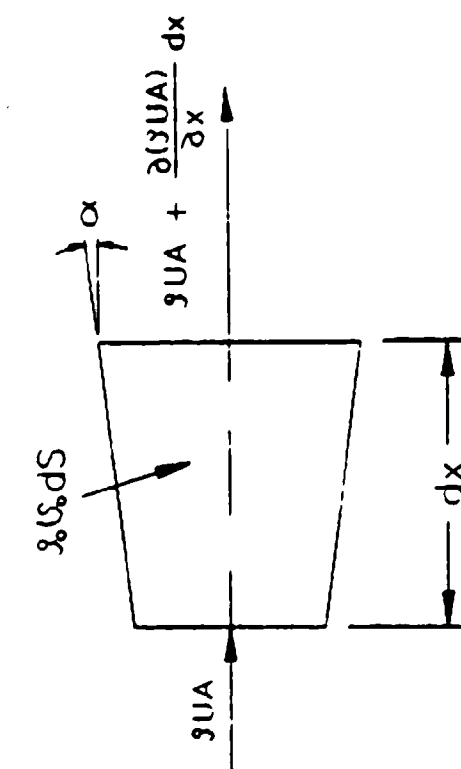
### 5.3.2 Transient Compressible Quasi - One-Dimensional Vapor Flow

A stationary vapor control volume with width  $dx$  is represented in Fig. 5.3, along with the terms which appear in the conservation equations. The control volume was drawn on the vapor side of the liquid-vapor interface. The axial velocity was taken to be the average vapor velocity. It was also assumed that the injection or suction vapor velocity at the liquid-vapor interface was perpendicular to the heat pipe wall.

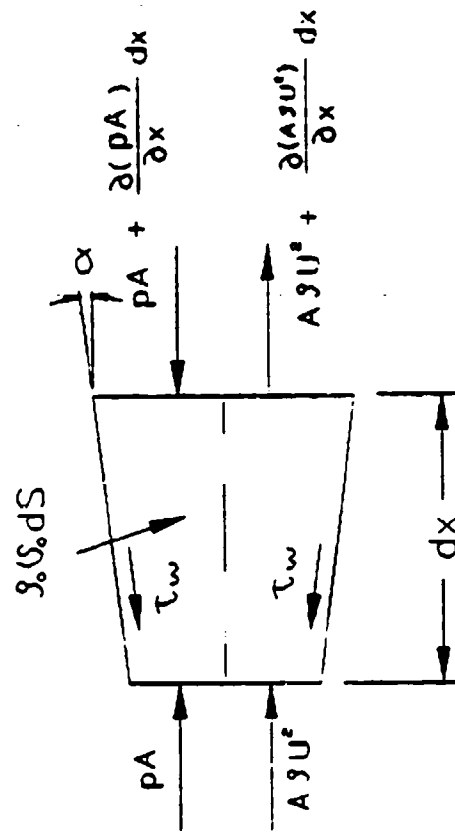
The conservation of mass is:

$$\frac{\partial(\rho \Lambda)}{\partial t} + \frac{\partial(\rho U \Lambda)}{\partial x} = v_o \rho_o \frac{dS}{dx} \quad (5.5)$$

where  $\Lambda = \Lambda(x)$  is the cross-sectional area of the vapor channel.  $S = S(x)$  is the channel wall surface area between the leading edge and position  $x$ . For a circular heat pipe  $dS/dx$  reduces to  $\pi D$ .



a) Mass



b) Momentum

Figure 5.3 Vapor Control Volume for the Conservation of Mass and Momentum

The conservation of momentum for the same control volume is:

$$\frac{\partial}{\partial t} (\Lambda \rho U) + \frac{\partial}{\partial x} (\Lambda \rho U^2) = -\Lambda \frac{\partial}{\partial x} (p - \frac{4}{3} \mu \frac{\partial U}{\partial x}) - \frac{1}{2} f \rho U^2 \frac{dS}{dx} \cos \alpha + \rho_0 v_0^2 \frac{dS}{dx} \sin \alpha \quad (5.6)$$

where  $f = 2 \tau_w / \rho U^2$  is the friction coefficient at the wall.

The perfect gas law is employed to account for the compressibility of the vapor. The equation of state is:

$$p = \rho R T_v \quad (5.7)$$

The vapor temperature and pressure are related by the Clausius-Clapeyron equation:

$$\frac{dp}{p} = \frac{h_{fg}}{R} \frac{dT_v}{T_v^2} \quad (5.8)$$

This approach corresponds to the equilibrium two-phase model (Levy, 1968) with vapor quality  $x' = 1$ . Levy shows that the equilibrium two-phase model was realistic and  $x'$  was approximately equal to unity along the heat pipe. Ivanovskii et al. (1982) also used this model with  $x' = 1$  to analyze the steady-state one-dimensional vapor flow, and found that the numerical result agreed well with the experimental data.

### 5.3.3 Boundary Conditions and Friction Coefficients

At both ends of the heat pipe, the no-slip condition for the vapor velocity was applied; i.e., at  $x = 0$  and  $L$ ,  $U = 0$ . For the wall and wick

regions, the adiabatic symmetry boundary conditions were applied except at the outer wall surface and the inner liquid-vapor interface, which will be described separately.

At the outer wall surface of the evaporator section, a distributed heat flux,  $q_{dis}$  was specified. At the outer wall surface of the condenser section, either a convective or a radiative boundary condition was specified:

$$q_c = \begin{cases} h(T_w - T_f) & \text{(convection)} \\ \sigma \epsilon T_w^4 & \text{(radiation)} \end{cases} \quad (5.9)$$

where  $h$  is the convective heat-transfer coefficient,  $T_f$  is the bulk cooling fluid temperature,  $T_w$  is the outer wall temperature of the condenser,  $\epsilon$  is the emissivity and  $\sigma$  is the Stefan-Boltzmann constant.

The boundary condition at the liquid-vapor interface is more involved because this couples the wick and the vapor flow. The interface temperature at the evaporator and adiabatic sections was assumed to be the vapor temperature obtained by the Clausius-Clapeyron equation. Since in the present study the working temperature is relatively high, the assumption is valid as shown by Dunn and Reay (1982) and by Groll et al. (1984).

The blowing or suction mass velocity  $v_o \rho_o$  in eqns. (5.5) and (5.6) was found from the interface relation:

$$\rho_o v_o = \frac{k_{eff}}{h_{fg}} \frac{\partial T_l}{\partial r} \quad \begin{cases} > 0 & \text{blowing} \\ < 0 & \text{suction} \end{cases} \quad (5.10)$$

where  $\partial T_r / \partial r$  can be calculated from the temperature distribution in the wick.

At the condenser interface, vapor condenses and releases its latent heat energy. In order to simulate this process, a heat source

$$q_s = h_{fg} \rho_0 v_0 \quad (5.11)$$

was applied at the grids next to the interface on the wick side. The suction mass flux  $v_0 \rho_0$  in eqn. (5.11) can be obtained by using the conservation of mass, eqn. (5.5), for a given vapor flow distribution along the x direction.

The friction coefficient  $f$  for the vapor flow used in this paper is described below. At the evaporator, the vapor flow is always laminar as indicated by Bowman and Hitchcock (1988). The skin-friction coefficient for a circular pipe is  $f = 16/Re$ . If the Reynolds number was greater than 2000, the flow at the condenser was considered to be turbulent, and the skin-friction coefficient was taken to be  $f = 0.079/Re^{0.25}$ . Bowman and Hitchcock (1988) studied the transient compressible flow of air in a simulated heat pipe and proposed a friction correlation which takes into account the effect of mass removal at the liquid-vapor interface on the friction coefficient. In a later paper (Bowman, 1990), he pointed out that when their proposed correlation and the skin-friction coefficients were used to model two identical heat-pipe transients, he observed very little difference. For the leading edge heat pipe shown in Fig. 5.1, the vapor channel is rectangular. The skin-friction coefficient  $f$  at the evaporator was taken to be  $f = \eta/Re_h$ , where  $Re_h$  is the Reynolds number based on the hydraulic diameter  $D_h$  of the vapor channel and  $\eta$  was taken from the chart for rectangular tubes (Chi, 1976). At the condenser,

$$f = 0.079/Re_h^{0.25}.$$

### 5.3.4 Limits to Heat Transport

Since the compressible vapor flow coupled with the wick and wall was solved, the sonic limit (Mach number approaches unity) was part of the vapor flow solution, so no special effort was needed to describe the analytical relations here. Therefore, the relations for the capillary limit and the boiling limit are emphasized.

### 5.3.5 Capillary Limit

In order for the heat pipe to operate, the maximum capillary pumping head  $(\Delta p_c)_{\max}$  must be greater than the total pressure drop in the heat pipe. Upon neglecting the gravitational head, this relation can be expressed as:

$$(\Delta p_c)_{\max} = \frac{2\sigma_\ell}{r_c} \geq \Delta p_\ell + \Delta p_v \quad (5.12)$$

where  $r_c$  is the effective capillary radius of the wick pores at the liquid-vapor interface.

The vapor pressure drop  $\Delta p_v$  was found from the vapor solution at each time step. For  $\Delta p_\ell$ , a quasi-steady state assumption and the Darcy's law were applied, with the positive x-direction opposite to the liquid flow direction:

$$\frac{dp_\ell}{dx} = \frac{\nu_\ell G}{K A_w} \quad (5.13)$$

where  $K$  is the wick permeability, which may be a function of  $x$ .  $A_w$  is the

wick cross-sectional area, and  $G$  is the local axial mass flow rate of the liquid. Equation (5.13) can be integrated to obtain the liquid pressure drop  $\Delta p_\ell$  in eqn. (5.12). Therefore,

$$\int_0^{x_{\min}} \frac{\nu_\ell G}{K\Lambda_w} dx + \Delta p_v \leq \frac{2\sigma_\ell}{r_c} \quad (5.14)$$

where  $x_{\min}$  is the location where the capillary pressure is minimum and equal to zero.

The local liquid mass flow rate  $G = G(x)$  was obtained by numerically integrating  $m_i(x) = v_o \rho_o$  along the liquid-vapor interface at time  $t$

$$G(x) = \int_0^x v_o \rho_o W d\xi \quad (5.15)$$

### 5.3.6 Boiling Limit

The boiling limit occurs at the evaporator with high radial heat fluxes. Because of the existence of the capillary wick, the boiling process is more complicated than that for smooth surfaces. Analysis of the boiling limit involves the theory of nucleate boiling, which involves two processes: the formation of bubbles (nucleation), and the subsequent growth and motion of these bubbles. A generally acceptable relation for the boiling limit is

$$\Delta T_{cr} = \frac{2T_v \sigma_\ell}{h_{fg} \rho_v} \left( \frac{1}{r_n} - \frac{1}{R_m} \right) \quad (5.16)$$

where  $r_n$  is the initial radius of the vapor bubble at its formation,  $R_m$  is the radius of the liquid-vapor interface. In the absence of sufficient data, a

conservative approach suggested by Chi (1976) would be to use the values of  $r_n$  equal to  $2.54 \times 10^{-5}$  and  $2.54 \times 10^{-7}$  m for the gas-loaded and conventional heat pipe, respectively.  $R_m$  was taken to be approximately  $r_c$  in the calculation.

#### 5.4 NUMERICAL PROCEDURE

The governing equations along with the boundary conditions were solved by employing the control-volume finite-difference approach described by Patankar (1980, 1988). For the wall and wick regions, an energy balance was directly applied to the control volume to obtain the discretization equations for temperature  $T$ . For the vapor flow, the one-dimensional SIMPLE algorithm was employed. To deal with the compressible flow, the pressure was chosen as a dependent variable and the density was obtained by directly applying the equation of state.

The discretization equations for  $U$  and  $p'$  have the general form

$$a_P \phi_P = a_E \phi_E + a_W \phi_W + B \quad (5.17)$$

which was described by Patankar (1980). For the present one-dimensional formulation, the source term  $B$  contains the blowing and suction contributions at the liquid-vapor interface which appear in eqns. (5.5) and (5.6).

At both ends of the heat pipe, the no-slip boundary condition leads to the prescribed velocity boundary conditions with  $U = 0$ . Since no boundary pressure is specified, and all the boundary coefficients in the pressure correction  $p'$  equation will be zero, the  $p'$  equation is left without any means of establishing the absolute value of  $p'$ . A direct tridiagonal matrix

algorithm would encounter a singular matrix and not be able to give a solution. In this case, the value of  $p'$  at the condenser end was assigned to zero. The absolute value of the vapor pressure at the condenser end point was calculated using the temperature of the liquid-vapor interface at the liquid side and the Clausius-Clapeyron equation. The absolute values of the vapor pressure along the heat pipe were also adjusted according to the value at the end point during the iterations. The sequence of numerical steps was as follows:

1. Initialize the temperature, velocity, and pressure fields. The density values for the vapor are obtained from the current vapor pressure and temperature fields through the equation of state.
2. Calculate the vapor-liquid interface mass velocity  $v_o \rho_o$  using eqn. (5.10).
3. Solve the vapor momentum equation to obtain  $U^*$ .
4. Solve the  $p'$  equation and update the current vapor pressure field.
5. Calculate  $U$ 's from their starred values using the velocity correction formulas.
6. Calculate the vapor temperature using the Clausius-Clapeyron equation.
7. Calculate the heat source term, eqn. (5.11), using the conservation of mass (eqn. 5.5) and the present vapor velocity solution.
8. Solve the temperature field for the wick and wall region.
9. Update the interface temperature at the evaporator and adiabatic sections with the present vapor temperature, and steps (1) - (9) are repeated until convergence is reached for each time step.

## 5.5 NUMERICAL RESULTS AND DISCUSSION

In order to validate the present model, the computer code was first written for a conventional cylindrical heat pipe, and the numerical results were compared with the experimental data by Kemme (1969). The heat pipe studied by Kemme was 1.3 m long with  $L_e = 0.143$  m,  $L_c = 1.08$  m, and inside diameter 5.7 mm with a screen wrap wick of thickness  $\delta_l = 0.15$  mm and stainless steel wall of thickness  $\delta_w = 0.9$  mm. During the experiment, the heat input was fixed to 6.4 kW. At a temperature near  $800^\circ\text{C}$ , the heat pipe was nearly isothermal so that the temperature profile was essentially flat. The operating temperature was then reduced by changing the cooling condition so that the choked condition could be reached. As the cooling rate at the condenser was increased in steps, three different sets of steady-state experimental data were obtained for subsonic (case A), sonic (case B) and supersonic (case C) vapor flow in the sodium heat pipe. In order to simulate the experimental conditions, a convective heat-transfer boundary condition was specified at the outer wall surface of the heat pipe condenser,  $q_c = h(T_w - T_f)$ . The numerical calculation was first made to reach the steady state with a vapor working temperature of  $800^\circ\text{C}$ . Then, the heat-transfer coefficient  $h$  was increased in steps, and three steady-state vapor temperature curves corresponding to the experimental data were obtained. The numerical results were compared with the experimental data in Fig. 5.4. The figure also shows the numerical outer wall temperature distributions. As can be seen, the agreement between the experimental data and the numerical results is reasonable.

The grid size used in the above numerical calculation was 8 (3 radial wick + 5 radial wall)  $\times$  48 (axial). The numerical results were essentially

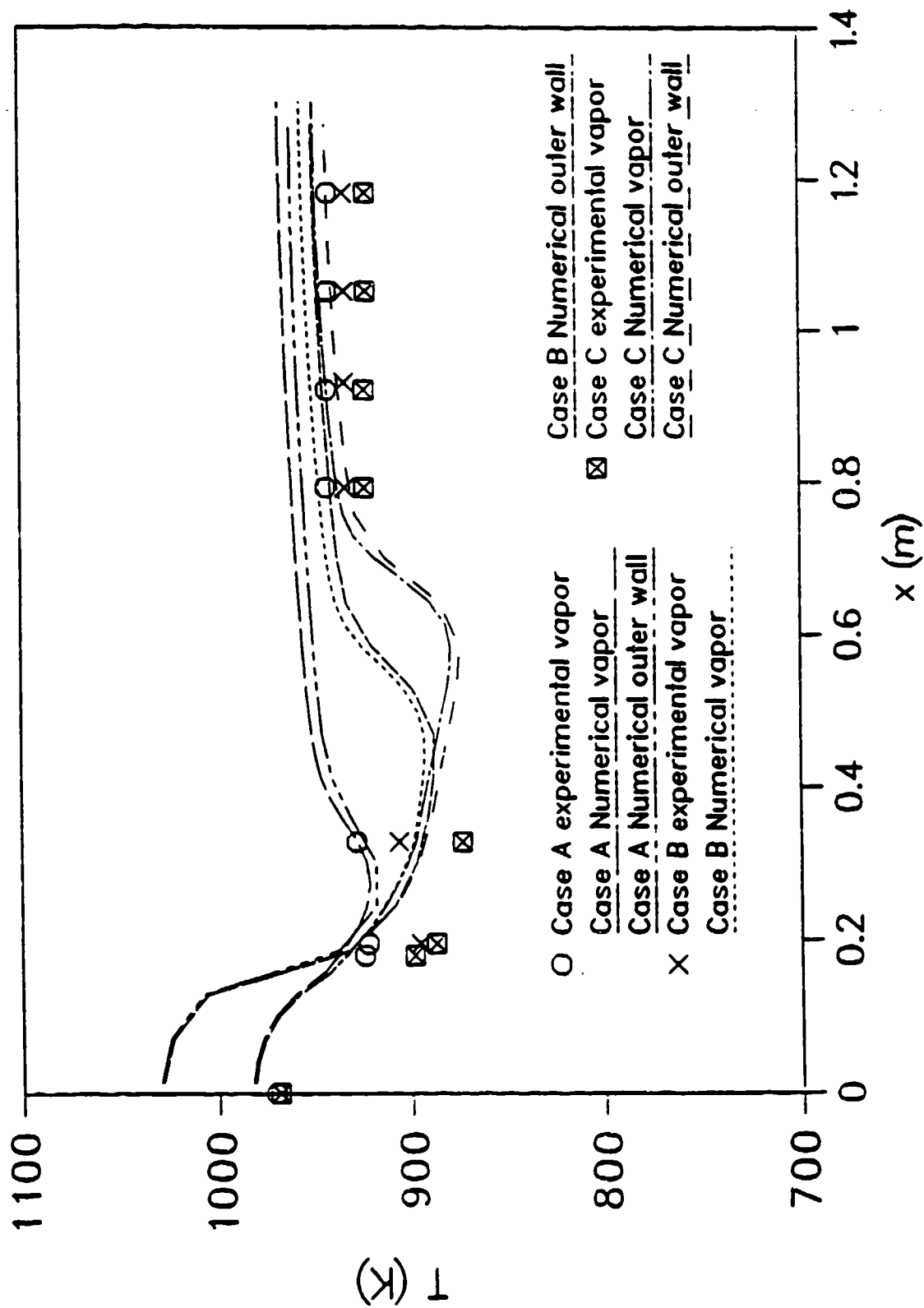


Figure 5.4 The Axial Temperature Profiles Along the Sodium Heat Pipe Compared With the Experimental data by Kemme (1969)

independent of grid size. A change of grid size from  $8 \times 40$  to  $8 \times 80$  resulted in a change in the numerical results of less than 3%. The numerical scheme used in this report has some restriction on the radial grid size for the wick and wall. The blowing or suction mass velocity  $v_o \rho_o$  was calculated using the temperature distribution in the wick (eqn. (5.10)) during the iteration. If the grid size was too small and the effective thermal conductivity was high, the temperature at a particular grid would be very close to the temperatures of the neighboring grids. As a consequence, a serious round-off errors would be produced when evaluating the temperature gradient in the wick. However, the heat pipe wick and wall are very thin (usually on the order of 1 mm), so a smaller number of grids in the wick and wall would not produce any significant discretization or truncation errors, especially when the control volume approach was used.

The numerical results were also compared with the transient experimental data by Faghri and Buchko (1990). The heat pipe was a 1-m-long multiple heat source sodium/stainless steel heat pipe with a vapor core radius  $R_v = 10.75$  mm, a wrapped screen wick of thickness  $\delta_\ell = 0.456$  mm, and stainless steel wall of thickness  $\delta_w = 2.15$  mm. The heat pipe was initially at a steady state with each of the four heaters having a power input of  $Q_1 = 90$  W. At time  $t = 0$ , the power input was increased to  $Q_2 = 115$  W for each heater. Since the sodium heat pipe assembly included additional heat capacities such as those of the coiled heaters, radiation shielding, and supports, there existed an additional thermal inertia for a power increase to the heat pipe. To account for the additional heat capacities, a transient heat input  $Q_t = Q_1 + (Q_2 - Q_1) [1 - \exp(-t/\tau_o)]$  was specified at the outer wall surface of the evaporator section. The characteristic time  $\tau_o$ , which is the time needed for the outer surface of

the heater to reach its maximum temperature after the power increase, was about 8 min from the experimental data. The boundary condition at the condenser was a radiative boundary condition,  $q_c = \epsilon \sigma T_w^4$ . The emissivity  $\epsilon$  was taken from the experiment to be  $\epsilon \approx 0.6$ . The numerical results for the vapor temperature were compared with the experimental data by Faghri and Buchko (1990) for six different times as well as two steady states in Fig. 5.5 with a good agreement.

After testing the numerical method in the above two cases, attention was turned to the leading edge heat pipe shown in Fig. 5.1. In the following numerical calculation, the emphasis was put on the leading edge heat pipe with an extremely high heat input at the evaporator to demonstrate the performance characteristics that were different from conventional heat pipes. The numerical calculation was first made for a lithium leading edge heat pipe in Fig. 5.1(a) with a uniform heat input at the evaporator,  $q_{dis} = 3 \times 10^7 \text{ W/m}^2$ . The dimensions and the properties of the heat pipe are  $L_e = 0.054 \text{ m}$ ,  $L_c = 0.051 \text{ m}$ ,  $W = 0.00630 \text{ m}$ ,  $h_o = 0.00521 \text{ m}$ ,  $R_i = 0.0015 \text{ m}$ ,  $\delta_w = \delta_l = 0.380 \text{ mm}$ ,  $(c_p \rho)_w = 4.94 \times 10^6 \text{ J/(m}^3 \cdot \text{K)}$ ,  $(c_p \rho)_{eff} = 6.8 \times 10^5 \text{ J/(m}^3 \cdot \text{K)}$ ,  $k_{eff} = 55 \text{ W/(m} \cdot \text{K)}$ ,  $k_w = 40 \text{ W/(m} \cdot \text{K)}$ . At the condenser, a convective boundary condition was specified with  $q_c = h (T_w - T_f)$ . In this case,  $T_f$  and  $h$  were taken to be 500 K and  $60000 \text{ W/(m}^2 \cdot \text{K)}$ , respectively. The initial condition for the heat pipe is  $T_v = T_w = 1200 \text{ K}$ ,  $p_i = 2050 \text{ N/m}^2$  and  $U = 0$  with a thawed working fluid. At  $t = 0$ ,  $q_{dis}$  was applied at the evaporator surface and the heat pipe startup was initiated. Figure 5.6 shows the vapor Mach number distribution along the heat pipe length during the startup process. The heat pipe reached the sonic limit in a very short time. For a conventional heat pipe, startup may be inhibited only when the heat pipe is initially in the frozen state and

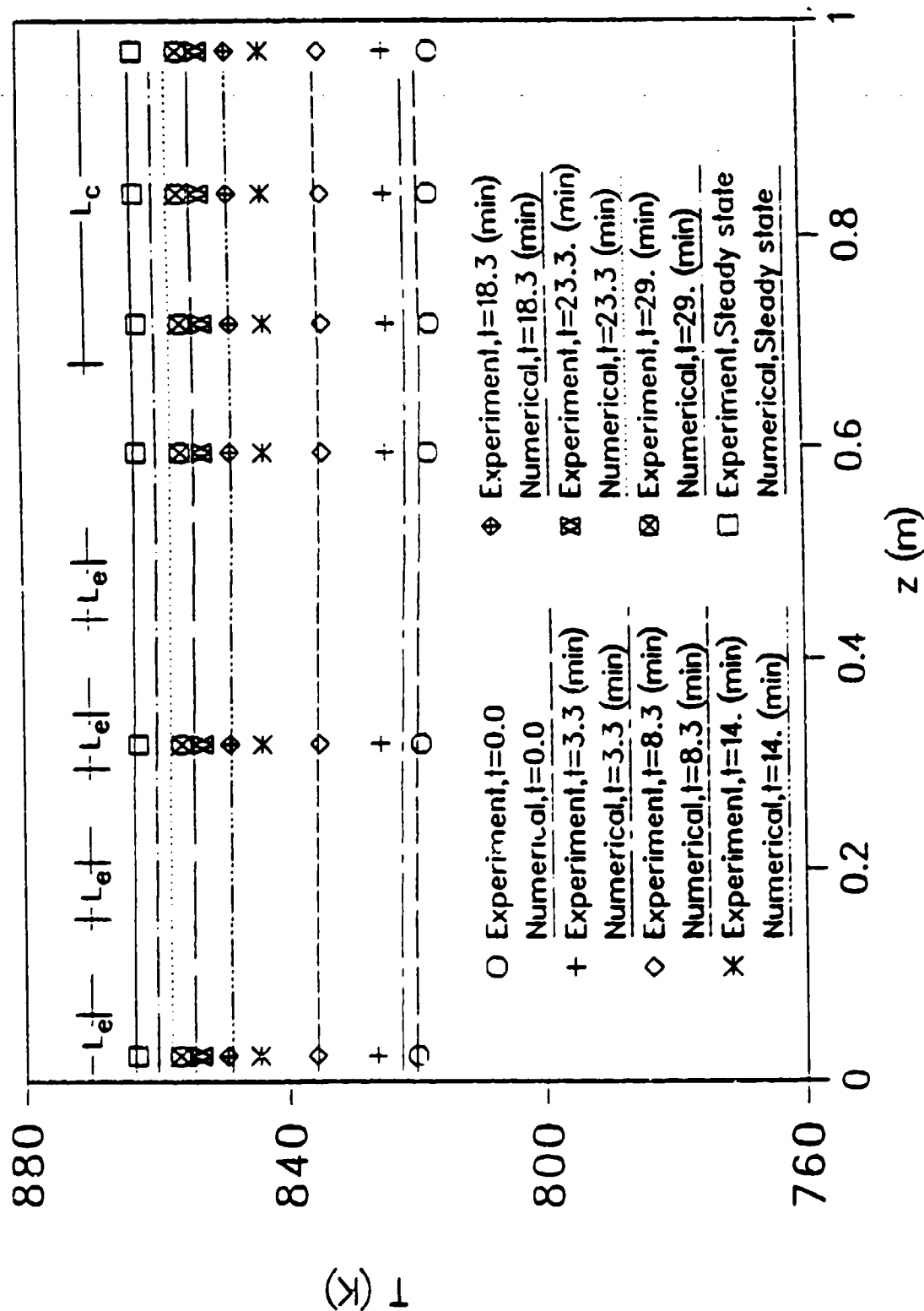


Figure 5.5 The Vapor Temperature for Different Time Periods  
Compared with the Experimental Data by  
Faghri and Buchko (1990)

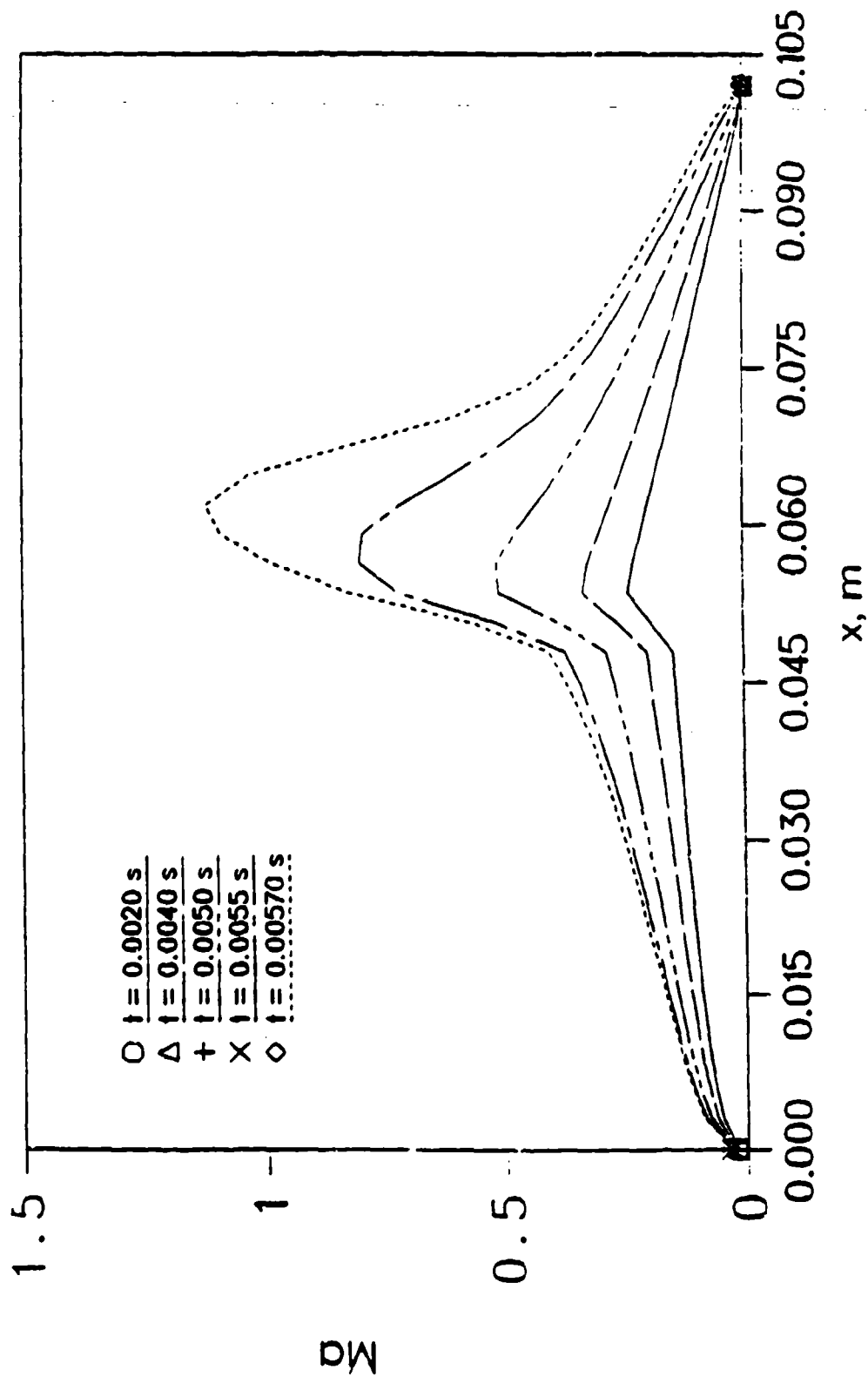


Figure 5.6 The Startup Axial Mach Number Along the Leading Edge Heat Pipe With Uniform Heating and High Heat-Transfer Coefficient

the heat-transfer coefficient at the condenser is very high. However, for the present heat pipe with an extremely high power input at the evaporator and a small geometrical dimension, startup difficulties may occur even when the heat pipe initially has a fairly high temperature. The calculation was made again with an initially lower heat transfer coefficient,  $h_i = 15000 \text{ W/(m}^2 \cdot \text{K)}$ , at the condenser, which was gradually increased to  $h = 60000 \text{ W/(m}^2 \cdot \text{K)}$  after  $t = 0.05 \text{ s}$ . The corresponding outer wall surface temperature, vapor temperature and vapor Mach number are presented in Fig. 5.7. The heat pipe started successfully without encountering the sonic limit, and reached the steady state in about 4 s. The transient periods for the present heat pipe were much shorter than those of conventional heat pipes, which have a transient period of about 10 min for a pulsed heat input as indicated by Cao and Faghri (1990). Since the present heat pipe has a much smaller geometrical dimension and therefore a smaller heat capacity, it is understandable that the heat pipe has a short transient period under a heavy heat load. Another performance characteristic is that although the vapor temperature is relatively uniform along the heat pipe length, large outer wall temperature gradients exist at the leading edge and near the evaporator-condenser junction.

A leading edge heat pipe with different heat inputs at the evaporator and a different wall and wick was then studied. The dimensions and properties of the tungsten wall and wick were  $\delta_\ell = 0.508 \text{ mm}$ ,  $\delta_w = 0.762 \text{ mm}$ ,  $(c_p \rho)_w = 2.1 \times 10^7 \text{ J/(m}^3 \cdot \text{K)}$ ,  $(c_p \rho)_{\text{eff}} = 2.60 \times 10^6 \text{ J/(m}^3 \cdot \text{K)}$ ,  $k_{\text{eff}} = 80 \text{ W/(m} \cdot \text{K)}$ ,  $k_w = 112 \text{ W/(m} \cdot \text{K)}$ , with the rest of the dimensions and working fluid of the heat pipe being the same as the previous one. The heat pipe was initially working at the steady state with a uniform power input of  $q_{\text{dis}} = 2 \times 10^6 \text{ W/m}^2$  at the

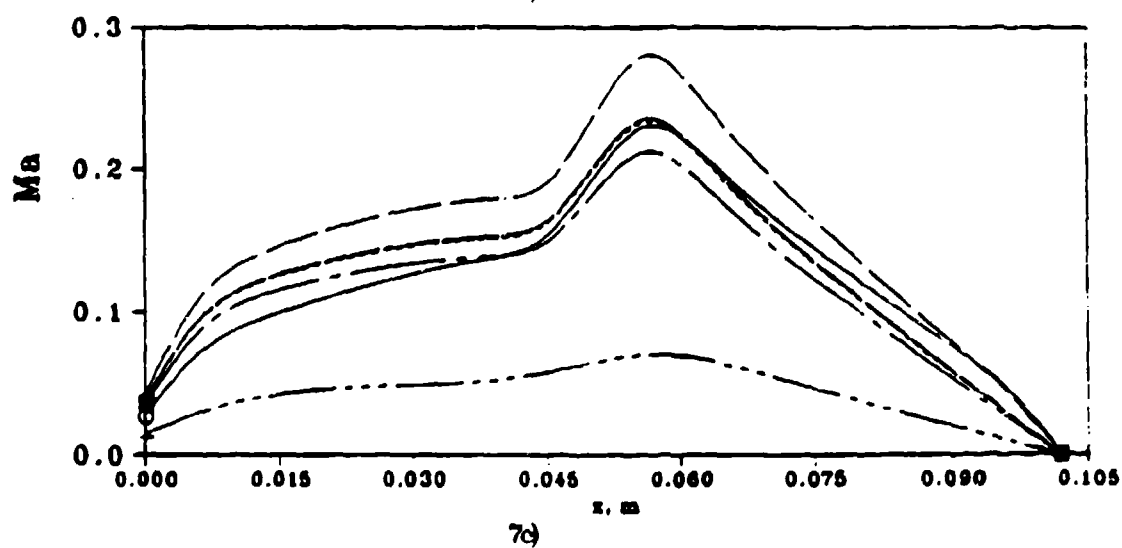
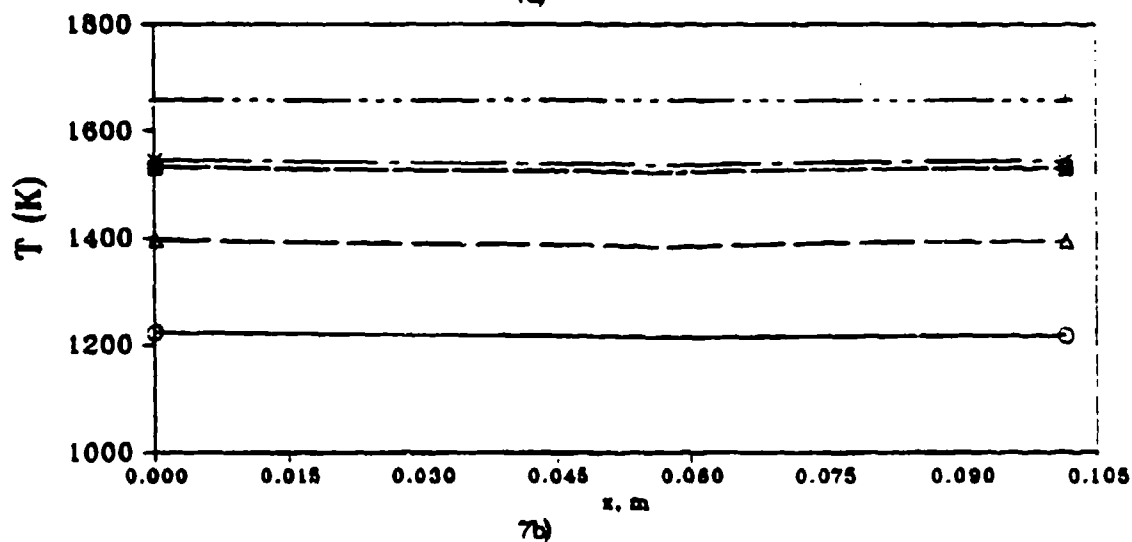
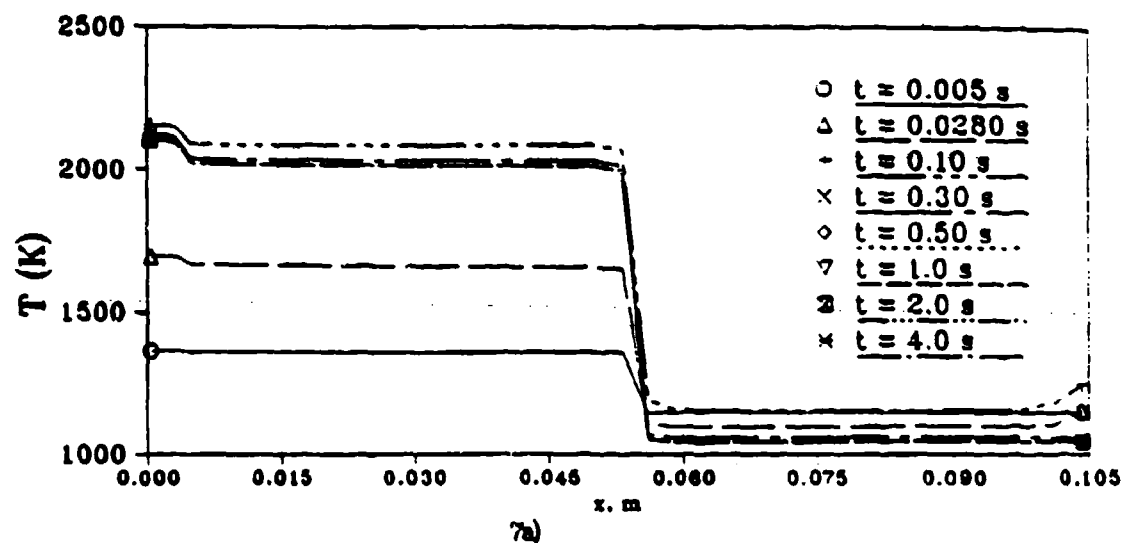
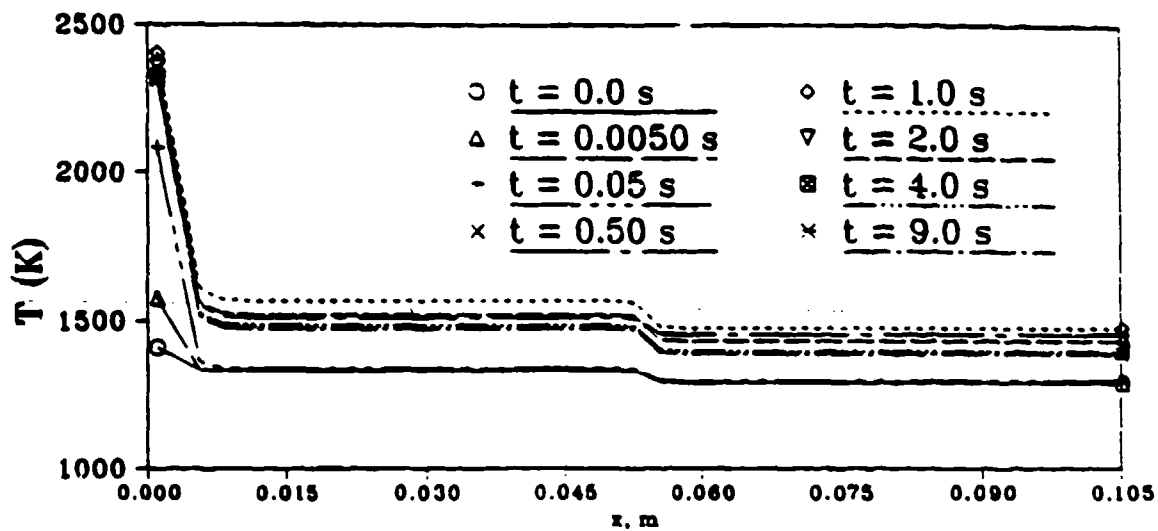


Figure 5.7 The Leading Edge Heat Pipe With Uniform Heating at Evaporator

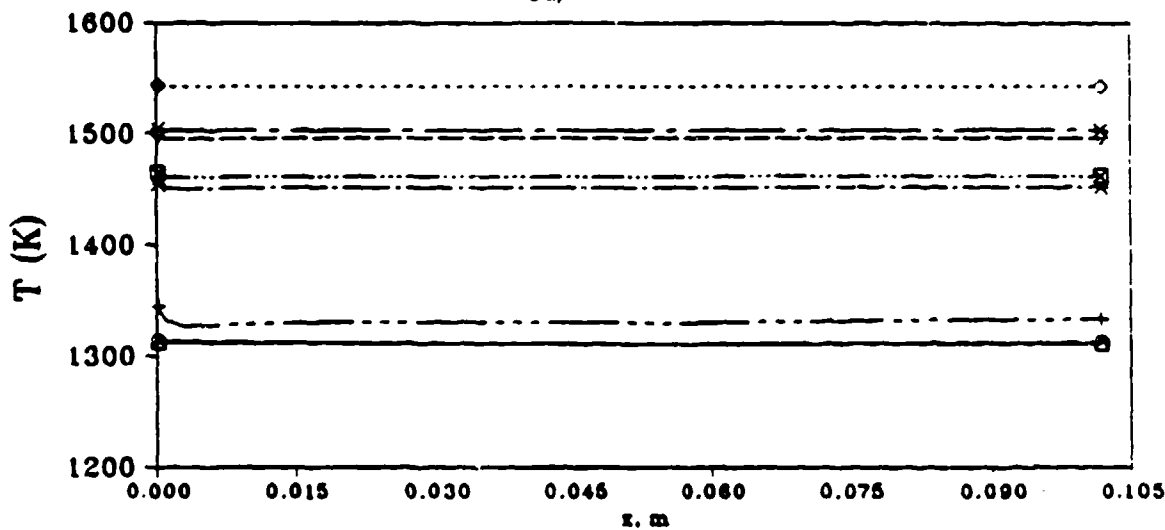
- a) Outer Wall Temperature
- b) Vapor Temperature
- c) Axial Mach Number

evaporator. At  $t = 0$ , a line heat source with a total heat input of  $Q = 2.06$  kW was added at the outer wall surface of the leading edge ( $-\frac{\pi}{2} \leq \theta \leq \frac{\pi}{2}$ ). The heat flux distribution was assumed linear at the leading edge with a maximum heat flux of  $75 \times 10^6 \text{ W/m}^2$  at  $\theta = 0$ . The initial steady-state working condition at  $t = 0$  and the subsequent transient response are illustrated in Fig 5.8. The convective heat-transfer coefficient at the condenser was initially  $h = 2000 \text{ W/(m}^2 \cdot \text{K)}$  corresponding to the initial steady state ( $t = 0$ ) and was gradually increased to  $h = 6000 \text{ W/(m}^2 \cdot \text{K)}$  after  $t = 0.2 \text{ s}$  to reduce the heat pipe working temperature. Both the vapor temperature and the wall temperature rose to a maximum as the additional heat input was applied at the leading edge, and then dropped off because of the increase of the heat-transfer coefficient at the condenser, reaching another steady state in about 9 s. The vapor velocity distribution along the heat pipe length with a uniform heat input at the evaporator was not much different from those of conventional cylindrical heat pipes as indicated by the case  $t = 0.0$  in Fig 5.8c. As the intense heat flux was applied at the leading edge ( $0 \leq x \leq R_{in} = 0.0015 \text{ m}$ ), the vapor velocity increased sharply at the leading edge region, and then began to decrease in the slope region ( $R_{in} \leq x \leq L_e$ ). In this region, the area of the vapor flow space increased significantly with much less intense evaporation at the liquid-vapor interface; therefore, the vapor velocity actually decreased. Near the evaporator-condenser junction, the vapor velocity increased to another peak value and then gradually decreased to zero along the condenser.

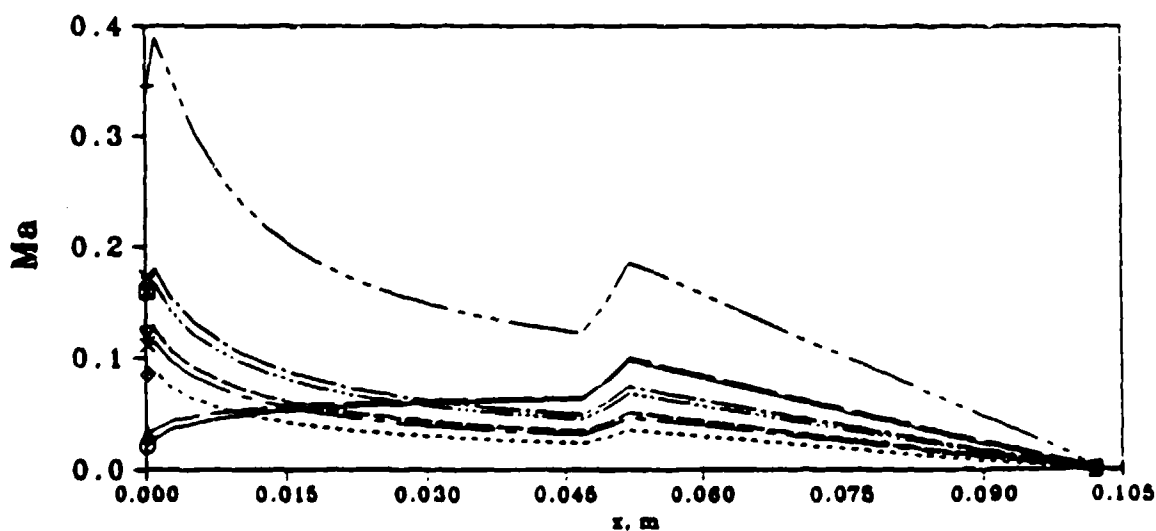
The capillary and boiling limits were also calculated for this heat pipe configuration. The heat pipe wick considered was a wrapped screen wick with a permeability  $K = 6.0 \times 10^{-9} \text{ m}^2$  and an effective capillary radius  $r_c = 3.81 \times$



8a)



8b)



8c)

Figure 5.8

The Heat Pipe With Line Source at the Leading Edge

- a) Outer Wall Temperature
- b) Vapor Temperature
- c) Axial Mach Number

$10^{-4}$  m. The  $x_{\min}$  in eqn. (14) was chosen as the location in the condenser near the evaporator-condenser junction. Figure 9 shows the liquid and vapor pressure distributions along the heat pipe at different time periods. Even for a uniform heat flux  $q_{\text{dis}} = 2 \times 10^6 \text{ W/m}^2$  (the steady state labeled with  $t = 0.0 \text{ s}$ ), the liquid pressure drop constituted only a small portion of the total capillary pressure in eqn. (5.14). As the additional power was applied at the leading edge, the vapor pressure drop increased dramatically. At  $t = 0.004 \text{ s}$ , the vapor pressure at some location near the leading edge was even lower than the liquid pressure. Shortly after this, the capillary limit was reached. This means that a special design is needed for a leading edge heat pipe with heavy heat loads to increase the total capillary pressure available, or increase the vapor flow space at the leading edge. Where the vapor and liquid pressures are equal,  $x_{\min}$  was chosen at the location near the evaporator-condenser junction because of the large vapor pressure recovery at the condenser. Ernst (1967) pointed out that if the pressure recovery in the condenser region is greater than the liquid pressure drop, then the meniscus in the wick will be convex. While this is possible in principle under normal heat pipe operation, there is excess liquid in the condenser region so that this condition cannot occur. For this reason, it is usually assumed the meniscus in the wick are flat and the liquid and vapor pressures are equal in the condenser region, as shown in Fig 5.9.

The numerical results in Fig 5.8 were obtained with the assumption that the capillary wick had been perfectly designed without encountering the capillary limits, while in reality this is not always the case. If the capillary limit was encountered, the outer wall temperature of the heat pipe would be too high and the heat pipe would be burned out.

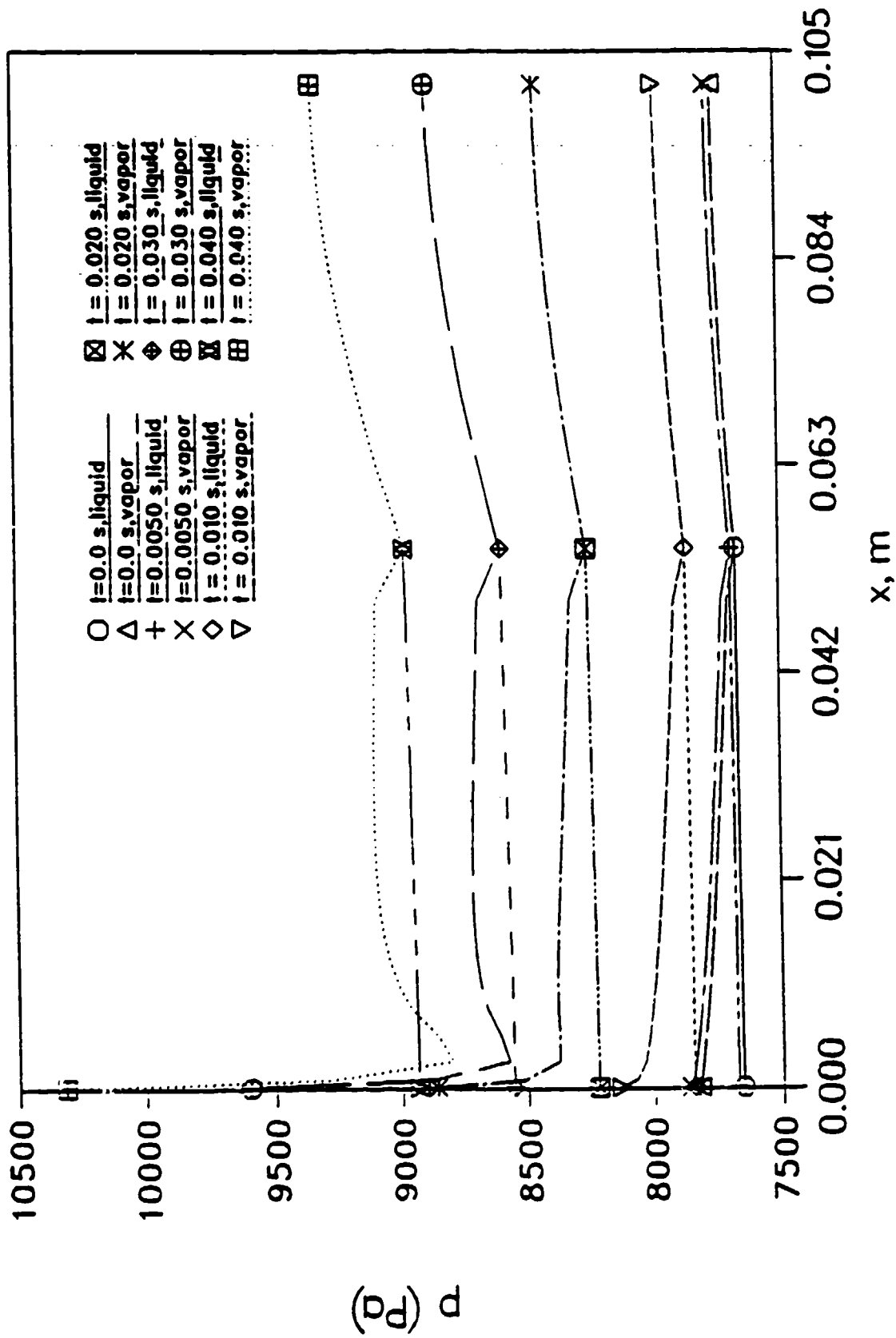


Figure 5.9 The Liquid and Vapor Pressure Distributions Along the Heat Pipe for Different Time Periods

The boiling limitation in eqn. (5.16) is heavily dependent on  $r_n$ , the initial radius of the vapor bubbles at formation. In the absence of sufficient experimental data, Chi (1976) suggested that a value of  $r_n = 2.54 \times 10^{-7}$  m be used. With this value, the boiling limitation would not be encountered in most cases except when the vapor temperature was very high and the lithium vapor pressure approached  $10^5$  Pa. However, the value of  $r_n = 2.54 \times 10^{-7}$  m can only be used when the heat pipe has been carefully processed to eliminate all noncondensable gases. In the presence of noncondensable gases, a much larger value ranging from  $2.54 \times 10^{-6}$  m to  $2.54 \times 10^{-5}$  m should be used. In this case, the boiling limitation might be encountered with heavy heat loads.

Calculations were also made with a nonuniform heating condition along the width of the leading edge heat pipe shown in Fig. 5.1(b). The distributed heat flux was  $q_{dis} = 3 \times 10^7$  W/m<sup>2</sup> with  $W_e = 1.90$  mm. The heat pipe configuration and the initial condition were the same as those of the first leading edge heat pipe examined. In this case, the heat transfer in the wall and wick was three-dimensional. Figure 5.10 shows the outer wall temperature along the stagnation line in the width direction. As shown, heat conduction in the width direction is evident because of the nonuniform heating. However, the heat conduction effects are limited to a region about  $2(\delta_l + \delta_w)$  wide.

## 5.6 CONCLUSIONS

The numerical method presented in this paper proves to be flexible and capable of dealing with conventional and nonconventional heat pipes. The numerical results have been compared with two sets of experimental data with good agreement. The numerical results for the leading edge heat pipe

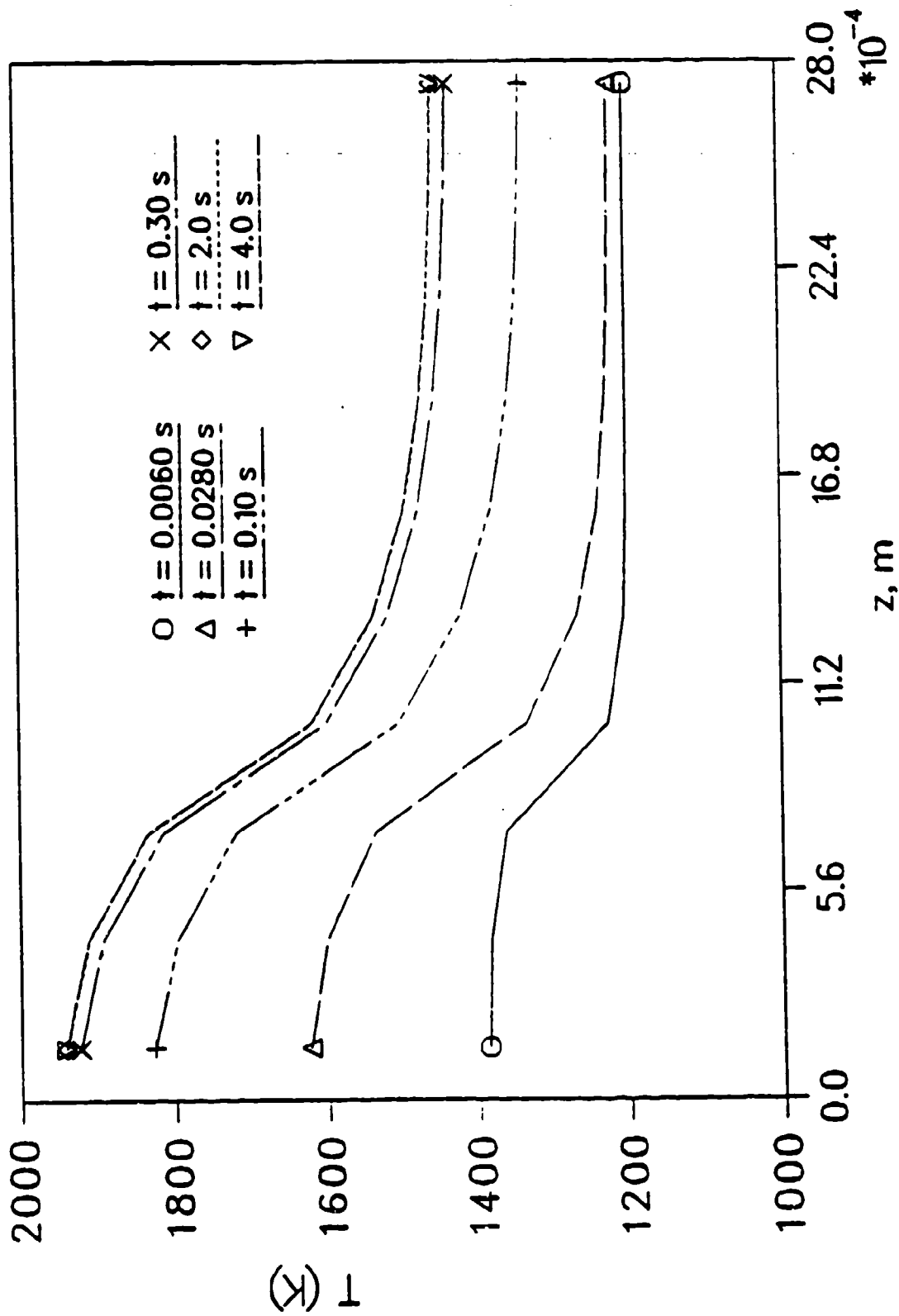


Figure 5.10 The Outer Wall Temperature Along the Stagnation Line for the Case of Nonuniform Heating

demonstrated the following different performance characteristics:

- (1) For a leading edge heat pipe with an extremely high heat load at the evaporator and a small geometrical dimension, difficulties with startup at a relatively high temperature may be encountered when the cooling rate at the condenser is not low enough.
- (2) The leading edge heat pipe reached the steady state very quickly because of the high heat load and small heat capacity of the heat pipe.
- (3) When the heat load was very high at the leading edge, the vapor pressure drop was a dominant factor for the capillary limit consideration. An increase in the vapor space at the leading edge is recommended.
- (4) Even though the vapor temperature was relatively uniform along the heat pipe length, large temperature gradients existed at the outer wall surface of the heat pipe. These temperature gradients may result in large thermal stresses which may limit the life of the heat pipe.
- (5) Since temperature drops across the wick at the leading edge were as high as several hundreds of degrees, the boiling limit may be encountered in spite of the liquid-metal working fluid. More effort is needed to predict the boiling limit more accurately.

All these performance characteristics mentioned above add additional challenges to heat pipe applications, and further study is definitely needed.

## REFERENCES

Bowman, W.J., 1987, "Simulated Heat Pipe Vapor Dynamics," Ph.D. Dissertation, Air Force Institute of Technology.

Bowman, W.J., and Hitchcock, J., 1988, "Transient, Compressible Heat Pipe Vapor Dynamics," Proc. 25th ASME National Heat Transfer Conf., Houston, Texas, pp. 329-337.

Bowman, W.J., 1990, "Transient Heat-Pipe Modeling, the Frozen Start-Up Problem," Proc. AIAA/ASME 5th Joint Thermophysics and Heat Transfer Conference, AIAA 90-1773, Seattle, WA.

Cao, Y., and Faghri, A., 1990, "A Transient Two-Dimensional Compressible Analysis for High-Temperature Heat Pipes with a Pulsed Heat Input," Numerical Heat Transfer, Part A, Vol. 18, pp. 483-502.

Cao, Y., Faghri, A., and Mahefkey, E.T., 1989, "The Thermal Performance of Heat Pipes With Localized Heat Input," Int. J. Heat Mass Transfer, Vol. 32, No. 7, pp. 1279-1287.

Chang, W.S., 1987, "Effective Thermal Conductivity of Wire Screens," Fundamentals of Conduction and Recent Developments in Contact Resistance, HTD-Vol. 69, pp. 64-75.

Chang, W.S., and Colwell, G.T., 1985, "Mathematical Modeling of the Transient Operating Characteristics of a Low-Temperature Heat Pipe," Numerical Heat Transfer, Vol. 8, pp. 169-186.

Chen, M.M., and Faghri, A., 1990, "An Analysis of the Vapor Flow and the Heat Conduction Through the Liquid-Wick and Pipe Wall in a Heat Pipe With Single and Multiple Heat Sources," Int. J. Heat Mass Transfer, Vol. 33, No. 9, pp. 1945-1955.

Chen, M.M., and Faghri, A., 1990, "An Analysis of the Vapor Flow and the Heat Conduction Through the Liquid-Wick and Pipe Wall in a Heat Pipe with Single or Multiple Heat Sources," International Journal of Heat and Mass Transfer, Vol. 33, No. 9, pp. 1945-1955.

Chi, S.W., 1976, Heat Pipe Theory and Practice: A Sourcebook, McGraw-Hill Book Company, New York.

Deverall, J.E., Kemme, J.E., Florschuetz, L.W., 1970, "Sonic Limitations and Startup Problems of Heat Pipes," Los Alamos Scientific Laboratory Report LA-4518, Los Alamos, NM.

Dunn, P.D., and Reay, D.A., 1982, Heat Pipes, Third Edition, Pergamon Press.

Ernst, D.M., 1967, "Evaluation of Theoretical Heat Pipe Performance," Thermionic Conversion Specialist Conf., Palo Alto, California.

Faghri, A., and Buchko, M., 1991, "Experimental and Numerical Analysis of Low Temperature Heat Pipes With Multiple Heat Sources," ASME J. Heat Transfer, Vol. 113, No. 3, pp. 728-734.

Faghri, A., and Chen, M.M., 1989, "Numerical Analysis of the Effects of Conjugate Heat Transfer, Vapor Compressibility and Viscous Dissipation in Heat Pipes," Numerical Heat Transfer Journal, Part A, Vol. 16, pp. 389-405.

Faghri, A., and Thomas, S., 1989, "Performance Characteristics of a Concentric Annular Heat Pipe, Part II, Vapor Flow Analysis", ASME J. Heat Transfer, Vol. 111, No. 4, pp. 851-857.

Faghri, A., Buchko, M., and Cao, Y., 1991, "A Study of High Temperature Heat Pipes with Multiple Heat Sources and Sinks, Part I: Experimental Methodology and Frozen Startup Profiles," ASME Journal of Heat Transfer, Vol. 113, No. 4.

Faghri, A., Buchko, M., and Cao, Y., 1991, "A Study of High Temperature Heat Pipes with Multiple Heat Sources and Sinks, Part II: Analysis of Continuum Transient and Steady State Experimental Data with Numerical Prediction," ASME Journal of Heat Transfer, Vol. 113, No. 4.

Ganic, E.N., Hartnett, J.P., and Rohsenow, W.M., 1985, "Basic Concepts of Heat Transfer," in Handbook of Heat Transfer Fundamentals, Edited by W.M. Rohsenow et al., McGraw-Hill Book Company.

Groll, M., Brost, O., Mack, H., and Shevchuk, E.N., 1984, "Evaporation Heat Transfer of Sodium From Capillary Structures," Research and Development of Heat Pipe Technology, Supplement, pp. 21-27.

Hall, M.L., and Doster, J.M., 1990, "A Sensitivity Study of the Effects of Evaporation/Condensation Accommodation Coefficients on Transient Heat Pipe Modeling," Int. J. Heat Mass Transfer, Vol. 33, pp. 465-481.

Ivanovskii, M.N., Sorokin, V.P., and Yagodkin, I.V., 1982, The Physical Principles of Heat Pipes, Clarendon Press, Oxford.

Jang, J.H., 1988, "An Analysis of Start-Up From the Frozen State and Transient Performance of Heat Pipes," Ph.D. Dissertation, Georgia Institute of Technology, Atlanta, GA.

Jang, J.H., Faghri, A., Chang, W.S., and Mahefkey, E.T., 1990, "Mathematical Modeling and Analysis of Heat Pipe Start-Up From the Frozen State," ASME J. Heat Transfer, Vol. 112, No. 3, pp. 586-594.

Karki, K.C., 1986, "A Calculation Procedure for Viscous Flows at All Speeds in Complex Geometries," Ph.D. Dissertation, University of Minnesota.

Keddy, E.S., and Martinez, H.E., 1982, "Development of High Temperature Liquid Metal Heat Pipes for Isothermal Irradiation Assemblies," Proc. 17th Intersociety Energy Conversion Engineering Conference, pp. 58-62.

Kemme, J.E., 1969, "Ultimate Heat-Pipe Performance," IEEE Transactions on Electronic Devices, Vol. ED16, No. 8, pp. 717-723.

Levy, E.K., 1968, "Theoretical Investigation of Heat Pipes Operating at Low Vapor Pressure," J. Engineering for Industry, Vol. 90, Series B, No. 4, pp. 547-552.

Merrigan, M.A., Keddy, E.S., Runyan, J.R., Martinez, H.E., 1984, "Development and Extended Operation of a High Power Radiation Loaded Heat Pipe," Los Alamos Scientific Laboratory Report LA-UR-84-1950, Los Alamos, NM.

Merrigan, M.A., Keddy, E.S., Sena, J.T., 1986, "Transient Performance Investigation of a Space Power System Heat Pipe," AIAA/ASME 4th Joint Thermophysics and Heat-Transfer Conference, AIAA Paper 86-1273.

Patankar, S.V., 1980, Numerical Heat Transfer and Fluid Flow, McGraw-Hill Book Company, New York.

Patankar, S.V., 1988, "Elliptic Systems: Finite-Difference Method I," in Handbook of Numerical Heat Transfer, Edited by W.J. Minkowycz, et al., John Wiley and Sons, Inc.

Ponnappan, R., 1990, "Comparison of Vacuum and Gas Loaded Mode Performances of a LMHP," AIAA/ASME 5th Joint Thermophysics and Heat-Transfer Conference, AIAA Paper 90-1755.

Rosenfeld, J.H., 1987, "Modeling of Heat Transfer Into a Heat Pipe for a Localized Heat Input Zone," Proc. AIChE Symposium Series, Heat Transfer, Vol. 83, pp. 71-76.

Shaubach, R.M., Dussinger, P.M., and Bogart, J.E., 1990, "Boiling in Heat Pipe Evaporator Wick Structures," Proceedings of 7th International Heat Pipe Conference, Minsk, USSR.

Sockol, P.M. and Forman, R., 1970, "Re-examination of Heat Pipe Startup," Proc. 9th IEEE Thermionic Conversion Specialist Conference, pp. 571-573.

Spalding, D.B., 1980, "Mathematical Modeling of Fluid-Mechanics, Heat Transfer, and Chemical Reaction Processes, a lecture course," CFDU Report, HTD/80/1, Imperial College, London, U.K.

Tanaka, Y., Yamamoto, T., Matsumoto, S., Hirano, S., Ikeda, Y., Mochizuki, M., Sugihara, S., 1990, "Container Failure of Sodium Heat Pipe Due to Local Dry-out," Proceedings of 7th International Heat Pipe Conference, Minsk, USSR.